

POLITECNICO DI TORINO

Corso di Laurea Magistrale in Petroleum and Mining Engineering

Tesi di Laurea Magistrale

Measurement of the Shock Wave Pressure Using Low Cost Sensors



Relatore

Prof. Marilena Cardu

Correlatore

Prof. Takis Katsabanis

Candidato

Giovanni Pais

Anno Accademico 2019/2020

Alla mia famiglia...

ABSTRACT

This work was carried out through a collaboration between Politecnico di Torino and Queen's University (Kingston, Ontario, Canada) under the supervision of Prof. M. Cardu and Prof P. D. Katsabanis.

A laboratory environment was utilized to test the performance of the different gauges employed to collect pressure pulse data, which can allow to understand the malfunction and the sympathetic detonation of explosives due to shock waves in different media. The experiments were carried out both in boreholes (10 cm of diameter) and buckets (with diameter of 30 cm) by using respectively sensitized Emulsion and Pentolite 50/50.

Relationships were sought in order to understand the attenuation of the shock wave pressure in boreholes, which were stemmed and unstemmed, and in the surrounding rock. The shock wave pressure was measured throughout two different gauges, built by the candidate, that take advantage of two different effects, namely, Piezoresistive and Piezoelectric effect.

Thereby, afterwards, an improved design sensor was developed for the Piezoresistive gauges, which showed smoother trend and better respond compared to the other past attempts. Furthermore, it was found that some theories cannot be applied in a confined environment and that, at certain separation distances, the shock wave pressure detected is relevant, thus, it could influence nearby charges, as well as detonators.

Instead, from the Piezoelectric gauges, new information came up; this aroused interest, as well as doubts in this piece of technology. This technology nowadays has opened the door to new researchers and further investigation has to be done.

ACKNOWLEDGEMENTS

Long and struggled journey this thesis; anyways, I'd like to thank so many people who helped me in different ways.

First of all, I'd like to thank my advisors, Prof. Katsabanis and Prof. Cardu, for their guidance and most important, for their patience during these long six months.

I'm grateful for all the time spent at Queen's, in the laboratories and at the test site. I'd like to thank Oscar Rielo for his help for instrumentation and especially for his friendship, because he didn't leave me alone during these months, and he made me smile every day. Finally, I'd like to thank Perry Ross and Larry Steele, for their constant support and time spent in the lab, for their knowledge and for their patient for answering me to each question and curiosity. I'd like to extend my thanks and appreciation to the whole staff of the Robert Buchmann department of mining, to all my colleagues, especially to the first person I met there, Noufou Traore, the most positive person in this world; I wish him all the best.

All my permanence in Canada was made amazing by the best people who somebody can meet; in fact I'd like to thank all the people I met at QUIC, in particular my second family: Stacy Pinto, Myron Menezes, Aimée Carter, Taylor de Souza, Harshvir Singh, Emma Bouillard, Flavio Martins, Andres Ramos and Ana Patricia and so on; they never left me alone, bad or good moments, it didn't matter, they were always there as a second family.

Me gustaría dar la gracia a todas las personas que he encontrado en España, antes de todos quería nombrar mis grupo de amigos, los que hicieron esto viaje uno de los mas divertido y maravilloso de mi carrera. Entonces, quería dar la gracias a toda "La Crew" que nunca me dejaron solo y cada dia me han hecho sonreir, gracias. Ademas queria dar la gracia a toda la ESN Huelva, por su amistad y la costante presencia durante esta esperiència. De verdad, me gustaría nombrarle todas pero es imposible! Y por fin quiero dar la gracia a mi colega y amiga Alba, porque sin ella habia sido perdido en la uni y en una ciudad como Huelva. Gracias a todo chicos. (lo siento mucho por las tildes)

Ora ci terrei a ringraziare le persone che mi hanno accompagnato durante questi sei lunghissimi anni di carriera universitaria e molto più. Sicuramente, senza mia sorella Sara sarei ancora alle scuole superiori (o prima?), la ringrazio per tutta la sua fiducia, per tutto il tempo speso con me, e, soprattutto, per la sua infinita pazienza. Ringrazio mio padre Gavino e mia madre Fiamma, per avermi supportato, ma più importante, supportato durante tutti questi anni. Li ringrazio infinitamente per avermi insegnato tutto, per avermi insegnato a guardare qualsiasi cosa con curiosità e infine, a chiedermi “il perché” di qualsiasi cosa.

Vorrei ringraziare i miei Nonni, avrei voluto che fossero tutti qua ad ascoltarmi per renderli orgogliosi di quello che son diventato dopo tutte queste esperienze e questo tempo; se sono qui oggi è decisamente anche grazie a loro. Ringrazio i miei zii, Fabrizio, Maria Giovanna e Pina, per la loro costante presenza durante tutti questi anni; i miei cugini: Martina, Walter, Floriana e Adele che non mi hanno mai lasciato solo e mi hanno sempre fatto sentire a casa nonostante la mia poca presenza in Sardegna.

Un grazie va a tutti i miei colleghi e amici del Politecnico di Torino e dell’Università di Cagliari, gli devo davvero tanto. Un grazie speciale va a tutti i miei amici, in particolare ci terrei a ringraziare: “I soliti Babaunzi” e gli amici di una vita “I soliti noti”, i miei coinquilini Enrico e Pierluigi, “Gli amici del sig. Vloris”, Valeria, Mara, Gianfranco e Paola; vorrei nominarvi uno ad uno ma non basterebbe la pagina. Vi ringrazio di cuore per essermi stati vicino, per i bellissimi momenti passati insieme e per continuare a “ridimensionarmi” ogni volta che esagero!

Infine, ci terrei a ringraziare Francesca, che, nonostante tutto, mi supportato durante tutti i miei studi e tutto questo tempo. Senza di lei, probabilmente, non avrei mai intrapreso in primo luogo la mia carriera universitaria in ingegneria.

INDEX

	ABSTRACT	1
	ACKNOWLEDGEMENTS	2
	Figure List	7
	Introduction	11
1	Pressure Concepts Review	14
	1.1 Introduction	14
	1.2 Explosion pressures	15
	1.2.1 Detonation Pressure	16
	1.2.2 Explosion Pressure	17
	1.2.3 Borehole Pressure	17
2	Shock waves	19
	2.1 Introduction	19
	2.2 Qualitative description of a shock wave	19
	2.3 Attenuation behind shock waves	21
	2.4 Rankine-Hugoniot Jump Equations.	23
	2.4.1 Mass balance	23
	2.4.2 Momentum Balance	24
	2.4.3 Energy Balance	25
	2.5 The Hugoniot Planes	26
	2.5.1 The Hugoniot equation	26
	2.5.2 The $U-u$ plane	26
	2.5.3 The $P-v$ Plane	27
	2.5.4 The $P-u$ Plane	29
	2.6 Shock Wave Attenuation, Rarefaction Waves	31
	2.6.1 Results of Shock Wave Attenuation in Different Materials	32

2.7	Shock propagation	33
2.8	Collision of Two Shock Waves	36
2.9	Underwater Explosions	38
3	Malfunction and Sympathetic Detonation	40
3.1	Introduction	40
3.2	Explosive Classification	41
3.2.1	Primary explosives	41
3.2.2	Secondary explosives	41
3.3	Shock Sensitivity	42
3.4	Changes in the Density	45
3.5	Desensitization of Explosives	45
3.6	Alteration of The Produced Fumes	48
3.7	Sympathetic Detonation	49
3.8	Detonator Malfunction	51
3.9	Effect of Pressure on Desensitization	54
3.10	Pressure Effects in Deck Blast	56
4	Pressure Sensor's Literature Review	59
4.1	CCR Review	59
4.2	PVDF Review	60
5	Pressure Sensors	61
5.1	Introduction	61
5.2	Carbon Composition Resistors	61
5.2.1	Working principle	63
5.2.2	Calibration Equation Selection	64
5.3	Piezo polymeric film gauges	67
5.3.1	Working principle	69
5.3.2	Calibration Equation	69

6	Field Experiments	72
6.1	Introduction	72
6.2	CCR Gauges	72
6.2.1	CCR, first typology	73
6.2.2	CCR, second typology	75
6.2.3	CCR, third type	76
6.3	CCR Experimental Setup and Procedures	77
6.3.1	First tests, setup 13/09/2019	77
6.3.2	Second tests, setup 27/10/2019	82
6.3.3	Pipe experiments, setup	85
6.3.4	First Borehole tests, setup	87
6.3.5	Second Borehole tests, setup	90
7	Results	92
7.1	Verification of the Pressure Sensor Functionality	92
7.2	Comparison Between Emulsion Charge and Pentolite Charge	97
7.2.1	Holmberg-Persson adapted integration	100
7.3	Stemming Attenuations	101
7.4	Attenuation in Parallel Holes	103
8	Conclusions	105
	REFERENCES	106
	APPENDIX I	109

FIGURE LIST

Figure 1-Decking technique, different typologies	12
Figure 2- Parallel holes pattern.....	13
Figure 3- Bragg's Scheme.....	14
Figure 4- Sketch of the initiation, Source: Mancini & Cardu (2001).....	15
Figure 5- Definitions of some specific pressures on the pressure history in a blasting hole, Source: Shulin Nie (1999)	15
Figure 6- Differences among the pulsed load and quasi-static load. Source: Mancini & Cardu (2001).....	16
Figure 7- Linear Stress and Strain behaviour. Source: H.F. Abdalla et al. (2006)....	19
Figure 8- Pressure wave at high pressure. Source: https://en.wikibooks.org/wiki/Engineering_Acoustics/Qualitative_Description_of_Shocks	20
Figure 9- Shocking-up of a pressure wave. . Source: https://en.wikibooks.org/wiki/Engineering_Acoustics/Qualitative_Description_of_Shocks	21
Figure 10- Square-wave shock. . Source: https://en.wikibooks.org/wiki/Engineering_Acoustics/Qualitative_Description_of_Shocks	21
Figure 11- Attenuation of a shock-wave shock. . Source: https://en.wikibooks.org/wiki/Engineering_Acoustics/Qualitative_Description_of_Shocks	22
Figure 12- Pressure-Time.	23
Figure 13- Control Volume or Mass Passing Through a Shock Front. Source: P.W. Cooper (1997).....	24
Figure 14- U-u Hugoniot. Source: Z.X. Zhang (2016).....	27
Figure 15- A P-v Hugoniot for TNT (cast). Source: Z.X. Zhang (2016)	29
Figure 16-P-u Hugoniots, Lagrangian, Eulerian. Source: D. Grady (2017).....	30
Figure 17-Test set up (left), Attenuation of peak pressure P with the distance travelled in solid specimen (right). Source: Khurana et al. (2012).....	32
Figure 18- Example of shock wave travelling in two material; $Z_A > Z_B$. Source: Z.X. Zhang (2016)	35

Figure 19- Up, Coordinates to shock collision; Down, Solution for P_3 due to their collision. Source: Z.X. Zhang (2016)	37
Figure 20-HEs and BAs subcategories.	42
Figure 21- Explosive Train, Initiation Sequence. Source: USA Department of Homeland Security.	42
Figure 22- VOD vs Density. Source: www.iring.ca.....	47
Figure 23- Left, typical configuration, Right, different kind of configuration, less adopted.....	47
Figure 24- The concept of hot spot, shock wave and air bubble/micro-balloon interaction. Source: Ghorbani (1997)	48
Figure 25- Test of Sympathetic Detonation. Source: Zou (2017)	49
Figure 26- Up: Parallel Pattern Configuration. Down: Decked Charges. Both Contain Sensitized Emulsion Cartridges.	50
Figure 27- Detonators, Left-NONEL det., Right-Electric det. Source:.....	52
Figure 28- Experiment Donor-Receptors Configuration. Source: www.iring.ca.....	53
Figure 29- Damage due to a shock wave from an adjacent charge placed in a side borehole. Source: www.iring.ca	53
Figure 30- Comparison between measured and calculated pressures away from a charge in a water filled borehole. Source: Katsabanis (2013).....	57
Figure 31- Energy fluence vs. Pressure at Different Durations. Source: Katsabanis (2013).....	58
Figure 32-Effect of Shock Pulse Duration vs Peak Pressure. Source: www.iring.ca	58
Figure 33- Pressure measurement circuit by means of a signal conditioner (current generator).....	62
Figure 34- Carbon Resistor by Allen Bradley. Source: A&B Data-Sheet	62
Figure 35- Carbon Resistor by Allen Bradley.	63
Figure 36- (a) Light microscope image of a cross section through a carbon composition resistor. (b) The conductive core comprises phenolic resin which is enriched with carbon particles to serve as conductive material. Source: Hoerth et al. (2014).....	63
Figure 37- Aquarium Experiments performed by Katsabanis (1997). Source: Gullermo C.O, Silva (2007).....	65
Figure 38- Pressure vs R/R_0	66

Figure 39- Voltage Drop Due To Shock Wave, Bucket Experiments.....	66
Figure 40-Pressure Curve Obtained From Figure 38	67
Figure 41-FDT series	68
Figure 42- Piezoelectric effect sketch considering PZT as piezoelectric material. Source: https://www.liberaldictionary.com/piezoelectric/	69
Figure 43- Hopkinson Split Bar in Little Scale	70
Figure 44- Hopkinson Split Bar.....	71
Figure 45- Hopkinson Split Bar.....	71
Figure 46- Generic coaxial cable cutaway view	73
Figure 47- Twisted cables.....	73
Figure 48- First step, CCR, first typology	73
Figure 49- Second step, CCR, first typology.....	74
Figure 50- Finished sensors, first typology	75
Figure 51- Finished sensors, second typology, not sealed yet (always through using plastic ties).....	76
Figure 52- CCR, third typology, before being insulated	76
Figure 53- Finished sensor, third typology, insulated with a special coating.....	77
Figure 54- First test's setup, starting from the left side, rightwards: Signal conditioner, Microtrap, Multimeter, Chargers.....	78
Figure 55- Pressure curve. TEST 1, 30mm faraway from the booster	79
Figure 56- Voltage drop, TEST 1, 30mm faraway from the booster, Volts-micro seconds.....	79
Figure 57- Ignition System, Blasting Machine plus Electric and NONEL detonator.	80
Figure 58- Experiment 1, Primer on the bottom of the bucket, sensors hanged at difference heights.....	81
Figure 59- Lateral view, Orthogonal Projection, First set up	81
Figure 60- Tektronix TDS10001B (left), Yokogawa DL750 (right).....	82
Figure 61- CCR third type during field experiments.....	83
Figure 62- Lateral view, Orthogonal Projection, Third type of CCR, first try.....	84
Figure 63- Picture taken on field, putting in place the sensors.....	84
Figure 64- Lateral view, Orthogonal Projection, Big Bin, [cm].....	85
Figure 65- Pipe experiments, setup	86

Figure 66- Inside view's Pipe.....	87
Figure 67- NONEL Detonator Glued at the Bottom Plastic Cup	87
Figure 68-Sketch of the First Borehole Tests, [cm]	89
Figure 69- Connection of Two Cartridges of Emulsion.	90
Figure 70- Sketch of Second Borehole Tests, [cm]	91
Figure 71-Comparison between Autodyn and Pressure Gauges, Big Garbage Bin ..	93
Figure 72-Comparison between Autodyn and Pressure Gauges, Bucket with Third Typology Guages	94
Figure 73- Absolute Error, Big Garbage Bin.....	96
Figure 74- Absolute Error, Bucket with Third Typology CCR.....	96
Figure 75- Blue: Column Charges Experiments, Orange: Pentolite Booster Experiment.....	99
Figure 76- Pentolite 50/50 in Borehole, Pressure vs Scaled Distance.....	100
Figure 77- Attenuation Curves, ST45: 45cm of Stemming, ST100: 100cm of Stemming, ST122: 122cm of Stemming, NOST: No Stemming Used	102
Figure 78- Parallel Holes Experiment, Blue: Pressures Detected, Orange: Pressures Calculated	103
Figure 79- Signal Conditioner's Datasheet by PCR	109
Figure 80-Emulsion Technical Datasheet, By Orica.	110
Figure 81- Pentolite 50/50 Booster, Technical Datasheet, by Orica.	111

INTRODUCTION

The explosive science seems to be very clear nowadays, since explosives are used in many applications. However, the science of explosive is still very young, even though it is well known, indeed the nonlinear interaction between chemistry and fluid mechanics that produce the rapid energy release known as detonation is still under study.

This science field is basically a coupling of chemistry and fluid mechanics. Nevertheless, the fluid-mechanical phenomenon of detonation is reasonably well understood, though, the detailed chemical reactions and thermos-mechanics that cause a detonation are still largely a mystery. This is due to two main reasons: first of all it is necessary to be aware that measurements in the interior of a detonating explosive are extremely difficult for a lot of reasons, such as the lack of proper and available (economically speaking) gauges, the difficulty to get data, the tough environment developed by the detonation (high energy, high temperatures, high pressures, high wave velocity, short time). The second reason is the most disappointing from the research point of view. Most explosive applications are in the fields of excavation, mining, or conventional munitions, in all these fields there are well established, albeit crude, “rules of thumb” as regards amount and configurations of explosive required to accomplish the task.

On the bright side though, in the last decades the need of understanding the details of energy release in explosives has been increased rapidly. Explosive systems have to show, nowadays, an extreme precision and efficiency in addition to ensuring safety. These needs have allowed to open a new chapter to the research in this a field, through new technologies able to get deep in these problems. For instance, now very powerful tools are available, such as Numerical simulations, Finite Analysis Methods, Computational Fluid Dynamics software and so on.

The purpose of this study is to analyse data, obtained from different experiments in different environments, which will be shown afterwards, and see how to link this data to the problems mentioned above. Therefore, throughout the measurements of the pressure shock waves, that were collected by means of different kind of pressure gauge sensors, the goal is to respond to different questions, and in some case, let the readers understand the huge potential of this field.

An explosive system requires, as previously said, extreme precision, efficiency and safety.

These three themes are very close each other, especially in blasting engineering.

In mining, as well as in excavation, the “decking technique” is well known; it refers to the axial or longitudinal decoupling of an explosive column by dividing it into decks spaced by gaps. These gaps are usually left with air although other materials such as sand or drilling debris can be used. For a given charge length, decking improves energy distribution along the hole; however, it will tend to generate an excess of fine from the sections of borehole in contact with the explosive and a poor fragmentation from the sections which are not. A problem arises from the need to prime each individual explosive deck, that introduces an element of risk as a consequence of explosive and/or initiator malfunction due to shock that could lead to misfires or propagation failures. A scheme is shown in Figure 1, besides, it is common knowledge that in some cases of Air Decking, subdrilling can be avoided, increasing the precision and the control of the blast, at the same time reducing vibrations and flyrocks.

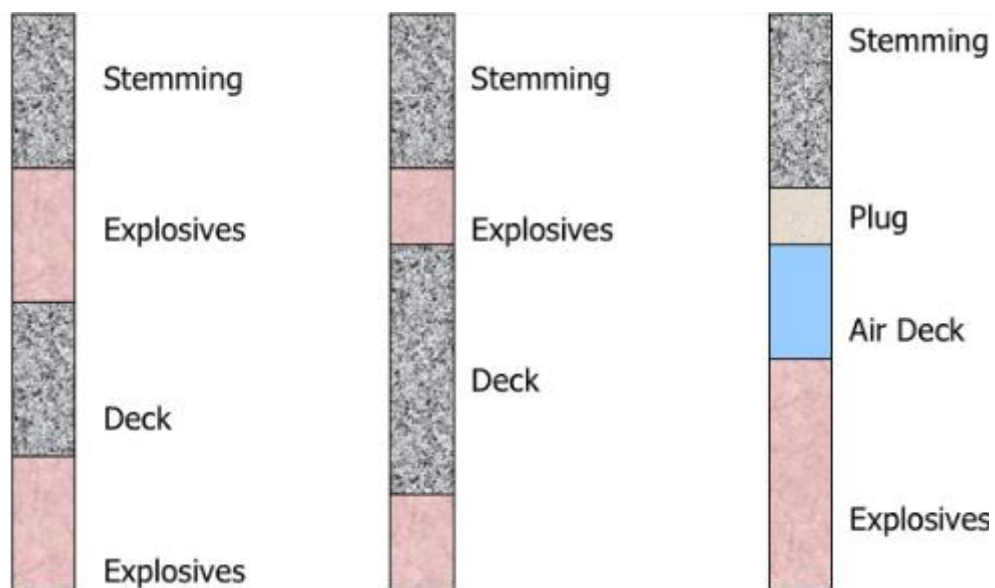


Figure 1-Decking technique, different typologies

One problem could be how to get close to the next explosive charge through the decking technique, avoiding sympathetic detonation and/or malfunctioning and/or desensitization of the other charge.

Remember: in this technique it is possible to delay each charge or to blast them simultaneously, depending on the required effect.

The pressure thresholds for those phenomena are known and published according to the kind of explosive as well as the type of initiation system and their brand. What it is unknown is the behaviour of the propagation of the shock wave through the medium, $P(t,d)$.

Another problem could be noticed in the other dimension, considering the lateral side: for instance, in an underground environment, where only one free surface is available (tunnels and shafts). as an example, a tunnel with parallel hole cut can be considered, Figure 2.

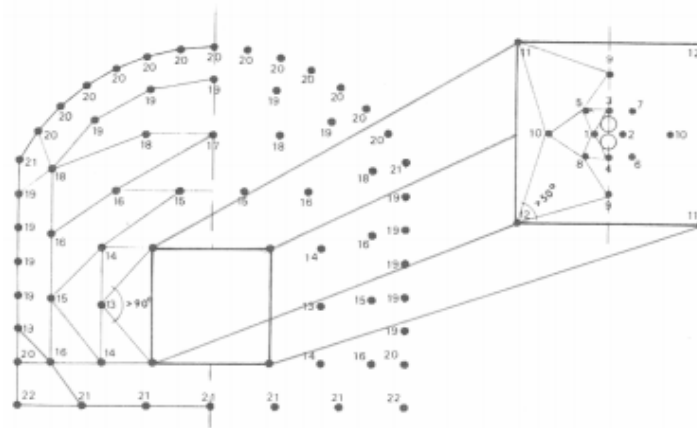


Figure 2- Parallel holes pattern

Observing the zoomed square on the right, parallel-holes cut with two dummy holes, it is known that in this kind of blasting, the efficiency depends on the delay sequence, indeed the correct timing improves the fragmentation of the whole cut, contributing to a better strata control and reducing the blast-induced vibrations.

1 PRESSURE CONCEPTS REVIEW

1.1 INTRODUCTION

To understand the phenomena, which are developed inside a borehole during an explosion process, in the simplest way, it can be useful to quote some statements of Bragg (1934). It will give us an idea very clear making simple examples.

Let us consider that the little balls in Figure 3 below are gas molecules

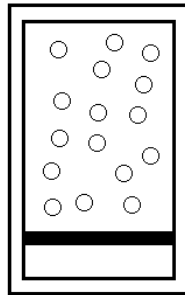


Figure 3- Bragg's Scheme.

As showed in Figure 3, the analogy is made by means of a billiard with a mobile edge, which can be moved upwards or downwards. If the molecules move the edge because of their movement, the work is carried out by their impacts against the edge, therefore a loose of their own energy will be noticed. However, by moving the edge towards them (upwards), the work would be carried out by the edge, thus in this case the molecules will get energy.

Now, in the case of an explosion, it is easy to deduce that in the first place the balls are stopped, thus, there is no movement and they are bonded to each other by chemical bonds, forming an explosive material. These molecules need an “initiation energy” for starting their reactions, namely, the breakege of their own bonds.

The pressure (thurst against the edge) depends on:

- the numbers of balls present on the table (density)
- the speed of the balls (temperature)

In Figure 6, ab easily understandable sketch is presented; the molecules are linked each other through a little wire which keeps a spring compressed, by breaking this little wire through, for instance, a match (i.e., the initiation), the spring will release its own elastic energy and the ball will start moving according to this.

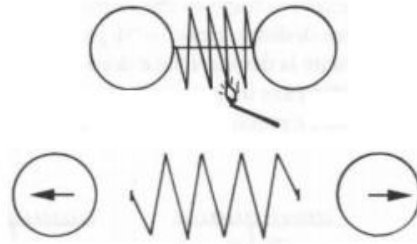


Figure 4- Sketch of the initiation, Source: Mancini & Cardu (2001)

1.2 EXPLOSION PRESSURES

From a damage control point of view, the most important parameters related to the performance of an explosive are the detonation pressure, the explosion pressure and the borehole pressure. The following figure, Figure 7, makes the concept clearer.

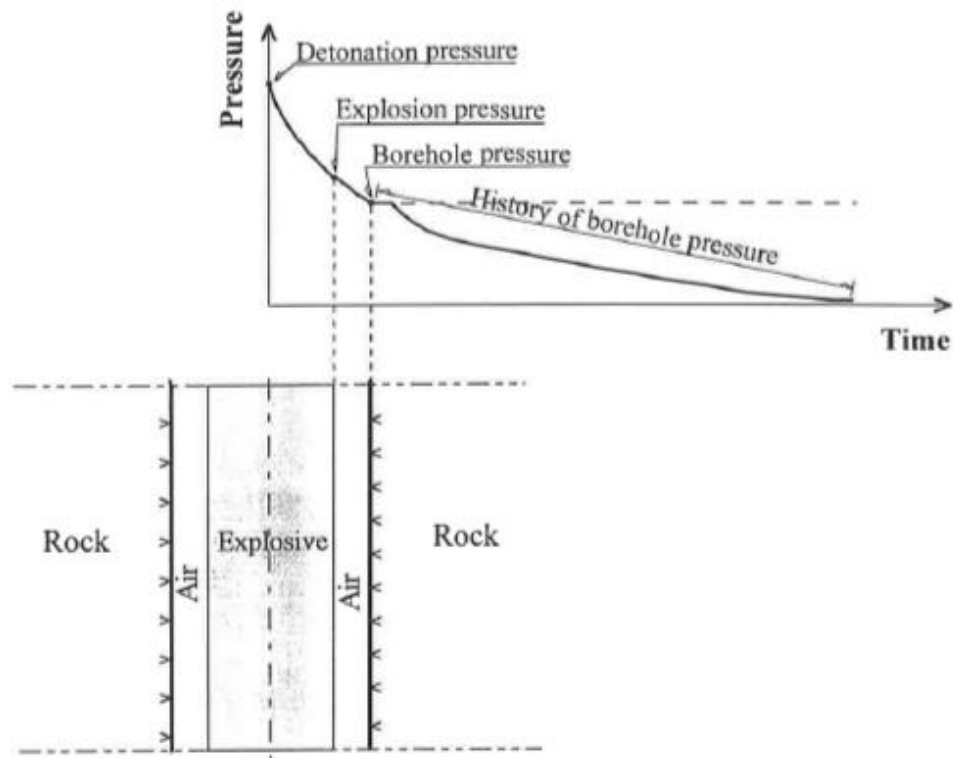


Figure 5- Definitions of some specific pressures on the pressure history in a blasting hole, Source: Shulin Nie (1999)

Let us regroup the pressures mentioned before under two families: pulsed pressures, due to a “dynamic load”, and “quasi-static” pressures, also known as “chemical pressure”, due to the containment of the gases in a little volume. The difference between two pressures is well explained in Figure 6.

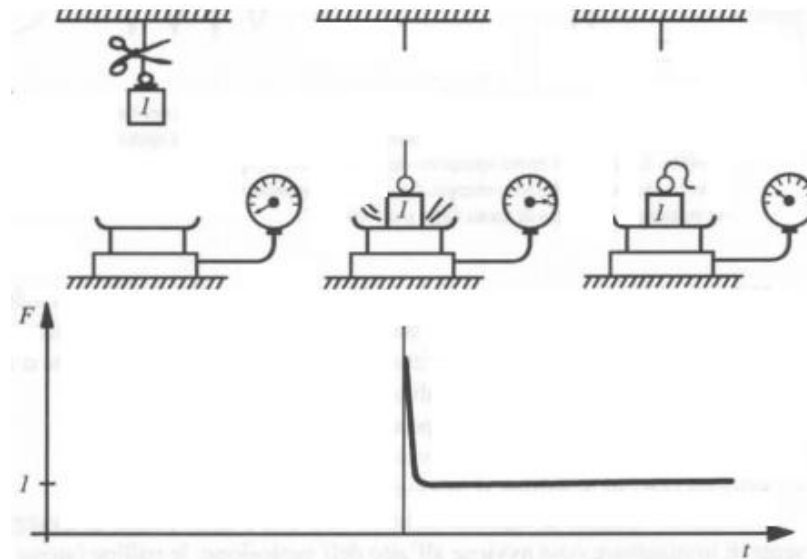


Figure 6- Differences among the pulsed load and quasi-static load. Source: Mancini & Cardu (2001)

A mass of 1 kg is hanged at a certain height above a dynamometer. By cutting the rope that is holding the hanging mass, the mass will fall in a short time, Δt , till it stops. The dynamometer in that short time, will record a heavy load (exactly the pulse) and it will be followed by a steady-low load, which simply is the weight of the mass.

The dynamic load is the force necessary to rescubf the mass velocity (Δv) in a the shock time Δt , namely:

$$F_d = \frac{M\Delta v}{\Delta t} \quad (1)$$

Instead, the steady load is just Mg .

Now, the analogy is clear, hence the pulse represents the dynamic pressure, instead the other, represents the chemical pressure, which can be conceived as Explosion and Borehole pressure, since those two appear right after the detonation phenomenon (depending on the design of the blast, as explained in 2.2.3 below).

1.2.1 Detonation Pressure

The detonation pressure is the pressure that develops behind the detonation front before any gas expansion takes place. This pressure is usually referred as the Chapman-Jouget state (CJ). For ideal explosives, full chemical reaction (complete oxidation) has been accomplished at this state; however, having to deal with non-ideal explosive product, the chemical reaction continues beyond the CJ state and into the expansion zone of the reaction products.

Thereby, the conservation of momentum equation describing shock phenomena, explained in Paragraph 2.4.2, the detonation pressure is given by:

$$P_d = \rho D u \quad (2)$$

where ρ is the original density of the explosive, D the velocity of the detonation front and u the particle velocity behind the detonation front. Rearranging equation (2) by changing the particle velocity u , it is possible to obtain the detonation pressure for a generic adiabatic expansion coefficient, always at the CJ state.

$$P_d = \frac{\rho D^2}{(1+\gamma_{CJ})} \quad (3)$$

where γ_{CJ} is the coefficient of adiabatic expansion at the CJ state. For condensed high-density explosives, (ρ between 1.0 g/cm³ and 1.80 g/cm³), γ_{CJ} is roughly equal to 3. By replacing this value in equation (3), the well-known expression used to estimate detonation pressure is obtained:

$$P_d = \rho \frac{D^2}{4} \quad (4)$$

1.2.2 Explosion Pressure

“Explosion pressure is that pressure exerted by the expanding detonation products when they occupy the original volume of the explosive charge”, (G.C.O. Silva ,2007). “By assuming the γ -law equation of state with a value of γ remaining constant throughout the expansion process from the state CJ state to the original volume of the charge, then the explosion pressure equals one-half the detonation pressure” (Zerrill, 1981). Therefore, using equations 3, 4, the corresponding pressure expressions are expressed as:

$$P_e = \frac{\rho D^2}{2(1+\gamma_{CJ})} \quad (5)$$

$$P_d = \rho \frac{D^2}{4} \quad (6)$$

1.2.3 Borehole Pressure

Borehole pressure is the pressure exerted by detonation gases expanding against the borehole's wall. When an explosive charge is loaded into the borehole, the borehole pressure and the explosion pressure are equivalent; however, it is possible diversify those pressures, for example let us considered a decoupled explosive charges. The borehole pressure in this case, results in a reduced value, which depends on the

extent to which the products of detonation are allowed to expand. By assuming that the expansion process from the explosion state to the borehole state is adiabatic (i.e. $PV^\gamma = \text{constant}$) with a constant γ coefficient, the borehole pressure (Nie, 1999) is given by:

$$P_b = P_e \left(\sqrt{\frac{L_e r_e}{L_b r_b}} \right)^{2\gamma} \quad (7)$$

As it is possible to notice from Equation 7, the borehole pressure, P_b , is function of the explosion pressure P_e , of r_e/r_b , (ratio between the charge and the blast hole), of L_e/L_b (ratio between the charge and the blasthole length) and γ .

To sum-up, it can be stated that:

the detonation pressure is a function of the explosive density, as well as the velocity of detonation and the coefficient of the adiabatic expansion; its amplitude is determined by the conservation of momentum equation (2.4.2). It is appropriate for ideal conditions, involving full chemical reaction at the CJ state, this behaviour is well represented by condensed high-density explosives. However, commercial explosives show a higher dependence on external and internal factors; let us list the most important ones: charge diameter, heterogeneity of the mixture and degree of confinement. These factors affect the explosives' ability to get to the full chemical reaction at the CJ state and, therefore, they will exhibit the non-ideal behaviour that characterizes most commercial products.

The explosion and borehole pressures are strictly related to the detonation pressure; hence, all it was said for the detonation pressure also apply. Besides, it is very common to take half of the value of the detonation pressure for expressing the amplitude of the explosion pressure; otherwise, the empirical relationships presented can be used to estimate it. The borehole pressure, in its turn, is expressed as a function of explosion pressure and it is estimated by assuming a constant value for the specific heat ratio during the gas expansion in the annular space created by the decoupled charge.

2 SHOCK WAVES

2.1 INTRODUCTION

First of all it is necessary point out some mechanical models and then proceed to develop the basic equations that describe the dynamic uniaxial strain, which is the direction where the shock travels.

2.2 QUALITATIVE DESCRIPTION OF A SHOCK WAVE

It is more than familiar the typical stress and strain curve, with a linear behaviour, the most common case is shown in Figure 7.

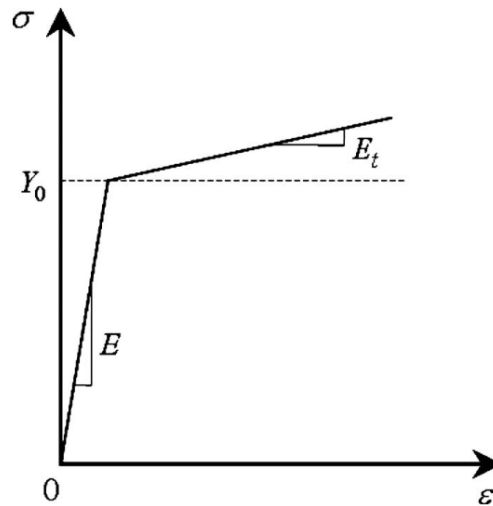


Figure 7- Linear Stress and Strain behaviour. Source: H.F. Abdalla et al. (2006)

That is the strain (amount of distortion) produced in a material is directly proportional to the stress placed on the material. Thus, the first trend, from 0 to Y_0 , visible in Figure 9, is surely linear with a known steep coefficient, E . However, after the Y_0 point, the diagram stress-strain suddenly changes its slope. This point is called the yield point or elastic limit, indeed when a material is strained beyond its elastic limit, plastic deformation arises.

In shock behaviour, only compressive stress and strain will be considered, furthermore, to keep the mathematics and models simple, uniaxial compressive stress and strain are considered. This means that the effects will be analysed along only one axis of a material. Thus, this assumption, which is a fair approximation, means that the systems have no an edge effect.

Taking in consideration the same material but applying a very high level of stress, it will behave differently; in fact, an elastic region will be noticed, followed by a combined Elastic-Plastic region, up to reach the plastic region, very close to a fluid behaviour.

In the elastic region, the sound velocity in the material is constant. The sound velocity, C , is proportional to the ratio of the change in pressure with change in density:

$$C = \frac{dP}{d\rho}$$

which means that in the elastic region, pressure and density are linearly related. However, beyond the elastic region, the wave velocity increases with pressure or density and the ratio P/ρ is not linearly proportional. Wave velocity continues to increase with stress or pressure throughout the region of interest. Thus, up to the elastic limit, the sound velocity in a material is constant. Beyond the elastic limit, the velocity increases with increasing pressure.

Let us consider the pressure wave in Figure 10; the pressure is low in point C; thus, C_c , the wave velocity, is low. Besides, the particle velocity, u_c , is fairly low, therefore, the velocity of the pressure wave, U , is low, $U=C_c+u_c$

At point B, the wave velocity is higher than at point C, since the wave velocity increases with increasing pressure (it is being considered the elastic region). The particle velocity is also higher, since the higher is the pressure, the higher is the particle velocity. Thereby, the pressure wave at point B is traveling faster than at point C. The same applies to point A, since it has a faster wave velocity than point B.

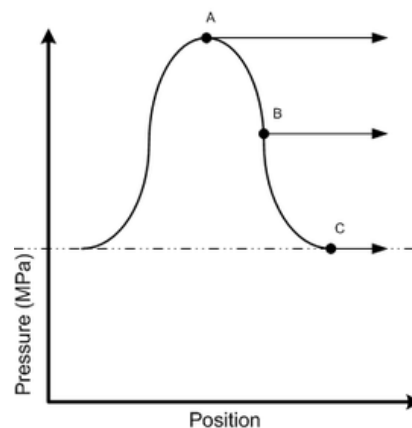


Figure 8- Pressure wave at high pressure. Source:

https://en.wikibooks.org/wiki/Engineering_Acoustics/Qualitative_Description_of_Shocks

The resulting effect is shown in Figure 11, where it can be noticed that the semi-wave, A-B-C, keeps getting steeper till reaching the point in which A-B-C are on the same straight line, on the same straight line.

When the wave assumes this vertical front, it is called a shock wave.

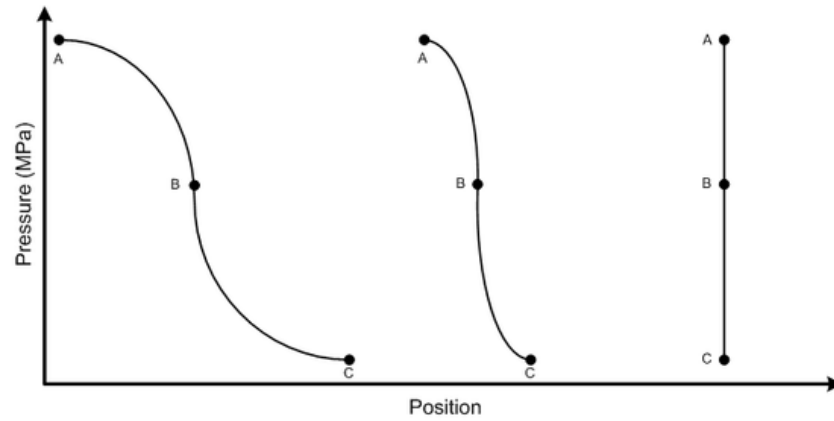


Figure 9- Shocking-up of a pressure wave. . Source:

https://en.wikibooks.org/wiki/Engineering_Acoustics/Qualitative_Description_of_Shocks

Take into account that there is not a smooth transition between matter in the “head” of the wave and the matter in the “tail” of the wave. The material in fact “jumps” from nonshocked to shocked state. This is called a discontinuity.

2.3 ATTENUATION BEHIND SHOCK WAVES

A smooth front pressure disturbance will “shock-up” due to the fact that the wave speed increases with increasing pressure. Viewing the square wave in Figure 12, assume that it is going through a material.

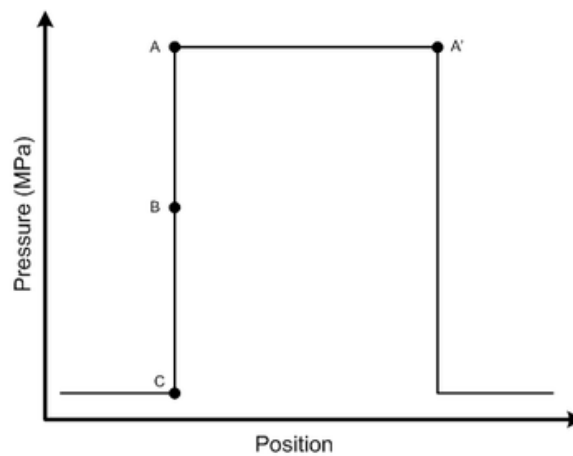


Figure 10- Square-wave shock. . Source:

https://en.wikibooks.org/wiki/Engineering_Acoustics/Qualitative_Description_of_Shocks

The front of this wave is already a shock; so let us inspect the back part of the wave. The material front of point A is at high pressure. It is also traveling at a certain particle velocity u , and density ρ is high. The speed of the rear of the wave is obtained by summing the particle velocity and wave speed, as explained before. Now, since the back is moving into a higher-density region compared to the front and is even encountering a faster material or particle speed than the front, it is traveling faster than the front. It therefore tends to catch up rapidly with the front. Thereby as the shock wave travels along, the rear of the wave, either called rarefaction wave, smears out the back and eventually catches up to the shock front. Yet, it is traveling faster than the front and thus, the upper parts of the rarefaction wave starts “whittling down”, namely, begins to decrease the pressure in the front, until when the pressure is reduced to the region of elastic behaviour, and the shock has decayed to a sound wave; the whole evolution of the events is shown in Figure 13.

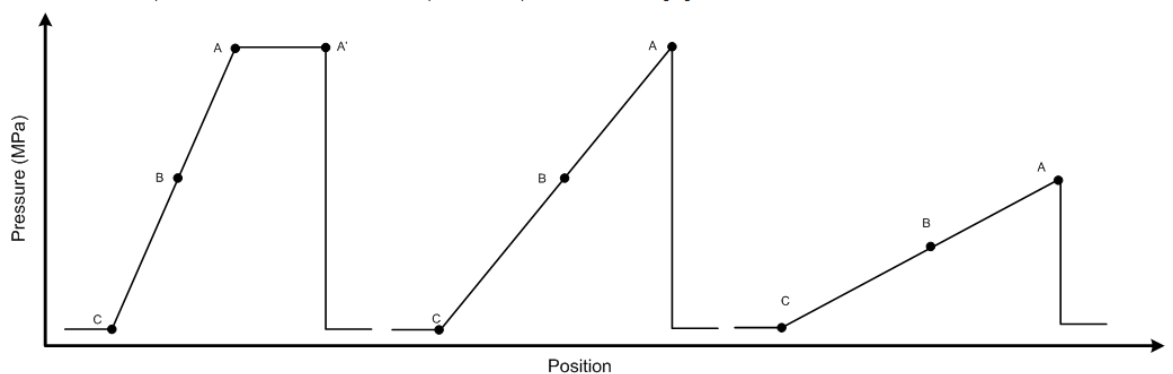


Figure 11- Attenuation of a shock-wave shock. . Source:

https://en.wikibooks.org/wiki/Engineering_Acoustics/Qualitative_Description_of_Shocks

In summary, it has been said that:

1. Shock waves occur when material is stressed well beyond its elastic limit by a pressure wave.
2. Since the pressure-wave velocity increases with pressure above the elastic limit, a smooth pressure wave “shocks-up”.
3. As the rarefaction wave through the shocked region moves faster than the shock front, the shock is attenuated from behind.

In Figure 13 is shown a pressure trend due to a shock wave by detonating explosive (PENT) in water. It is possible to notice the rarefaction phenomenon that takes place suddenly after the peak of pressure (over 0.4 GPa). Beside it is interesting to look at

the magnitude of time, μs , especially the interval between $0.05 \mu\text{s}$ and $0.28 \mu\text{s}$ which marks the entire rarefaction time ($\Delta t=0.23 \mu\text{s}$).

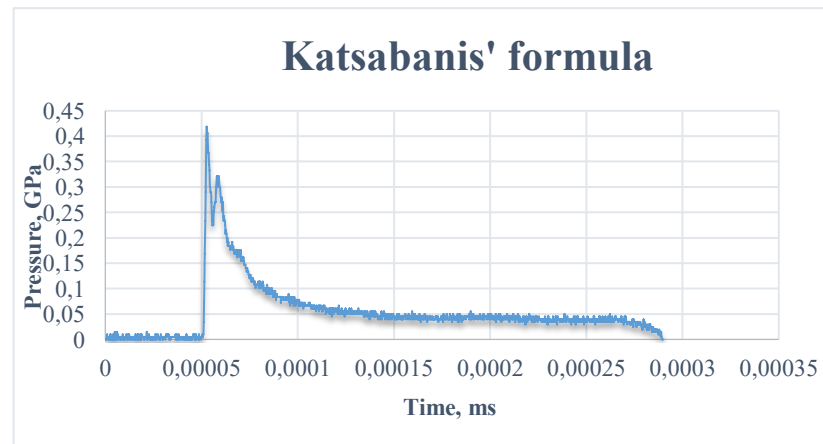


Figure 12- Pressure-Time.

2.4 RANKINE-HUGONIOT JUMP EQUATIONS.

Remembering what said previously about a shock wave, where the front was referred to as discontinuous, the original states of particle velocity u_0 , density ρ_0 , internal energy E_0 , and pressure P_0 , suddenly change across the shock front. They will not variate gradually, indeed, they will discontinuously jump, in an abruptly way, from unshocked to shocked values. Thus, there are five variables to deal with; hence, are needed five relationships to solve the problem.

As in every physics problem, there are some trustworthy equations, which most of the time play fundamental roles; indeed, the first three relationships that can be derived by knowing that mass, momentum, and energy across the shock front must be conserved. These balances do not depend upon a process path but simply upon the initial and final states of the material. These three equations take the names of “Rankine-Hugoniot jump equations”.

2.4.1 Mass balance

As known, the mass balance equation implies the mass is neither created nor destroyed, therefore:

$$m = \rho v \quad (8)$$

where m is the mass, ρ is the density and v is the volume.

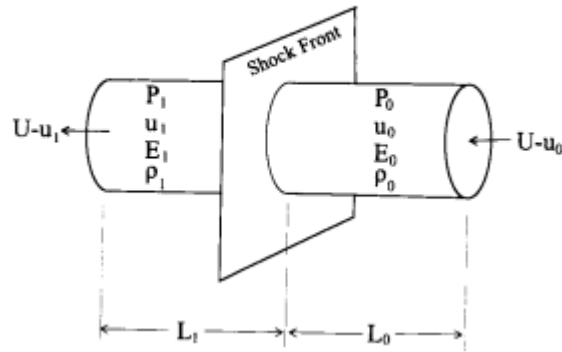


Figure 13- Control Volume or Mass Passing Through a Shock Front. Source: P.W. Cooper (1997)

$$v = AL$$

By looking at the system shown in Figure 13 the parameters considered are:

A is the cross-sectional area of the control volume.

L is the length, which in this system can be found as the distance that a particle runs along (it its relative to the shock front), which is the velocity relative to the shock front multiply the time that the particle took to run along that length; this means:

$$L = t * \text{velocity, relative}$$

According to the statements written above, there will be a mass entering (subscript 0) and mass leaving (subscript 1):

$$\rho_0 AL_0(U - u_0) = \rho_1 AL_1(U - u_1)$$

Rearranging the equation and considering $v = \frac{1}{\rho}$:

$$\frac{\rho_1}{\rho_0} = \frac{U - u_0}{U - u_1} = \frac{v_0}{v_1} \quad (8)$$

2.4.2 Momentum Balance

The momentum balance equation has to imply that the rate of change of momentum (considering always the control mass in Figure 13), from the un-shocked state (state 0) till reach the state after the shock (state 1) must be equal to the force applied to it.

The force applied is hence calculating throughout the pressure difference across the shock front multiply the area above which it is applied, always considering our control volume cross-sectional area

$$F = (P_1 - P_0)A \quad (9)$$

The rate of change momentum is:

$$r = (mu_1 - mu_2)/t \quad (10)$$

Combining the equation (9) with the (10) and rearranging the equation (rewriting the term m in function of ρ), the momentum equation, considering the particle velocity at state 0 equal to 0, is obtained:

$$P_1 - P_0 = \rho_0 u_1 U \quad (11)$$

However, for a generic case of u , it is expressed as:

$$P_1 - P_0 = \rho_0(u_1 - u_0)(U - u_0) \quad (12)$$

2.4.3 Energy Balance

The energy balance is the law of conservation of energy, which means that energy can be neither created nor destroyed. The rate of work done in this system is expressed in term of internal energy, E , and specific internal energy, e , is:

$$\frac{E}{t} = (\rho_1 AL_1 e_1 - \rho_0 AL_0 e_0)/t$$

The rate of change of kinetic energy is:

$$\frac{KE}{t} = \left(\frac{1}{2} \rho_1 AL_1 u_1^2 - \frac{1}{2} \rho_0 AL_0 u_0^2 \right) / t$$

Developing the calculations, and combining the equation with Equation 7 and Equation 12, the energy equation is developed, and as before, by considering the particle velocity at state 0, u_0 equal to 0, it is possible to rewrite it as:

$$e_1 - e_0 = \frac{1}{2} (P_1 + P_0) (v_0 - v_1)$$

However for a generic u_0 is:

$$e_1 - e_0 = \frac{1}{2} \left(\frac{P_1 u_1 - P_0 u_0}{\rho_0 (U - u_0)} \right) - \frac{1}{2} (u_1^2 - u_0^2) \quad (14)$$

Now, making a balance of the equations and the unknowns (3-5) it is possible to figure out that this system is unsolvable, so far. Thereby, in order to solve the shock problems, it is needed two more relationships. The solution was given throughout an empiric approach, by H. Hugoniot (1889).

2.5 THE HUGONIOT PLANES

As written in paragraph 2.4.3, these new relationships take the names of “Hugoniot equations”.

2.5.1 The Hugoniot equation

At this point it is needed a relationship which will link all the parameters at stake. This relationship is called equation of state (EOS). The EOS will give all the information about the equilibrium at a certain thermodynamic state; it will be in terms of specific internal energy, pressure, and specific volume. Unfortunately, a general EOS for all the materials is not available, neither possible to obtain; however, there is, of course, the ideal gas equation, $PV=NRT$, where RT is related to the specific internal energy, even if the case under study is not referred to ideal gases. If there were an EOS, $e=f(P,v)$ then it could be combined with the energy jump equations and the energy, e , term could be deleted, giving us the relationship $P=f(v)$.

Therefore, the problem will be solved throughout an empirical approach, by looking at certain relationships between the unknowns.

Back in the days, a lot of experiments were carried out by Rankine and Hugoniot (1870-1880) in order to obtain such relationships, and it was found (as first equation) that the shock velocity was linearly dependent to the particle velocity, for most materials:

$$U = C_0 + su \quad (15)$$

The Hugoniot equation (Equation 15) solves, in part, the problem. By looking and representing this equation in a plane $U-u$, it is possible to notice its linear behaviour, besides the other planes that are worth it to be represented, as well as analysed are: the $P-v$, and $P-u$ plane. Such planes are considered the most important for giving a solution to shock wave problems.

2.5.2 The $U-u$ plane

The first value of the $U-u$ relationship is linear. This means that the shock wave velocity U and the particle velocity u , for a given material, at a known number of shock states, can be plotted on this plane, strike a straight line through the data points, easily find the $U-u$ Hugoniot equation. This is shown in Figure 16. The equation for this linear relationship is again $U=C_0+su$. The constant C_0 is named the

bulk sound speed, but could be misled, since C_0 has no real physical meaning, it is just the shift in y-axis, which intercepts on a straight line drawn through the data points. U , C_0 are expressed in km/s and the term s is dimensionless. Unfortunately, there is no simple correlation of the constants C_0 or s with any other material properties. Therefore, it is possible not to find the Hugoniot for a material in any references, the only way is to use the $U-u$ Hugoniot values of another material that is similar to the one of interest. Then trying to match, as much as possible, the materials by chemical composition and physical proprieties, and besides try to match by mechanical state.

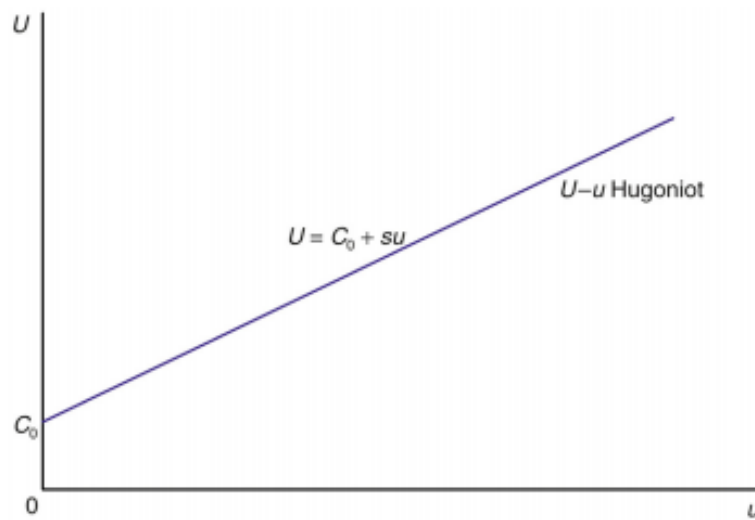


Figure 14- $U-u$ Hugoniot. Source: Z.X. Zhang (2016)

2.5.3 The $P-v$ Plane

By combining the $U-u$ Hugoniot equation with the momentum (12) and mass equations (8), and implying the values of $P_0=0$ and $u_0=0$ the particle and shock velocity terms ca be deleted and thus can be obtained the following expression $P=f(v)$.

$$P = C_0^2(v_0 - v)[v_0 - s(v_0 - v)]^{-2} \quad (15)$$

This is the Hugoniot equation in the $P-v$ plane. It is possible to see the $P-v$ plane in Figure 15. The isentropice, namely, the path that describes all the states with same entropy, is smooth and in fact there is no jump or discontinuities, it differs from the Hugoniot. It has been noticed that a relief wave is a continuous process and its trend would be along the “unloading” isentropic. The Hugoniot represents the place of all possible states behind the shock front, there is though, a line that joins the initial and

final states on the P - v Hugoniot, this line represents the jump condition and it is called Raleigh line. By deleting the particle velocity term u by rearranging the mass and momentum-jump equations, and implying $u_0=0$, the jump equation is given by:

$$P_1 - P_0 = \frac{U^2}{v_0} - \frac{U^2 v_1}{v_0^2} \quad (16)$$

Equation 16 describes the Raleigh line, and besides the slope of this line is dP/dv_0 , namely, U^2/v_0^2 . By knowing the initial and final P - v states of shock, the shock velocity U , can be calculated throughout the Raleigh line's slope. The fifth variable has been, then, fixed by specifying it as a boundary condition in the calculation. Moreover the in Figure 15 it has to be specify that the point P_l, v_l marks the upper limit of the elastic-plastic stress-strain relationship, and as a matter of fact, the P_0, v_0 point marks the upper limit of the elastic region. Furthermore, "by shocking a material, which means going through the Raleigh line from the state P_0, v_0 to P_l, v_l and allow a relief wave to bring it back to P_0, v_0 (passing through the Hugoniot curve) there will be a change in specific internal energy. Thus, in the process of shocking and then relieving the material, the final specific internal energy is increased by the amount equal to the difference between the area under the Raleigh line and the area under the Hugoniot segment. Changes in internal energy are changes in thermal state; therefore, the temperature of the material must have increased." P.W. Cooper (1997).

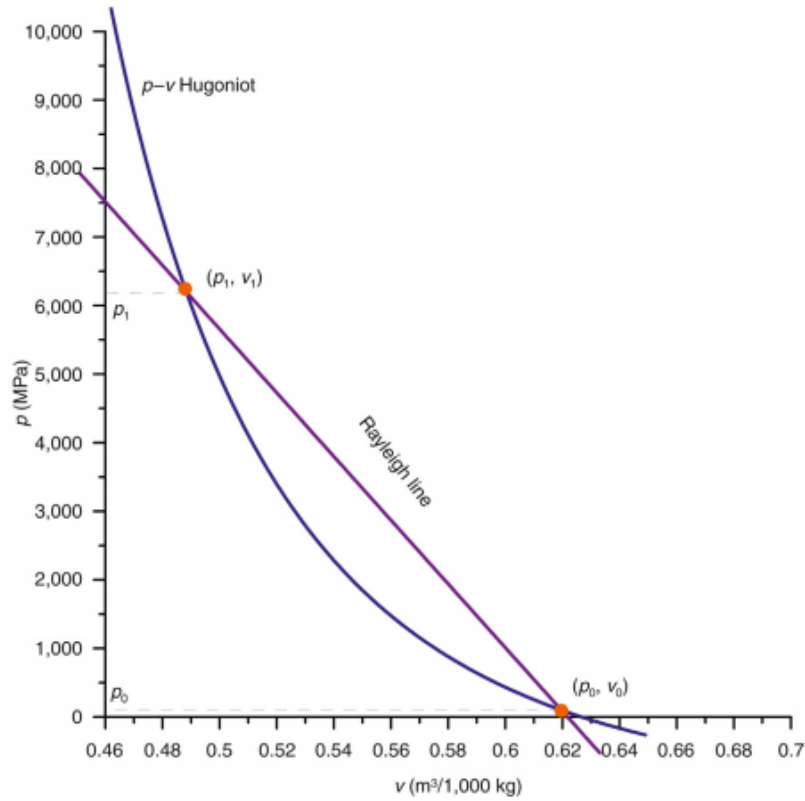


Figure 15- A P - v Hugoniot for TNT (cast). Source: Z.X. Zhang (2016)

2.5.4 The P - u Plane

Again, starting with the momentum and U - u Hugoniot equations, this time we will manipulate the equations to eliminate U , leaving P - u

$$P_0=0, u_0=0;$$

$$P_1=\rho_0 u_1 U$$

$$U=C_0+su$$

$$P_1=\rho_0 u_1 (C_0+su_1)$$

So far calculations were developed on the P - v Hugoniot, always allowing u_0 , the initial material particle velocity, equal to zero. This, in somehow, meant to say that the analysis of the problem is made throughout Lagrangian coordinates. Now, by allowing a different state of the material in u_0 , namely a value $u_0 \neq 0$, and by changing u_1 (Lagrangian system) to $(u_0 - u_1)$, the Eulerian system expression is obtained on behalf of the particle velocity:

$$P_1=\rho_0 u_1 (C_0+su_1) \text{ (Lagrangian) (17)}$$

$$P_1=\rho_0 C_0 (u_1-u_0) + \rho_0 s (u_1+u_0)^2 \text{ (Eulerian) (18)}$$

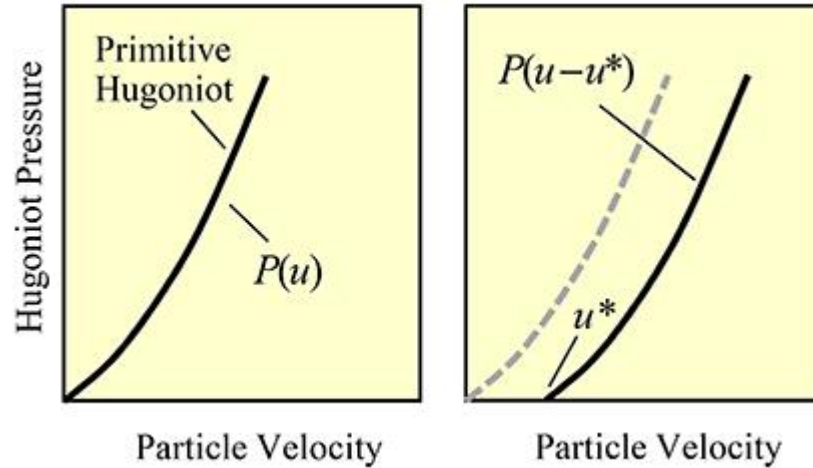


Figure 16-P-u Hugoniot, Lagrangian, Eulerian. Source: D. Grady (2017)

The next implication to notice is that, since that velocity is a vector quantity, it has a direction in fact. Equation 17 and Equation 18 are plotted in Figure 17 through the $P-u$ Hugoniot for a material where the shock is travelling from rightwards (a right-going shock). If the shock travels from right to left, it can be surely claimed that the particle velocity is equal to $-(u_1-u_0)$. For that case, the Hugoniot equation for a rightwards shock in Equation 16 would not be corrected. In order to find the Hugoniot for a left-going shock, let us step back again to the $P-u$ plane and modify the term (u_1-u_0) in $-(u_1-u_0)$.

$$P_R = \rho_0 C_0 (u_1 - u_0) + \rho_0 s (u_1 + u_0)^2$$

Shock wave's equation right-going.

$$P_L = \rho_0 C_0 (u_0 - u_1) + \rho_0 s (u_0 - u_1)^2$$

Shock wave's equation left-going.

“It is the left-to-right mirror image of the right-going Hugoniot, and it too “slides” back and forth along the u axis depending upon the value of u_0 . The slope of the line connecting two states, before and behind a shock, on the left-going Hugoniot is $-\rho_0(U-u_0)$, where the minus sign means that the shock is moving towards the left” P.W. Cooper (1997).

All these explanations that have been said so far, allow to solve the problem related to initial and final states of the shock waves, obviously nowadays, do exist different tools, numerical simulators, FLACs and so on, which allow to analyse and solve in prompt and efficient way this troubles. In this paper will be used the Code Autodyn, thereby throughout different simulations, will be given different comparisons among the experiments and the theoretical data.

2.6 SHOCK WAVE ATTENUATION, RAREFACTION WAVES

As anticipated in paragraph 2.3, the rarefaction phenomenon attenuates the pressure behind the shock front. Thus, something more can be said about this important phenomenon without looking at its development, which is complicated since thermochemistry and thermodynamics equations have to be managed, as well as recall the Hugoniot equations.

First of all, “rarefaction” could be found under different names in literature, such as relief wave, unloading wave, and Taylor wave. A rarefaction wave could be expressed as the progression of particles that are accelerated away from shocked front. It indeed, will travel in the opposite direction of the acceleration of the particles, this is considered to be the opposite of a shock wave, in which in fact, the particles are accelerated in the same direction of the shock. On the contrary, a rarefaction wave is spread in space, and it does continue to spread with time. This is due to the fact that an expansion of the high-density material to a lower density has its own time. Thus, the velocity of a rarefaction wave is in function of time. In the following, some characteristics of the rarefaction wave are provided:

- Interesting cases of rarefaction wave will be mentioning; for instance, (1) a first case could be by means of explosive detonation, where take place a shock wave, and hence, there will be a rarefaction wave, which will be due to the fact of the releasing of the shocked material. (2) A second example could be when a shock wave travels from a high shock impedance material to a low impedance one, see Paragraph 2.7. It is well known that there will be the occurrence of a rarefaction wave because of the high impedance material, which will reduce the pressure. (3) The last one could be when a shock wave propagates to a free surface; in this case, a rarefaction wave is caused.
- “The unloading of a rarefaction wave is along a continuum (isentropic) that is approximated by the Hugoniot” Z.X. Zhang (2016).
- The particle-moving direction in a rarefaction wave will be always against the direction of the rarefaction wave, in the opposite sense. On the other hand, the particle movements and the shock wave are concurrent in direction.
- A rarefaction wave is dependent on different factor, indeed it can be affected by material properties, boundary conditions, etc. Those factors include the

explosive properties, length and stemming material, charge parameters and obviously the rock properties.

2.6.1 Results of Shock Wave Attenuation in Different Materials

It is well known that in solids will take place a decrease of shock wave velocity, since there are interaction between rarefaction waves and other attenuation mechanisms, thus, this fact will lead the shock waves to become elastic waves.

Considering now a shock wave, generated by an explosion in an plastic inert specimen. By knowing the mass of the explosive, can be affirm that the pressure behind the shock front decreases rapidly, indeed there is an instant drop, such drop is due to rarefaction waves. The peak pressure decays following a exponential law, as the wave propagate outward because the energy distributed over the constantly increasing area, and besides, it is due to finite dissipation of energy in the transition through shock front. Figure 18 (left) shows a test set up for loading the shock waves in solids by contact explosive detonation and Figure 18 (right) shows progressive attenuation of the peak shock pressure with distance travelled in the solid specimen. Khurana et al. (2012).The peak pressure and the shock wave velocity U , decrease until the shock wave turns out in an elastic wave. Since the sound velocity is increasing function of pressure, the shock pulse becomes broader with distance travelled in solid specimen.

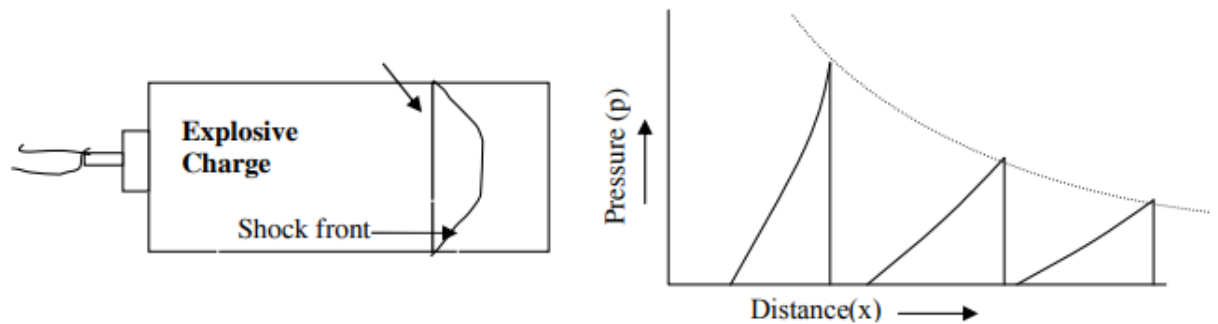


Figure 17-Test set up (left), Attenuation of peak pressure P with the distance travelled in solid specimen (right). Source: Khurana et al. (2012).

This decrease of pressure of shock wave, shown in Figure 18 right, which is travelling a solid material, is strictly dependent on the pressure gradient in non-uniform wave profile behind the shock front and the ratio of velocities of rarefaction wave and the shock wave in the specimen. All of this can be summed up by

Equation 18 where the variation of pressure with respect to the space is equal to what written below. Knowing that U is the velocity of the shock front, the pressure can be calculated from the shock jump condition:

$$P_1 = \rho_0 u_1 U$$

Shock velocity and particle velocity are well related, as seen in the past paragraphs, to the Hugoniot equation:

$$U = C_0 + su$$

The pressure attenuation with distance is written as:

$$\frac{dP}{dx} = \left(\frac{u_p + c}{U} - 1 \right) \frac{dP}{ds} \quad (18)$$

where c is sound velocity in compressed solid, dP is change in pressure over a distance dx in solids and dP/ds is pressure gradient behind the shock front. The pressure gradient dP/ds is a function of the length of explosive. In the near region of shock loading the shock velocity attenuates according to an exponential law:

$$U = U_0 e^{-\alpha x} \quad (19)$$

where U_0 is the amplitude of transmitted shock velocity at the explosive solid interface and is attenuation constant, α is the attenuation coefficient and it depends on the material, incident shock velocity and shape of the shock front.

It is possible set the thing in terms of pressure as well; Equation 19 simply describes an exponential decaying, which is already well known from the experiment, since the shock velocity U is strictly linked to the pressure P , and it is possible to express it throughout the same law:

$$P = P_0 e^{-\alpha x} \quad (20)$$

2.7 SHOCK PROPAGATION

When the initial states, P_0 and u_0 , are equal to zero, the momentum equation (12) could be rewritten as: $P = \rho_0 u U$. The product $\rho_0 U$ is called shock impedance, which is similar to the characteristic impedance of an elastic medium, besides in literature this impedance is usually expressed by: $Z = U\rho$.

The case in which a shock wave is travelling from material A (left, blue) to material B (right, green) is shown in Figure 18, there are three different possible cases that can take place: (1) $Z_A < Z_B$: (2) $Z_A > Z_B$: and (3) $Z_A = Z_B$. These cases could be expressed as applied problems, such as: (1) considering a deck-charge blasting when

shock waves travel from one deck to another; (2) in normal blasting when shock waves propagate from the explosive to stemming; (3) in normal blasting when shock waves go into rock mass from the blasthole. The most interesting case among the ones mentioned is the (2) case, which is suitable for the purpose, as well as useful to understand the propagation of the shock wave through the stemming, and thus, to get the shock wave pressure which can reach another detonator placed in another generic deck, as shown in Figure 1 .

Let us suppose that a shock wave a in material A travels into B, it is known that there are also two more shock waves generated: one is the reflected wave that is going back to A from the interface, and one shock wave going into material B. Therefore, there are three Hugoniot curves. The wave that is going back into material A is reducing its pressure from P_1 down to P_2 . It would be possible to refer at this shock wave as a rarefaction wave, since its attenuation. In this case, the reflected wave is diffuse. Basically, this phenomena is still shown in Figure 18, where through the $P-u$ plane is noted that the curve from the original shock state in material A goes to lower pressure, then, it is formed at pressure P_2 and is going into B, reaching the material in B to a new state 2. “The Hugoniot curve for this shock in B is over the Hugoniot curve for the original shock in A, since the shock impedance of B is greater than that of A. It is an isentrope, not a Hugoniot curve. It can be calculated if the material properties are known, or measured by experiments.”, Z.X. Zhang (2016).

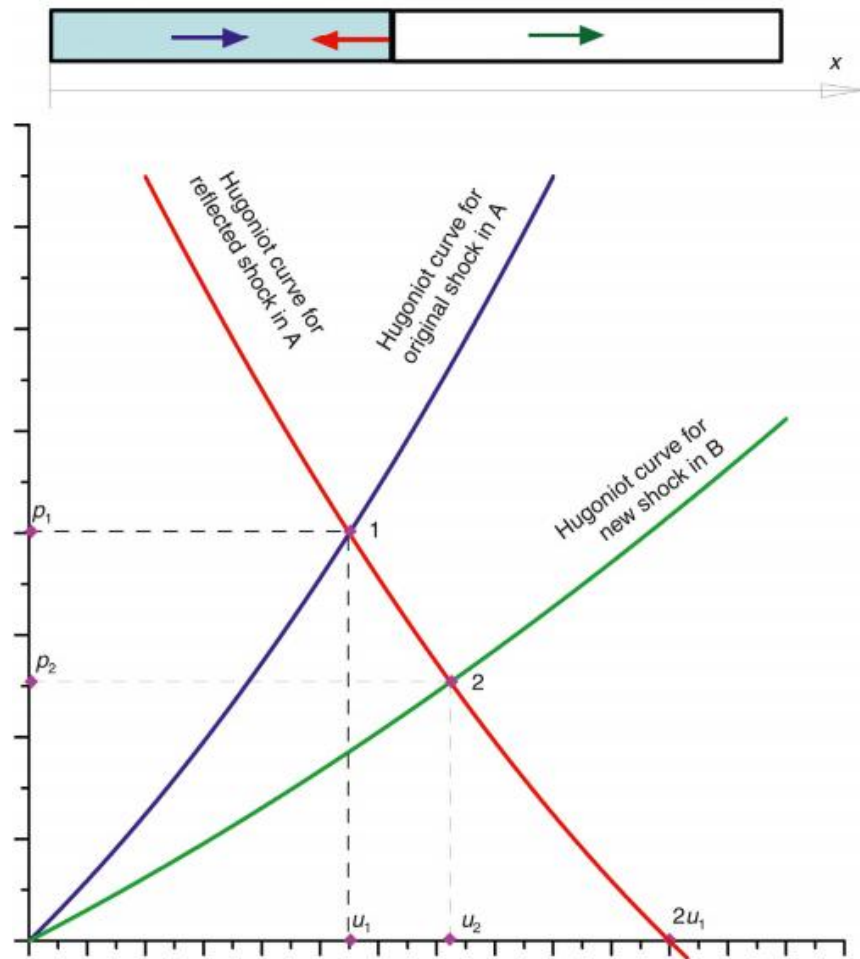


Figure 18- Example of shock wave travelling in two material; $Z_A > Z_B$. Source: Z.X. Zhang (2016)

The isentropic centred at the shock state and the Hugoniot curve centered at the same state are tangent at second order, and make a smooth curve through the centering point. In many cases, particularly with metals that are not too different in shock impedance, for the reflected rarefaction wave, the Hugoniot curve can be used for the reflected shock to replace the isentropic for the rarefaction wave as an approximation. Figure 18 shows the three Hugoniot curves and the final states. In conclusion, it can be stated that when a shock wave travels from a high to low impedance, the shock wave decreases in pressure. Therefore, the particle velocity increases, u_2 .

The problem can be solved

First step:

$$P_1 = \rho_{0A} u_1 (C_{0A} + s_A u_1) \quad (21) \text{ Blue Curve}$$

By knowing pressure P_1 the particle velocity u_1 can be easily calculated from the Equation 21 here.

Second step:

The Hugoniot for the new shock (or reflected shock) traveling in the negative x direction in the “donor” is:

$$P_L = \rho_0 C_0 (u_0 - u) + \rho_0 s (u_0 - u)^2 \text{ Red Curve. Indeed left-going.}$$

where $u_0 = 2u_1$

Thus, the Hugoniot curve for reflected shock in A can be obtained. The Hugoniot for the new shock traveling in the positive x direction, in the stemming is:

$$P_2 = \rho_{0B} u (C_{0B} + s_B u) \text{ Green Curve.}$$

Therefore, P_2 and u_2 can be obtained, which will be less than the original values at state 1.

2.8 COLLISION OF TWO SHOCK WAVES

The collision phenomenon would be useful for understating malfunctioning, desensitization as well as sympathetic detonation.

However, just a simple example will be provided. In the following case, it is supposed to initiate simultaneously two different detonators placed inside a blasthole filled of emulsion for instance, the case is the one shown in Figure 28 right. Hence, let us assume the shock waves are traveling towards each other and besides, they have the same pressure. Also consider that as positive direction (shock A, Figure 19) in the explosive (one-dimensional). In the same explosive there is another shock traveling in negative direction (shock B, Figure 19) on course for a head-on collision. When the two shock waves approach each other, the collision will cause two new shock waves that are reflected back in direction. This problem could be solved throughout the two Hugoniot curves, which afterwards will provide the new reflected waves.

Starting from the first curve, the new reflected wave will be negative in x direction.

This Hugoniot is coming from state (p_1, u_1) , and u_1 is positive; as it can be seen in Figure 19. The Hugoniot curve for the initial shock A ($u_0=0$) has equation:

$$P = \rho_0 C_0 u_1 + \rho_0 s u_1^2$$

Now, giving just some numerical values; $p=p_1=p_2=15$ GPa, the velocity u_1 as well as u_2 can be easily be found. The Hugoniot curve for the new shock in the negative direction (reflected shock A) must be rotated around this point and will intercept the $p_0=0$ or u axis at $2u_1$; its equation is

$$P = \rho_0 C_0(2u_1 - u) + \rho_0 s (2u_1 - u)^2 \quad (21)$$

Therefore, the reflected shock B, will be:

$$P = \rho_0 C_0(u - 2u_2) + \rho_0 s (u - 2u_2)^2 \quad (22)$$

The solution for the particle velocity after the interaction can be obtained from equating the two Hugoniot Equation (21, 22) and the result in this case is $u_3=0$

Then the pressure at the interaction can be obtained by using this particle velocity in either Equation 21, 22.

Note that $p_3 > p_1 + p_2$. In other words, the shock pressure caused by the shock wave collision is much greater than the sum of the two original shock waves.

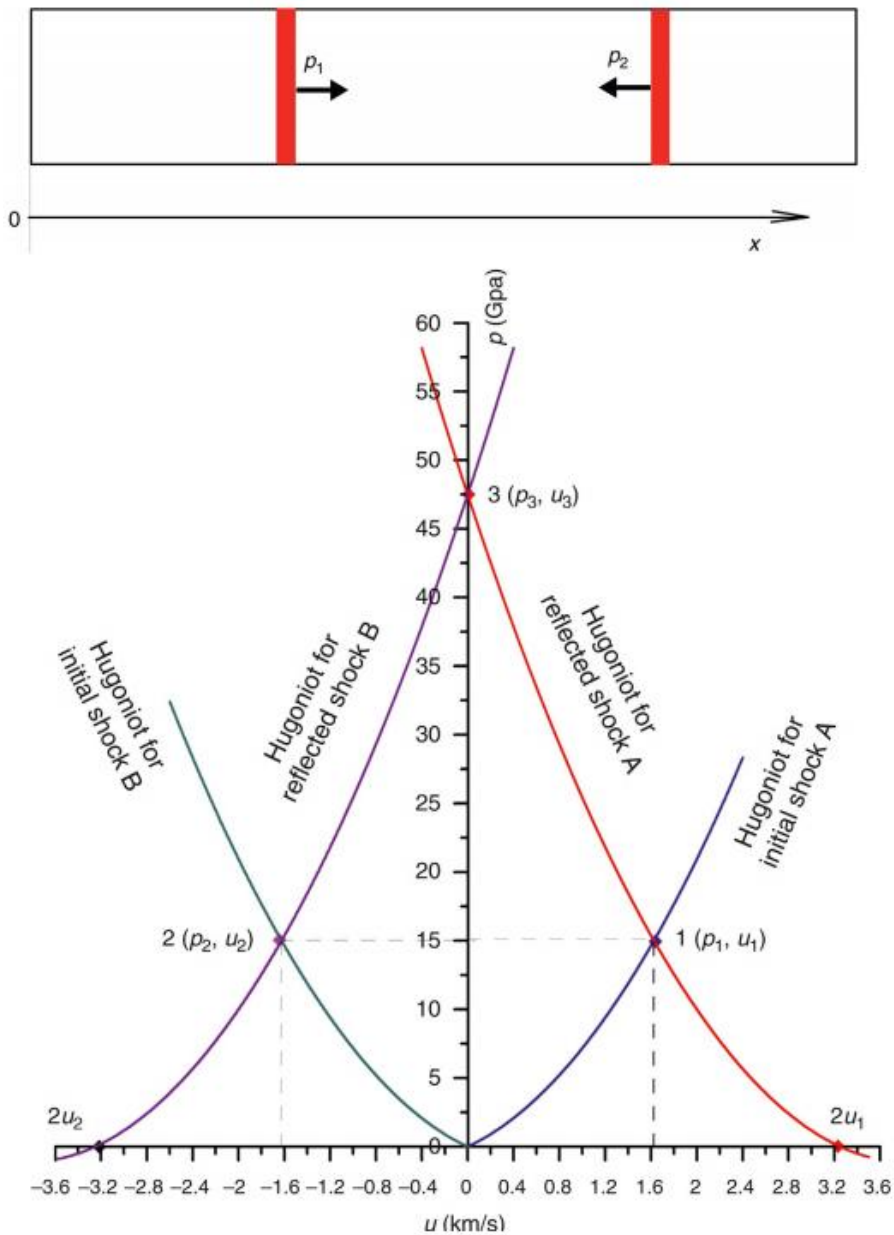


Figure 19- Up, Coordinates to shock collision; Down, Solution for P_3 due to their collision. Source: Z.X. Zhang (2016)

2.9 UNDERWATER EXPLOSIONS

It would be interesting to have a look at different environments such as underwater, where the problem can be simplified, considering that this kind of experiments are valid only in water.

There are many aspects of underwater explosions that must be studied in order to properly understand the development and propagation of the dynamic shock loading through the fluid. In this case, it is interesting to look at R.H. Cole researches (1948), where he carried out different measurements to figure out the magnitude of the dynamic pressure for different kind of explosives. Cole came up to a solution through an empirical formula, based both on statistical interpretation of his measurements and on the so called Principle of Similarity. The principle of similarity says: “suppose that measurements of pressure have been made at a distance r from a charge of given dimensions at a time t after it is initiated and that a new experiment is arranged in which all the linear dimensions of the charge are changed by a factor λ . The principle of similarity asserts that the pressure and other properties of a shock wave will be unchanged if the scale of length and time by which it is measured are changed by the same factor λ as the dimensions of the charge. For example, the pressure and duration of the shock wave measured ten feet from a cubical charge one foot on an edge will be the same as the pressure and duration measured twenty feet from a charge two feet on an edge in units of time twice as large”. Therefore, the most common formula given by Cole (1948) is:

$$P_m = K \left(\frac{R}{W^{1/3}} \right)^{-m} \quad (23)$$

where R is the distance from the charge, W is the mass of the charge assumed concentrated at its centre of gravity. Thus, R is the distance between the centre of gravity of the charge and the far away point, K and m are constant that in case of TNT were calculated by Keevin and Hempen (1997), where they are respectively 53.1 and 1.13. The same formula can be used for different kinds of explosives by giving to W the value of the equivalent mass of TNT that would have the same energy, by using the Relative Strength Weight. It must be remarked that Cole made his experiments in deep water, by using spherical charges of TNT, which could be approximated to point explosive charges since the sensors were enough far from the shock wave source. The results in Chapter 7 will show some analysis tools used in

order to prove the validity of the measurements collected according to Chapter 6, as well as to analyse the comparison between the assumption of point charge against the one for cylindrical charge.

3 MALFUNCTION AND SYMPATHETIC DETONATION

3.1 INTRODUCTION

The malfunction of an explosive charge refers to the tendency of explosive material and detonators, to work with reduced strength and/or at the wrong time, or not to work at all. Deflagration, production of toxic fumes, low VOD, and detonation at the wrong delay are phenomena that are associated with what said previously. Because of explosive malfunction, rock fragmentation, as well as general safety and production, are affected. Therefore, the malfunction of an explosive and/or detonator in one borehole (acceptor) caused by the detonation of explosive charges in adjacent boreholes (donor) is still nowadays, a serious concern and one of the biggest problems in the blasting industry. Thus, in the past few years, these phenomena have been studied and yet, they are under extensive study by researchers all over the world. As said, experiments using a variety of explosives have been carried out, for example by using primers and detonators under a variety of conditions, has made possible to understand the occurrence and to quantify the parameters leading to malfunction. With today's knowledge about explosives and their performance, it has been possible to gather the origins of explosive malfunctioning from one or a combination of the following:

- Desensitization of the explosive.
- Changes in the density of the explosive.
- Sympathetic detonation.
- Detonator malfunction, and
- Geometry of the explosive charges.

Before discussing these problems, it would be better to take a look at what is called “Sensitivity” of an explosive material and, furthermore, how is organized what we call “explosive train”.

The explosive Sensibility: is the aptitude that an explosive has to be initiated by a shock or a heat source. It is possible to talk about heat sensibility as well as shock, friction and detonator sensibility.

3.2 EXPLOSIVE CLASSIFICATION

The mining industry is by far the largest industry which requires high consumes of explosive materials compared to a smaller amount used for weapons and shock wave generators for research. Two general types of explosives exist based primarily on shock amplitude required to initiate them, which is called shock sensitivity.

According to the Italian Legislation, explosive material is divided in two different categories:

- Primary explosives
- Secondary explosives

3.2.1 Primary explosives

Primary explosives are very sensitive to stimuli, such as heat, impact, electric current, friction and electromagnetic radiation. Indeed, a relatively small amount of energy is required for their initiation. They are employed in detonators, in very small amount, usually mg, even though a detonator contains also a secondary explosive (this is the first introduction on the explosive train, Figure 23).

Common primary explosives are: lead styphnate, lead azide, tetrazene, tetryl and etc.

3.2.2 Secondary explosives

A secondary explosive is, obviously, less sensitive than a primary explosive, thus, it requires more energy to be initiated. Therefore, it cannot be initiated through a simple heat or shock wave. According to The Bureau of Alcohol Tobacco, Firearms and Explosives (ATF) of USA, the secondary explosives can be classified in two different categories according to their VOD: II^{ndary} High Explosive and Blasting Agents. This distinction clarifies the fact that HEs, unlike the BAs, can be initiated through a No. 8 blasting cap. This means that, a number 8 blasting cap (pyrotechnic Fuse Type Detonator, ‘Detonatore ordinario’, which contains such amount of explosive that has the same relative strength of 2 g of a mixture made of 80% mercury fulminate and 20% potassium chlorate) can initiate a secondary explosive, when it is confined. According to Copper (1997), those materials can be gathered as shown in Figure 20.

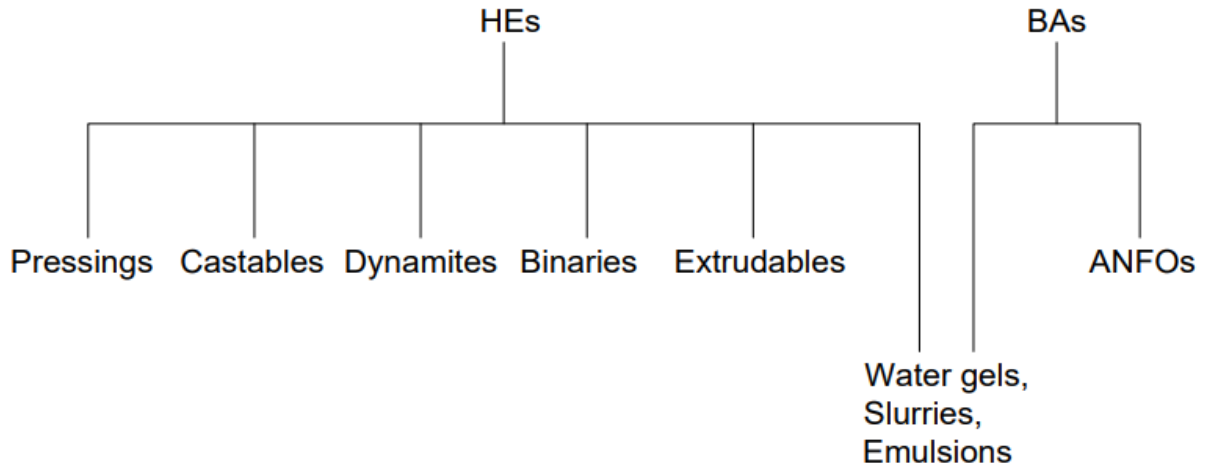


Figure 20-HEs and BAs subcategories.

It can be noticed that Water gels, Slurries and Emulsions stay under both categories, being possible to make them cap sensitive with different techniques, such as by adding TNT or PENT (they lay under Pressing HEs), powders (only for WGs and Ss) or by creating micro-balloons inside the Emulsions.

Figure 21 shows a typical sequence of a main charge which is not cap sensitive, indeed it is needed an explosive train where the detonator is the component (1), a booster is the component (2), namely a secondary sensitive cap explosive and finally the main charge (3), which is a secondary explosive no-cap sensitive.

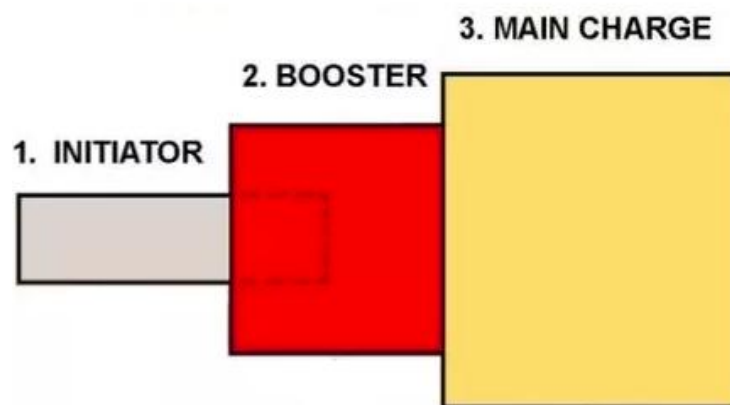


Figure 21- Explosive Train, Initiation Sequence. Source: USA Department of Homeland Security.

3.3 SHOCK SENSITIVITY

“Explosives sensitivity relates to the minimum stimulus for deliberate initiation of a charge as well as the ability of a charge to withstand impact and thus detonate on

time and at full strength after the detonation of neighbouring charges in the case of delayed blasting applications.” Katsabanis (2013).

Shock sensitivity is usually determined by means of gap tests, however, it has been proved that this type of methodology is influenced by the geometry and the confinement of the explosive charge, thereby is difficult to make comparisons between these tests and besides it is even tough estimate, as well as, predict the behaviour of the explosives in practical blasting. For this reason, modelling of shock wave sensitivity is becoming more important day after day.

Waled and Wasley (1969) have linked the shock wave sensitivity throughout the energy fluence criterion. The criterion utilizes the shock amplitude and its duration to claim that the energy per unit area, the energy fluence, is proportional to the square of the pressure amplitude and the duration of the pulse. Equation 24 gives the general formula for an arbitrary pulse:

$$E \propto P(t)^2$$

or

$$E = \int_0^{t_f} P(t)u_p dt \quad (24)$$

or

$$E = \int_0^{t_f} \frac{P(t)^2}{\rho_0 C} dt$$

where E is the energy fluence, P is the pressure, u_p is the particle velocity and t is the time, t_f is the time at the end of the pulse (its overall duration), and C is the sonic wave velocity through the material.

In case of a square pulse, the integral gives us:

$$E = \frac{P^2 t}{\rho_0 U}$$

The energy fluence E is often calculated throughout flyer plate and bullet impact experiments. P.D. Katsabanis (1987) several years ago, carried out different flyer plate experiments for different kind of commercial explosives. Table 1 shows the information used for the critical energy fluence value. The fluence energy in Table 1 was obtained by different past experiment performed by T. R. Gibbs and A. Popolato (1980), which show the “Pop plot” about different kind of explosives.

Through these “Pop plots”, which are obtained from a series of shock-to-detonation transition experiments, it has been possible to calculate E in Table 1.

Table 1- Sensitivity data of explosives used in modelling. C_0 sonic wave velocity, S U-u slope, E fluence energy

Explosive	C_0 [m/s]	S	E [J/cm²]
Detonator sensitive emulsion	1100	1.7	200
Detonator insensitive emulsion	1300	1.6	1140
Detonator sensitive slurry	1700	1.22	112

The code Autodyn (ANSYS, 2010) was used in order to model the impacts and calculate the fluence energy E according to Equation 24.

In Table 2 the results are shown, it is possible to notice that the gaps between the modelling from the “Pop plots” interpretation and the Autodyn code are small, thus they are in reasonable agreement to each other.

Table 2- Summary of results related to high velocity impact.

Explosive	Impact	Impact Velocity [m/s]	Experiment	E [J/cm²]
Detonator sensitive emulsion	-Brass projectile	711	Failed	247
	-Diameter=length=12mm	745	Detonated	275
Detonator insensitive emulsion	-Brass projectile	1300	Failed	996
	-Aluminium flyer plate, 3.2mm thick	1230	Failed	572
	-Aluminium flyer plate, 9.5mm thick	1820	Detonated	1220
Detonator sensitive slurry	- Aluminium projectile	435	Failed	258
	-Diameter=length=50mm	447	Detonated	274

3.4 CHANGES IN THE DENSITY

Density: is for sure one of the most important factors for the choice of a commercial explosive, indeed, density is the key for evaluating an explosive's performance. A slight change in the explosive's density could have a major effect on its detonation properties, sensitivity, and therefore a major role in its performance.

If in any event the density of an explosives product is increased, its specific energy and therefore, its ideal velocity of detonation is increased. However, if the density is increased beyond a critical point, steady state of detonation is not possible. This phenomenon is called "dead packing" and it happens when the volume of the entrained air bubbles or microballoons in the explosives is not sufficient to provide enough hot spots for the reaction to take place.

This can be possible because the density could be altered through different pressures from outside of the borehole, such as the shock wave produced from the detonation of an adjacent borehole (dynamic pressure), changes in sensitivity and performance should be expected. The effect might be permanent or temporary, depending on the level of damage to the bubbles and/or the phase structure of the explosive.

3.5 DESENSITIZATION OF EXPLOSIVES

The desensitization of an explosive charge refers to the loss of detonation sensitivity, said in 3.3.

According to P.W. Cooper (1997), the initiation of a chemical reaction in detonation is similar to what saw in Paragraph 3.3 regarding the flyer plate and bullet impact tests. The shock front compresses the unreacted explosive material, causing local shear failure and inelastic flow (Kamlet and Finger,1979).

Therefore, taking into account a sensitive emulsion explosive, which was used to carry out most of the experiments in boreholes in this paper, the desensitization phenomenon can be due to different mechanisms. It is well known nowadays that, emulsion explosives need "hot spots" (Figure 23) in their mass in order to be initiated and to sustain their own internal reactions. These hot spots, are characterized by high temperature and pressure as well, and they are created by the interaction of the impacting shock wave with density discontinuity, as explained by

Kamlet and Finger (1979). Most common discontinuities in emulsion explosives are glass microballoons whilst, in the case of slurries, air bubbles are preferred.

Although there is a general agreement on the hot spot theory, the precise function of the hot spots is not exactly understood. As a general rule, changes of the density by closing or destroying air bubbles or microballoons or changes in the phases of the explosives (which modifies the nature of the "hot spots" and the intimacy of the mix in the explosive) will result in changes both of density and sensitivity to detonation. In sequential blasting, the desensitization can be caused by dynamic pressure or hydrostatic pressure. The last one is usually only present in very deep boreholes and is not common for this reason. On the other hand, in dynamic desensitization, the most common situation are:

- Shock wave from neighbouring boreholes
- Due to in-hole detonating cord (used as booster for BAs, the shock wave produced by the detonation of the DETCORD could compress the cartridge of the explosive and thus, increases the density)
- Shocks created due to the channel effect in the open space between decoupled explosives and the borehole, this could create a precursor air shock wave, PAS which under some conditions causes detonation failure
- Lateral deformation of the borehole, especially for blasting in weak or highly fissured rocks, could cause a compression of the adjacent charge
- Compression of the charge due to the thrust of intermediate stemming material
- The semi-static pressure field in the borehole ("rifting" or gas pressurization)

The influence of explosive density is a very important factor in blasting, therefore as said in Paragraph 3.4 and 3.5. In Figure 22 it is shown the VOD in function of density for an ANFO. Recalling Equation 4, it is possible to notice the important of the VOD (D) to calculate the pressure detonation P_d , in addition the VOD is a function of density. For instance for the ANFO in Figure 22, iRing company provides the ideal VOD equation: $VOD_{ideal}=4878-3872(\rho-10)$, where ρ is the density (g/cm^3).

Yet, in Figure 22 can be observed a linear increase until about 1.0 g/cm^3 , therefore, once the explosive density is increased, the specific energy is increased as well, this

leads to an increase of the ideal VOD. However, after 1-1.2 g/cm³ (Critical Density), there is a sudden decrease due to the reduction of hot spots, as explained previously.

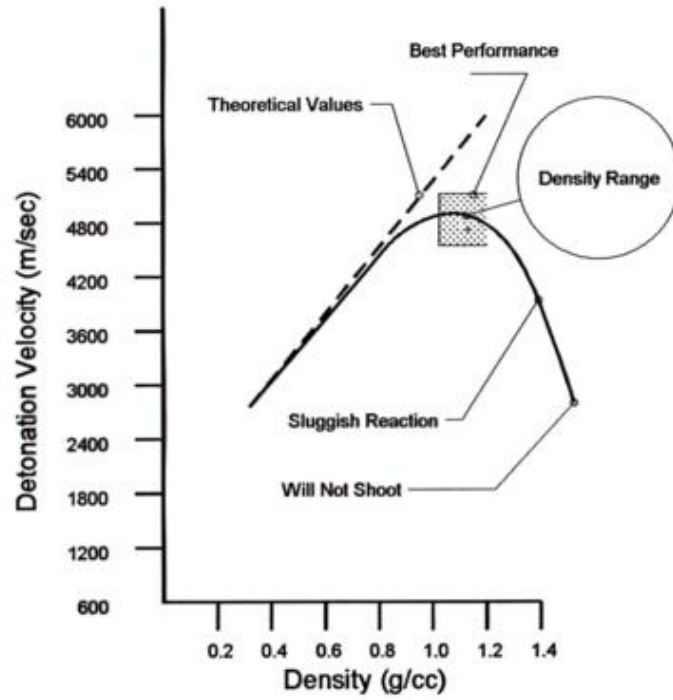


Figure 22- VOD vs Density. Source: www.iring.ca

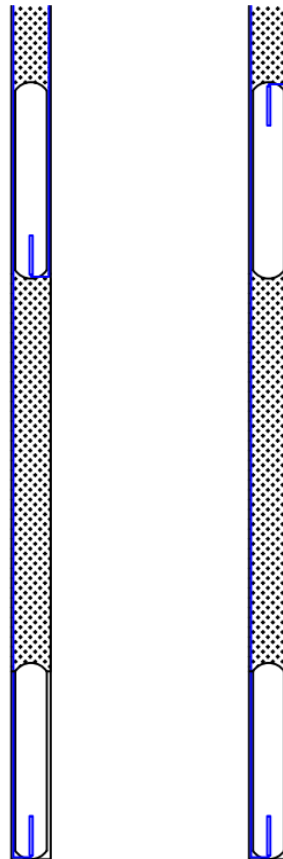


Figure 23- Left, typical configuration, Right, different kind of configuration, less adopted.

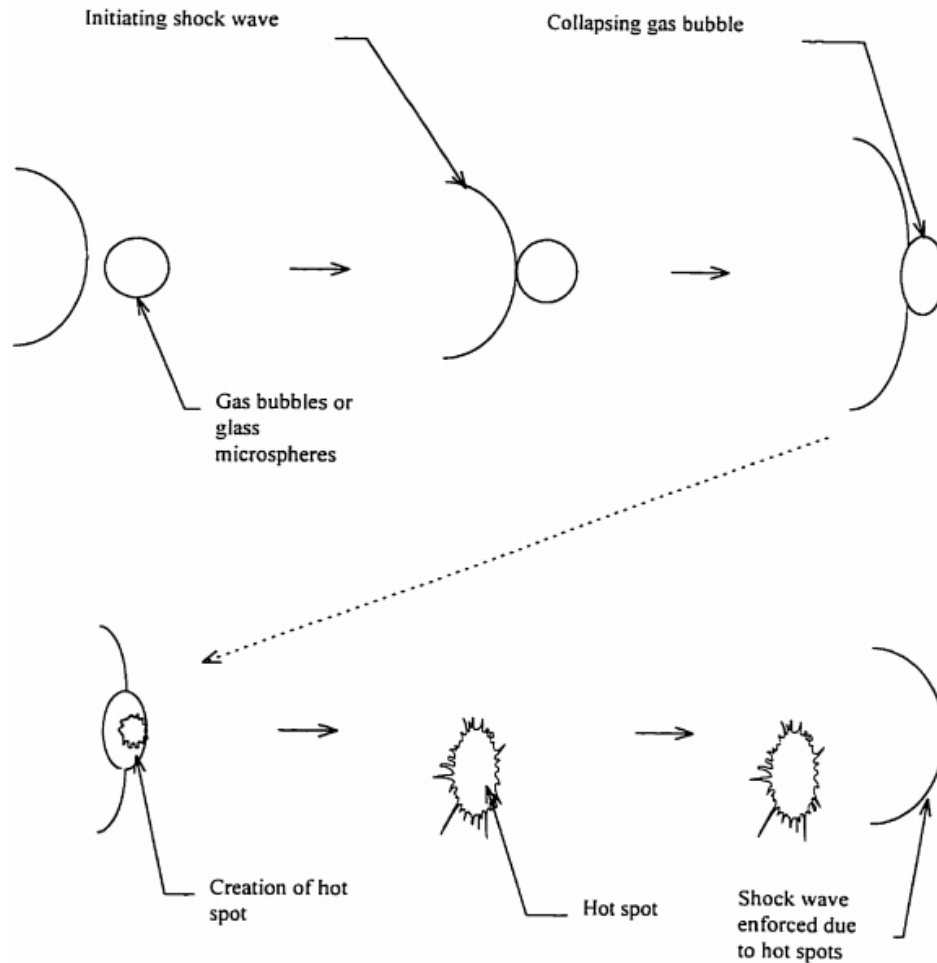


Figure 24- The concept of hot spot, shock wave and air bubble/micro-balloon interaction. Source: Ghorbani (1997)

3.6 ALTERATION OF THE PRODUCED FUMES

The desensitization mechanism of an explosive column has or may have a major effect on the final fumes produced. For instance, taking in to account, the AN (Ammonium Nitrate) based explosives which decompose to produce mainly Nitrogen (N), carbon dioxide (CO₂), and water (H₂O). However, due to shock wave desensitization, the chemical reactions in the explosive may not be brought into completion and toxic fumes such as CO and NO_x (NO, NO₂, and N₂O) could be produced (it is taken for granted the correct stoichiometry of the ANFO). Oxygen deficiency can cause the formation of carbon monoxide and at the same time, excess oxygen can result in the formation of nitrogen oxides. Therefore, oxygen balance of an explosive product can play a major role in the toxicity levels of the fumes produced. The toxicity level within the fume spectrum is also variant.

3.7 SYMPATHETIC DETONATION

According to Zou (2017), “sympathetic detonation is an explosion caused by the transmission of a shock wave through any medium from another explosion. The initiating explosive is called donor explosive, and the initiated one is known as receptor explosive. In the case of a chain detonation, a receptor explosive can become a donor one“. The shock sensitivity is also called “gap sensitivity”; this influences the susceptibility to sympathetic detonations and it could be measured through what is called “gap test”, Figure 25.

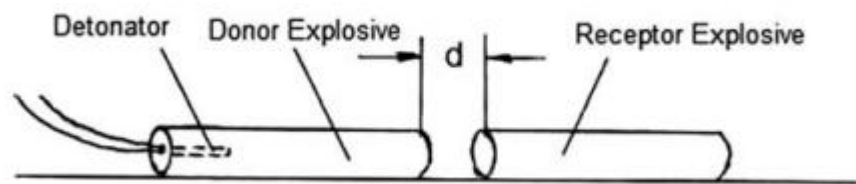


Figure 25- Test of Sympathetic Detonation. Source: Zou (2017)

Sympathetic detonation, obviously affects timing and results in out of delay sequences, in this way the blast could be completely or partially spoiled in terms of fragmentation as well as vibration. There are different parameters that can cause or affect sympathetic detonation in both parallel and decked charges. These parameters include:

- The blasting design (i.e. parallel configuration and decked charges, Figure 26)
- The distance between the donor and the acceptor charges
- Confining material
- Material between the charges (stemming)
- Diameter of the borehole
- The presence and/or the location of boosters and detonators
- The rock structure at the blast site
- The cross-hole reaction gas penetration
- The intensity of the cross-hole stress wave

The orientation of the donor-acceptor configuration is one of the factors that can have a major influence on the way the explosive charges are desensitized and/or malfunction. This phenomena could be amplified in case of drilling deviation, where boreholes can be very close to each other and thus, they can interact.

Furthermore, separation distance, which is the distance among the boreholes showed in Figure 26 up, is very important for malfunctions. Depending on this distance, the effect of the donor charge on the acceptor charge can vary from sympathetic detonation to desensitization and the modification of the timing of delay detonators, shown in Figure 28. This phenomenon is also influenced by the local geology and the rock structure of the area.

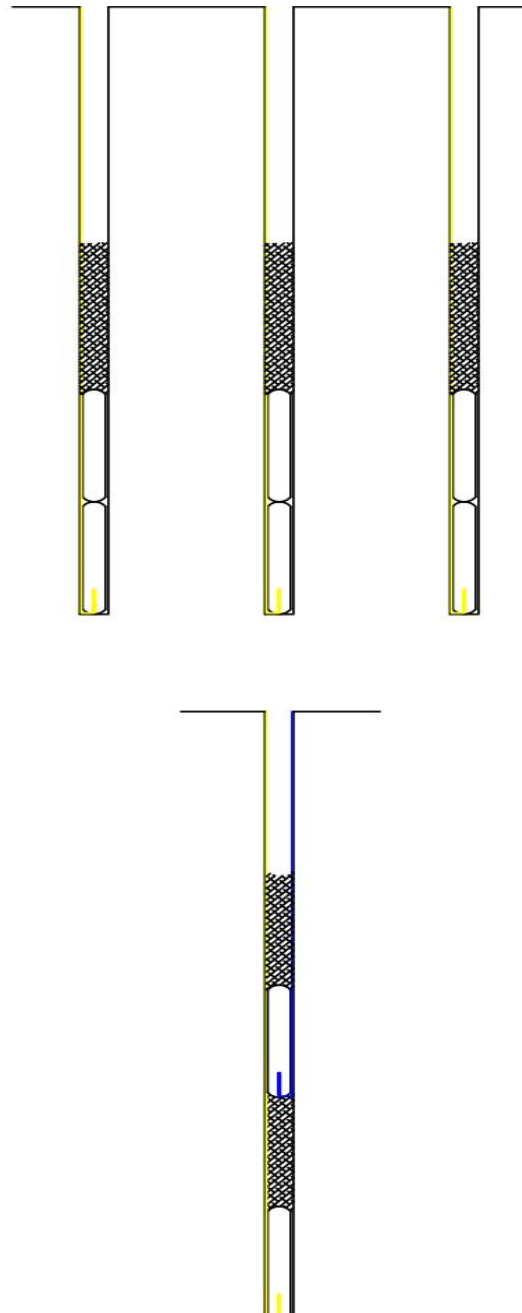


Figure 26- Up: Parallel Pattern Configuration. Down: Decked Charges. Both Contain Sensitized Emulsion Cartridges.

3.8 DETONATOR MALFUNCTION

In Figure 27 are shown two kinds of detonators, NONEL detonator on the left and Electric detonator on the right. During blasting operations, the detonators are placed inside sensitive secondary explosives. Detonators, as explained in Paragraph 3.2.2, are composed by two explosive charges, a primary explosive charge, which is in direct contact with the ignition stimulus (with or without a delay/pyrotechnic element), and a base charge, which is made by a secondary explosive, usually PENT. All these elements are, in turn, placed in a steel shell, which has thickness less than 1 mm. However, this shell in some cases is not able to provide an efficient shield effect against shock waves or fragmented rocks from a nearby detonation of another explosive charge (Figure 29). Thereby, detonator malfunction occurs when the base charge, as well as the delay element, are impacted by a shock, which affects in somehow (i.e. crimping the shell of the detonator) the performance of the detonator itself.

Nevertheless, other effects of shock waves related to internal damage of detonators are still under investigation, especially for electronic detonators, which are used mainly for their time accuracy.

Now, by considering what claimed by the DynoNobel company on their electric detonators: “the detonators withstand, without firing, an impact of a 4.5 to 5 kg weight, dropped from a maximum height of 60 cm, on the most sensitive are of the detonator (base charge)”. The base charge is the most sensitive part since the primary explosive is placed inside another little cage, named inner tube, instead, the base charge is in direct contact with the shell and besides, the amount of secondary explosive is greater.

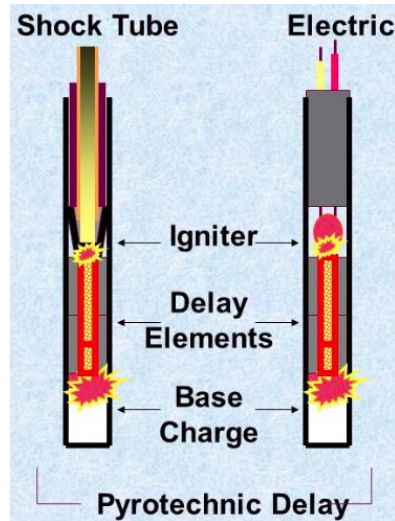


Figure 27- Detonators, Left-NONEL det., Right-Electric det. Source:

Then Iring IN Canadian Company (1996) carried out different experiments; one of them is shown in Figure 28, which basically shows an application on field of the “gap test” in Figure 25. Since there were used different amounts of explosive (sensitized water gel) and different distances among the boreholes, the scaled distance law is used, Equation 25, (it is a factor relating similar blast effects from various size charges of the same explosive at various distances). This law was already seen in Equation 23 for the Cole’s Equation.

$$SD = \frac{d}{W^{\frac{1}{2}}} \quad (25)$$

where SD stand for scaled distance, d is the receptor distance and W is the charge weight.

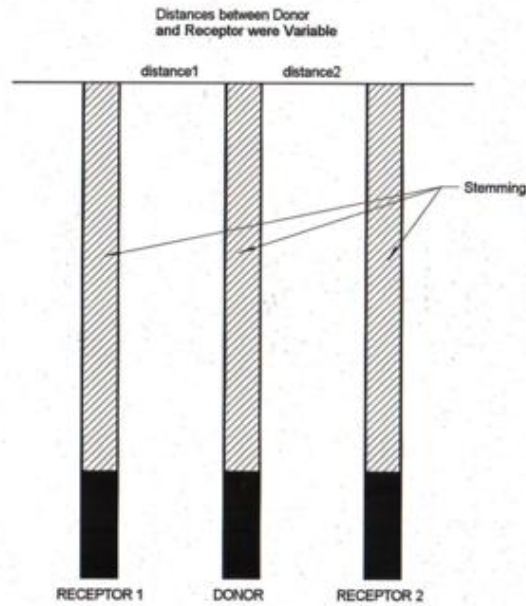


Figure 28- Experiment Donor-Receptors Configuration. Source: www.iring.ca

It was found out that detonators (electric), could malfunction about 50% of the time if the SD value was $0.12 \text{ m/kg}^{1/2}$. Then, detonators would detonate by sympathetic detonation at a value of SD of $0.06 \text{ m/kg}^{1/2}$ 100% of the times.

In Figure 29 is possible to see the effect of a shock wave from the donor borehole that impacted a detonator in a receptor hole.



Figure 29- Damage due to a shock wave from an adjacent charge placed in a side borehole. Source: www.iring.ca

3.9 EFFECT OF PRESSURE ON DESENSITIZATION

The two phenomena of interest in this context are the possible interaction between adjacent blast holes, as well as between two decks in the same hole. This would apply to both explosives and detonators. As said previously, extensive experimental studies have been carried out in the recent past by several researchers. Monhanty & Deshais (1989), Weiland (1990), Sumiya et al. (2001), have shown that one of the major causes of blast malfunction is due to pressure desensitization of the receptor explosive due to shock or explosion gas pressure of the receptor explosive pressure from an adjacent hole. Monhanty & Deshais (1992) performed experiments, in water, where they compared a water gel sensitized in two different ways, namely, by gassing the charge and by adding micro-ballons. Table 3 shows the sympathetic distances in water for a standard 220g Pentolite 50/50 primer and the responds of the different explosives, with and without a detonator. All the detonators in each test were initiated at the same instant; the donor, Pentolite, always with '0' period LP (long period delay) detonator, whereas, the receptor detonators were LP#10, with nominal firing time of 4 s. Besides, these experiments showed that there is a clear difference between a gassed emulsion explosive and micro-ballooned one, in the way these explosives respond to incident shock pressures.

Table 3-Distance for sympathetic detonation in water for a typical pyrotechnic detonator, a gassed slurry, and emulsion explosive with micro-balloons, with a 220g Pentolite primer serving as donor. Wrapped cartridge (50mmx400mm) explosive, with density 1.20 g/cm³

Explosive Product (Receptor)	Sympathetic Distance (cm)	Calculated Incident Shock Pressure (MPa)
LP Detonator (#10)	46	75
Water-gel slurry cartridge (gassed, without detonator)	13	310
Water-gel slurry cartridge (gassed, with same detonator)	200	14
Emulsion cartridge (micro-balloon, without detonator)	6	742
Emulsion cartridge (micro-balloon, with same detonator)	80	40

Besides, the results of Table 3 are the average of at least 5 tests in different configuration.

Yet, Table 3 proves that depending on the type of sensitization used, the incident pressure for sympathetic detonation assumed different values, despite the explosive composition is the same.

Furthermore, other experiments were carried out by Weiland (1990), who found out that water gel explosives are more resistant to shock waves than emulsion at different distances.

Liu and Tidman (1995) instead, performed different experiments in rock, where, they obtained bunch of measurements of pressure in water filled boreholes around a borehole with a detonating explosive.

“The study calculated the pressures in the rock from the pressure measurements in the water on the basis of the impedance mismatch of the media. The pressures compared favourably against pressures calculated on the basis of an equation

developed by Liu and Katsabanis (1993) earlier. The application of the one dimensional impedance mismatch equation, which was used, is however questionable when the geometry is cylindrical and the assumption conditions is also not realistic” Katsabanis (2013), and the equation by Liu and Katsabanis (1993) is expressed as:

$$P = P_m \left(\frac{R}{R_0}\right)^\alpha \quad (22)$$

with

$$P_m = 1.62 \rho_0 D^2 \left(\frac{\rho_r C}{\rho_0 D}\right)^{0.25} \quad (23)$$

and

$$\alpha = -1.35 \left(\frac{C}{D}\right)^{-0.33} \quad (24)$$

where P is the pressure at distance R from the borehole, R_0 is the borehole radius, D is the velocity of detonation in km/s, C is the sound speed in the rock in km/s and ρ_0 and ρ_r , are the densities of the explosive and rock in g/cm³.

Furthermore, several simulations were carried out and those calculations are very close to experimental values. Unfortunately though, this could mislead the reader giving him the idea to take advantage of the value of P , obtained through Equation 22. Hence, combining the pressure obtained in the rock, P , with what saw in Paragraph 2.7, which means going throughout the Hugoniot planes and obtain the final pressure state P_2 , which in this case would be in water. Said this, Katsabanis has proved that this approach is not truthful, even though theoretically it could seem appropriate, because the pressure obtained will be very far from the real value.

3.10 PRESSURE EFFECTS IN DECK BLAST

Mohanty (2009) throughout these experiments, in axisymmetric charge configuration (decking tec.) suggested that a good distance among decked charges would be about 20 diameters (in order to avoid malfunction), however Katsabanis (2013) has shown that, malfunction could be possible either at this distance.

By performing numerical analysis in Autodyn, Katsabanis (2013) has made a comparison between measurements in filled water boreholes shocked by a 10 diameter cartridge of emulsion (density:1.25 g/cm³). As shown in Figure 30, the agreement is quite good, suggesting that the pressure-time histories, predicted by Autodyn can be used in calculating fluence energy as a function of distance.

Katsabanis and Yeung (1993) showed that another factor plays a key role in sympathetic detonation as well as malfunctioning; this factor is the length of the pulse, which is not taken into account from Equation 27, the longer is the pulse, the higher is the energy fluence. For this reason, a qualitative graph is shown in Figure 26.

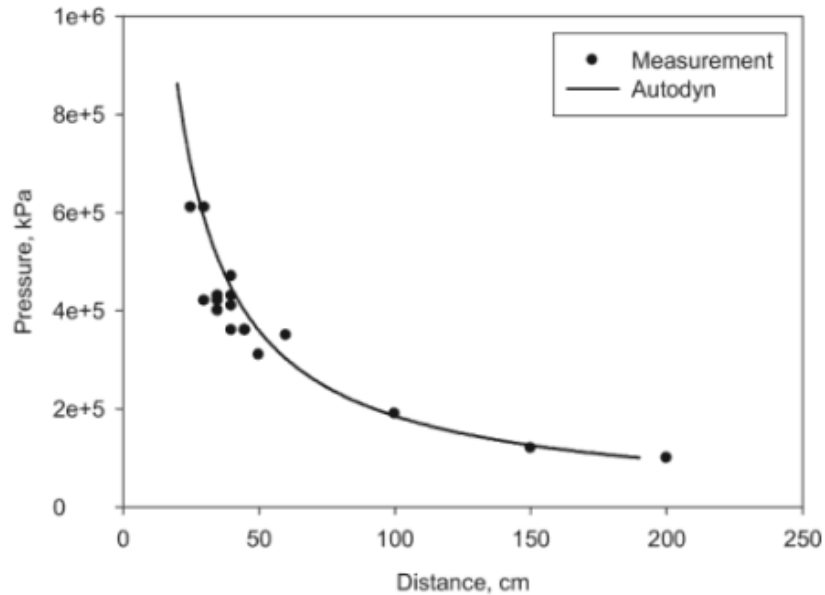


Figure 30- Comparison between measured and calculated pressures away from a charge in a water filled borehole. Source: Katsabanis (2013)

Indeed, critical energy fluence values can explain sensitivity in short pulse duration applications, such as high velocity impacts and interaction between parallel charges. Decked charge applications typically result in relatively long duration pulses and significant specific energy values, which tend to be higher than the critical energy fluence values derived with high amplitude short pulses. It appears that the critical energy fluence is related to the duration of the pressure pulse, and deviates significantly a very long time. In Chapter 6, several experiments performed in boreholes are presented, using different lengths of stemming in order to understand the pressure attenuation through the loose material employed.

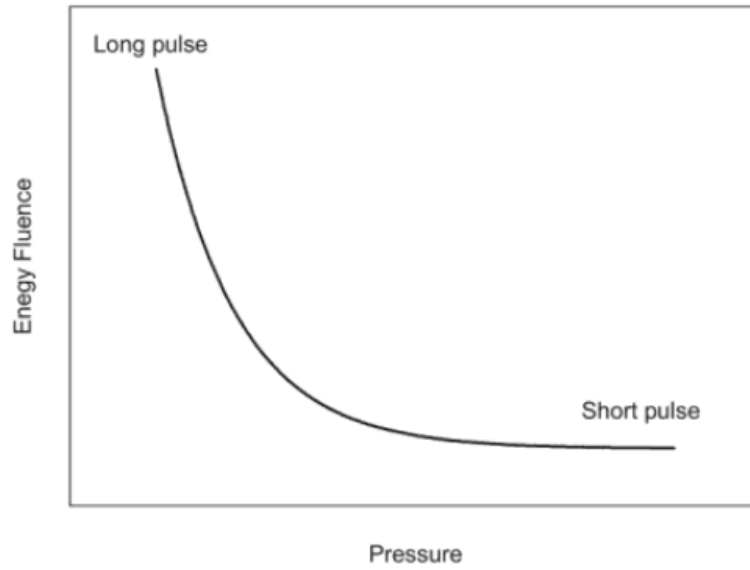


Figure 31- Energy fluence vs. Pressure at Different Durations. Source: Katsabanis (2013)

The relationship between Sympathetic Detonation and Desensibilization could be represented through Figure 32, which has been drawn from applied case by Iring IN Canadian Company (1996), for a sensitive water gel.

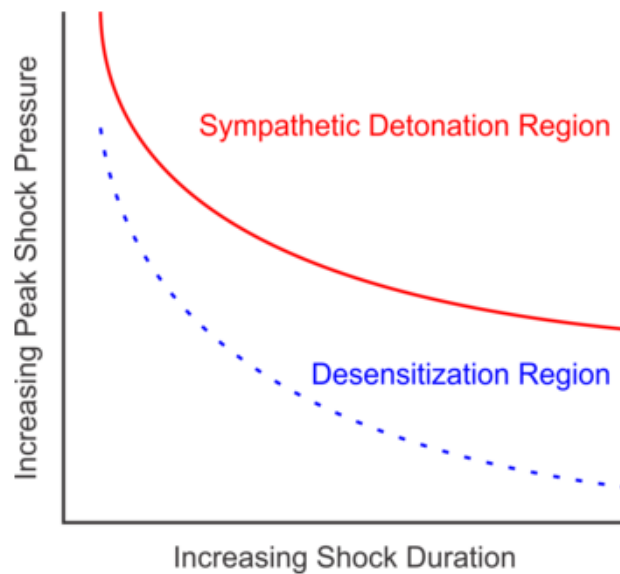


Figure 32-Effect of Shock Pulse Duration vs Peak Pressure. Source: www.iring.ca

4 PRESSURE SENSOR'S LITERATURE REVIEW

Pressure sensors have been used since the second half of the 20th Century, and during all these years, the research of this piece of technology has become more important. This chapter will analyse two different kinds of pressure sensors: on one hand there is the carbon composition resistors manufactured by Allen-Bradley, which nowadays is well known since the past works that different authors carried out; on the other hand, another typology of pressure gauge is worth to be examined, which is based on a completely different effect: instead of giving a response in term of resistance change (as the previous ones), these sensors give an answer in term of voltage, and therefore, they work thanks to the piezoelectric effect. This latter piece of technology is quite new in the field of pressure measurement by detonating explosives, besides for the PVDF gauges, by TE Connectivity, is the first time in the history.

4.1 CCR REVIEW

As said, the use of Carbon Composition Resistors as pressure sensors has started several years ago. They were first used to measure dynamic pressure by Watson (1967), who employed 1/8 Watt resistors and performed a calibration curve where there are two different, quite linear regions, which are linked by a curved segment between 1.5-3 GPa. However, Watson performed experiments only to measure the peak pressure, without considering the time arrivals.

Some years later, Scholz (1981) constructed some transducers with 470 Ohm CCR, which were used as pressure gauges in boreholes during mining operations.

Then, several experiments were performed by Hollenberg (1983), who analysed different kinds of CCR: 47, 470 and 4700 Ohm (nominal values). He achieved different conclusions, as well as different calibration curves: for instance, he found out that 4700 Ohm resistor were not saturated until the stress was over 25 GPa (that is a very high pressure, knowing that the nominal detonation pressure of Pentolite, by Orica, is 25 GPa, Table 4).

Wilson et al. (1987), developed a calibration curve (stress range: up to 4-5 GPa) through the Split-Hopkinson pressure, a drop tower apparatus, and a gas pressure chamber; Weiland (1988) used this CCR as pressure gauges in boreholes, as Scholz

did 7 years before, and he went into detail to the problem of explosives malfunction in underground coal blasts. Throughout these experiments Weiland developed his own calibration curve, suitable for a range of pressure of $0 < P < 0.1$ GPa.

Ginsber and Asay, later (1991), published another calibration curve for a greater range of pressures, compared to the Weiland one, indeed $0 < P < 5$ GPa. They made different experiments, starting from a laboratory approach by means of light-gas gun experiences till reaching a real case by means of detonating explosives in “aquarium tests”, to determine peak stress calibration points. The aquarium test is a method that requires the use of a streak camera and back-lighting photographic techniques.

Katsabanis (1994-1997) used 470 Ohm CCR to analyse detonator and explosive malfunctioning as well as shock wave pressure transmission decking materials. However, he developed a different calibration curve, which is suitable for another range of pressure, $0 < P < 0.3$ GPa. Through the same approach used by Ginsber and Asay (aquarium tests), he developed a calibration curve that is a good compromise considering Ginsber and Asay’s curve and Weiland’s curve. An interesting paper was written by K.S. Vandersall et al (2002) showing CCR gauge’s behaviour to a pressure up to 1 GPa, indeed they developed a new calibration curve using a static gas pressure chamber (Argon environment) and the Hopkison split bar.

4.2 PVDF REVIEW

Nowadays there is not so much to say about this kind of sensors in the field of mining engineering; it is thought, however, that they could really help this research field and perhaps one day even replace the role of the CCR used as low cost pressure gauges.

It is worth to mention their use in Guillermo C.O. Silva’s (2007) patent (Low Density Reactive Agents). In his research, Silva used two typologies of PVDF piezoelectric film sensors (stress range over 40 GPa) provided by Dynasen Inc. and Ktech Corp. Those sensors can work in two different recording modes, namely, charge mode and current mode. For each of these modes, the basic calibration curve was provided by the companies. However, even though these sensors showed good trends, they are not low cost: their price could easily reach hundreds Canadian dollars each, thus new brands, as well as typology of sensors, should be investigated.

5 PRESSURE SENSORS

5.1 INTRODUCTION

Experimental measurement of shock wave pressure by means of pressure gages is not an easy task to accomplish. Explosive discontinuities, temperature effects, shock wave effects (electromagnetic frequency pulses), embedment material of the gage, etc., contribute to ambiguous measurement results. There has been, however, a variety of piezo- resistive and piezo- electric sensors that have been used to measure detonation pressure including manganin gages, carbon gages, tourmaline gages, quartz crystals, lithium niobate crystals, piezo polymeric film gages (PPF) and carbon composition resistors (CCR). Selection of the appropriate gage will depend not only on the pressure range to be measured, but also on cost, which is an important consideration given the destructive nature of the experiments. From the above choices, two fairly different gages were selected: the piezo- resistive carbon composition resistors and the PPF piezo- electric film gages. The former, were provided by the company “Allen Bradley”, which nowadays are out of production, and were used as the principal gage for this investigation, given their low cost, availability and particularly their acceptance as a reliable sensor for harsh non- homogeneous environments. On the other hand, PPF film gages, in particular the FDT series provided by “TE connectivity”, were used in the second place, since their behaviour has never been studied and analysed for shock pressure measurements within a borehole, indeed a calibration curve or useful piece of information regarding their application is not available yet.

5.2 CARBON COMPOSITION RESISTORS

The carbon resistor gauge has previously been studied by numerous researchers in several different resistance values. This gauge is essentially a simple carbon composition resistor that can be used as a pressure gauge with little or no modification.

This resistor consists in a cylindrical element made of a conductive core and its outer is an insulated shell, Figure 34, 35.

The only equipment needed is a power supply to provide a small amount of constant current (signal conditioner).

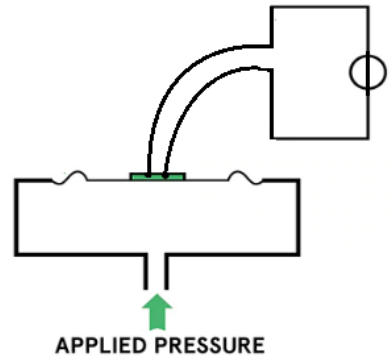


Figure 33- Pressure measurement circuit by means of a signal conditioner (current generator).

Because of the ease of use, ability to measure pressures in the range up to 3-5 GPa, and survivability in harsh environments, it can be used in cases where no other gauge would survive. However, being the gauge manufactured to simply act as a resistor and not as a pressure gauge, an empirical calibration would seem evident. Because of this, the accuracy of this gauge is about 15%. Past experiments at Lawrence Livermore National Laboratory (LLNL, 2001) have incorporated using the 470 Ω carbon resistor gauge in energetic materials that often make measurements in the range of 3-5 GPa and at times in the low-pressure regime less than 0.4 GPa. The resistors used in this work were standard 1/8 Watt, 470 Ω carbon composition resistors made by Allen-Bradley Corporation. The nominal dimensions of the resistor are 1.7 mm diameter and 4 mm long, with wire leads extending from each side of the length of the cylinder, as showed in Figure 34, 35.

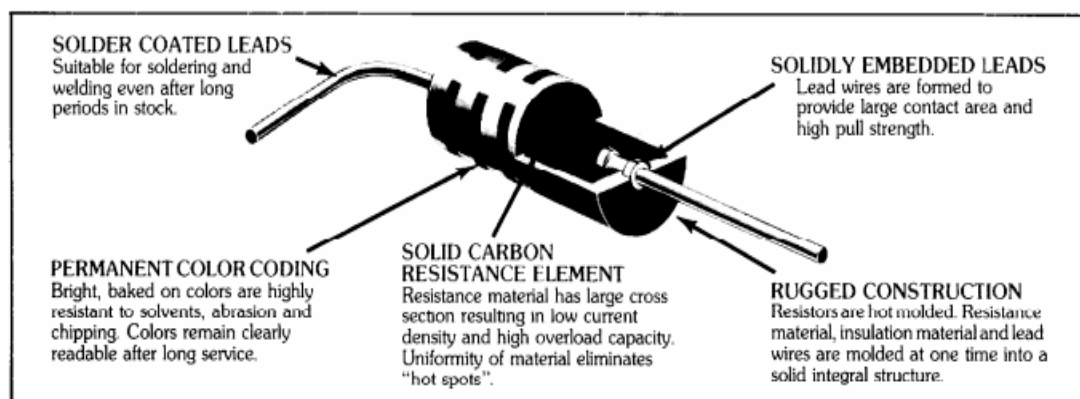


Figure 34- Carbon Resistor by Allen Bradley. Source: A&B Data-Sheet



Figure 35- Carbon Resistor by Allen Bradley.

These resistors/sensors are unfortunately out of production, though, since Queen’s University owns one of the last batch, there was the possibility to obtain and analyse data. This was the main reason to focus attention to the other kind of sensors, even though so far, nobody has collected useful pressure data inside boreholes.

However, it is still possible to find those resistors on the market, though the price has increased to about 20\$ each.

5.2.1 Working principle

The basic principle of the piezoresistive pressure sensor is to use a strain gauge made of a conductive material that changes its electrical resistance when it is stretched. “The resistance value depends on the particle-binder ratio. The higher the amount of carbon particles, the lower the resistance value is. Compression of the resistive element leads to a decrease in resistance because the carbon particles are forced to move closer together and partially touch each other.” Hoerth et al. (2014, AGU)

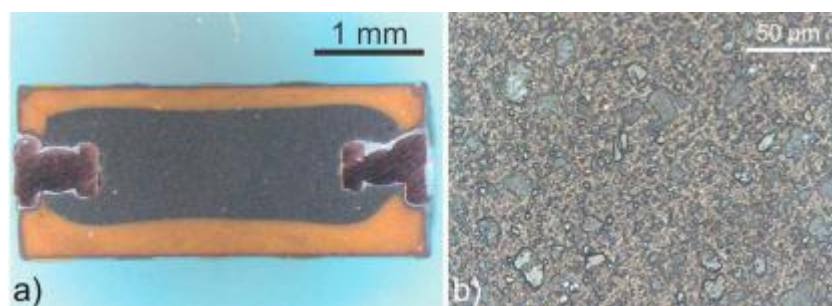


Figure 36- (a) Light microscope image of a cross section through a carbon composition resistor. (b) The conductive core comprises phenolic resin which is enriched with carbon particles to serve as conductive material. Source: Hoerth et al. (2014)

There are three separate effects that contribute to the change in resistance of a conductor:

- The resistance of a conductor is proportional to its length so stretching increases the resistance.
- As the conductor is stretched, its cross-sectional area is reduced, which also increases the resistance.
- The inherent resistivity of some materials increases when it is stretched.

The latter, namely the piezoresistive effect, varies greatly between materials. The sensitivity is specified by the gauge factor, which is defined as:

$$GF = \frac{\frac{\Delta R}{R}}{\varepsilon}$$

where ΔR is the change in strain gauge resistance due to axial strain and lateral strain, R is unstrained resistance of the strain gauge and finally, ε is the strain, namely $\varepsilon = \Delta L/L_0$ (change in length over the original length)

Reminding the first Ohm's law $I = \frac{V}{R}$;

$$V(R) = R(t)I$$

5.2.2 Calibration Equation Selection

Various experimental arrangements have been used by researchers to calibrate the pressure response of carbon composition resistors; these responses being measured in terms of relative resistance and relative conductance (inverse resistance) change. Ginsberg et al (1991) used gas gun and aquarium experiments to produce calibration equations, Hollenberg (1986) used shock wave experiments in water for his calibration experiments while Wieland (1987 and 1993) proposed a calibration constant relating pressure and relative conductance change that was claimed to work well for pressure amplitudes below 1.0 Kbar. What they obtained are the following formulas, namely a relationship between ΔR and pressure P .

Wieland (1993):

$$P(\text{kbar}) = \frac{R_0 - R}{R} \frac{1}{0.2} \quad (25)$$

for $0 < P < 1.0$ kbar

Ginsberg et al (1991):

$$P(\text{GPa}) = 7.001 - 4.345 \left(\frac{R}{R_0}\right) + 0.364 \left(\frac{R_0}{R}\right) - 8.40e^{-\left(\frac{R}{R_0}\right)} \quad (26)$$

for $0 < P < 50 \text{ kbar}$

In the above equations, R_0 and R refer to the original and the instantaneous resistances respectively, expressed in Ohms.

However, for this work advantage is taken from the Katsabanis' formula (1997), which is a good compromise, speaking in terms of pressure, since it has a restricted range of pressure, namely for $0 < P < 3 \text{ kbar}$.

$$P(\text{MPa}) = 4848.08 \left(\left(\frac{R_0 - R}{R_0} \right)^2 + 94.15 \left(\frac{R_0 - R}{R_0} \right)^{0.5} \right) \quad (27)$$

Equation 26 is the result of several aquarium experiments performed by Katsabanis (1997), in which the shock wave was generated by an explosive donor and it travelled through a plexiglass plate, 12 mm of thickness, until reaching the water media. The velocity of the shock wave was continuously recorded via a streak camera, Figure 37.

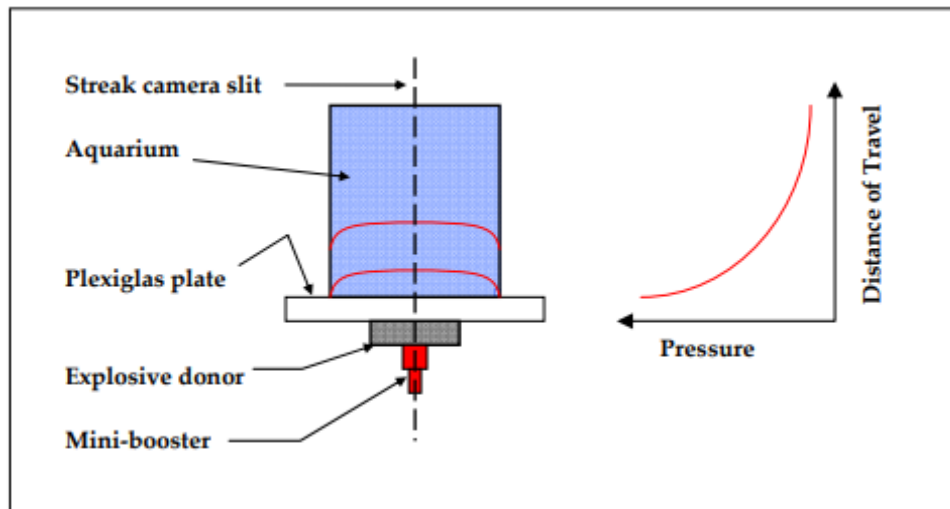


Figure 37- Aquarium Experiments performed by Katsabanis (1997). Source: Gullermo C.O, Silva (2007)

By gathering the three difference calibration curves in the same graph, Figure 38, it is possible to notice that the pressure P in function of the rate R/R_0 behaves in two different ways: exponential decrease plus a linear decrease. In the high pressure branch, the exponential one, where the Ginsberg et al (1991) formula was developed, a little variation of R/R_0 means a huge pressure range on the pressure axis (y-axis), thereby this leads to a great error for the evaluation of this range of pressure. On the other hand, the pressure assumes a linear behaviour and in this branch the Wieland's formula was developed. However between those two, it has to be considered the Katsabanis' formula, as said earlier.

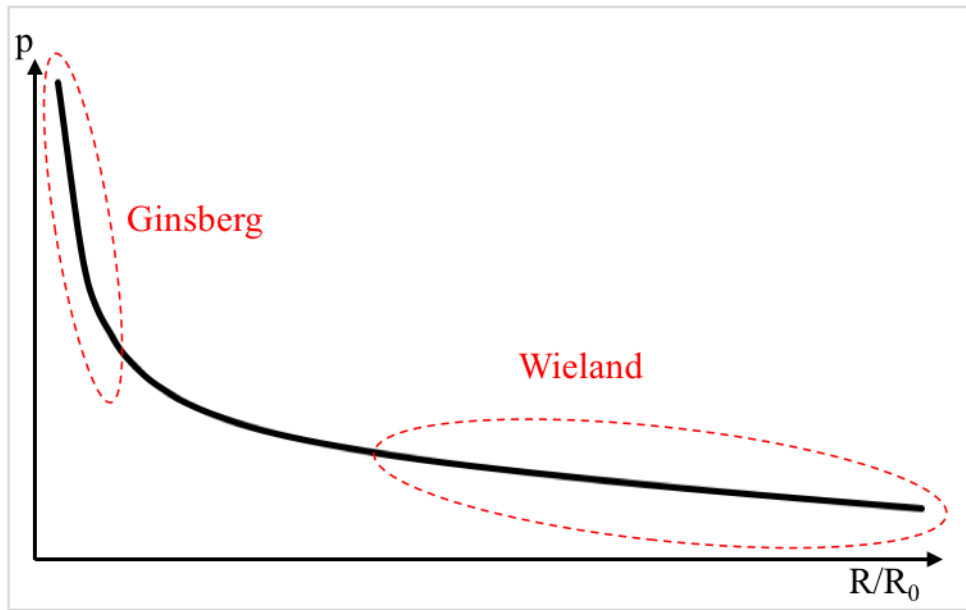


Figure 38- Pressure vs R/R_0

In the end, an answer in terms of voltage, was collected from the sensor, as noticeable in Figure 39, 40.

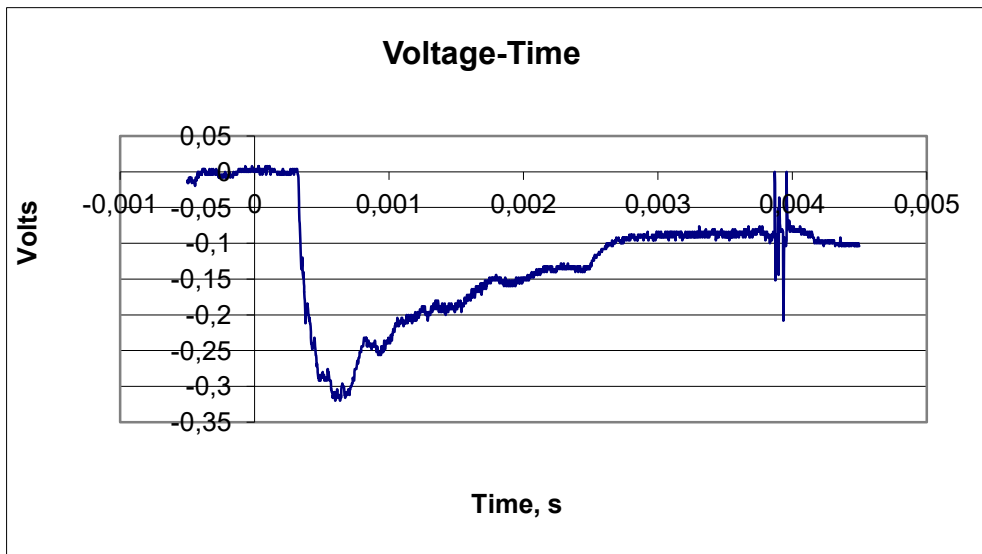


Figure 39- Voltage Drop Due To Shock Wave, Bucket Experiments

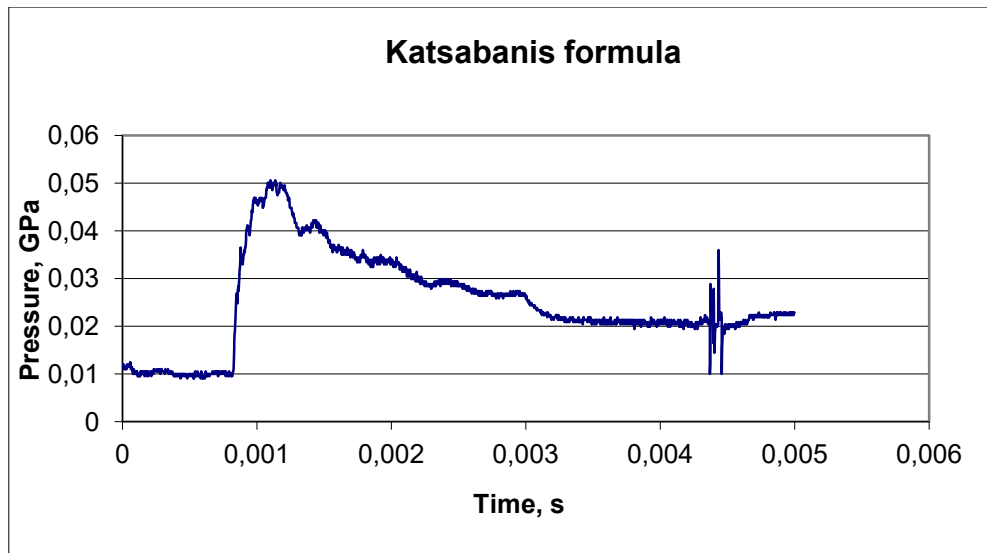


Figure 40-Pressure Curve Obtained From Figure 38

5.3 PIEZO POLYMERIC FILM GAUGES

Transducer materials convert one form of energy into another, and are widely used in detecting applications. The tremendous growth in the use of microprocessors has propelled the demand for sensors in diverse applications. Today, piezoelectric polymer sensors are among the fastest growing of the technologies within the \$18 billion worldwide sensor market. Like any new technology, there have been an extraordinary number of applications where "piezo film" has been considered for the sensor solution. This paragraph focuses only on one of thousands applications, which that is as pressure sensor.

Piezoelectric materials undergo a dipole deformation and electric charges accumulation as response to a mechanical stress. An electric field will generate and thus, voltage can be detected on the upper and lower surface of the piezoelectric materials. When stress is removed, the voltage disappears. This phenomenon is called direct piezoelectric effect.

The sensor by TE connectivity, showed in Figure 41, is flexible, lightweight, produced in a variety of different sizes, thicknesses and shapes. Its properties as a transducer include:

- Wide frequency range—0.001 Hz to 109 Hz.
- Vast dynamic range (10^{-8} to 10^6 psi or μ torr to Mbar).
- Low acoustic impedance—close match to water, human tissue and adhesive systems.

- High elastic compliance.
- High voltage output (10mV-100V).
- High dielectric strength—withstanding strong fields (75V/ μm).
- High mechanical strength and impact resistance (10^9 - 10^{10} Pascal).
- High stability—resisting moisture.



Figure 41-FDT series

However, the major disadvantage of piezoelectric pressure sensors is that they can only measure dynamic or changing events. It is because a static pressure will result in a fixed amount of charges on the piezoelectric material, causing an initial voltage output.

As specified before a particular kind of sensors produced by “TE connectivity” was used and, being the price for each sensor about 4 they became very suitable for the research.

In addition, since any information was found about their composition, either in the DataSheet, the company was directly contacted. That is what Richard Brown, Application Manager at TE connectivity, Sensors’, claims about the sensors:

“Our FDT series of piezo film elements are constructed using PVDF (polyvinylidene fluoride) polymer which we process in-house to make it piezoelectric. This polymer film is then printed on each surface with conductive (silver) ink patterns to provide an electrode structure. Finally, the electrodes are coated with a very thin clear acrylic coating to prevent the formation of Ag_2S (tarnish).”

5.3.1 Working principle

Piezoelectricity arises from the cross-coupling of mechanical and electrical energy within certain materials; these materials can be used as both actuators and sensors. When a piezoelectric device is used as sensors, it actively generates charges in response to external loads, if compared to piezoresistive sensors where a voltage/current source is applied across the sensor to measure the strain.

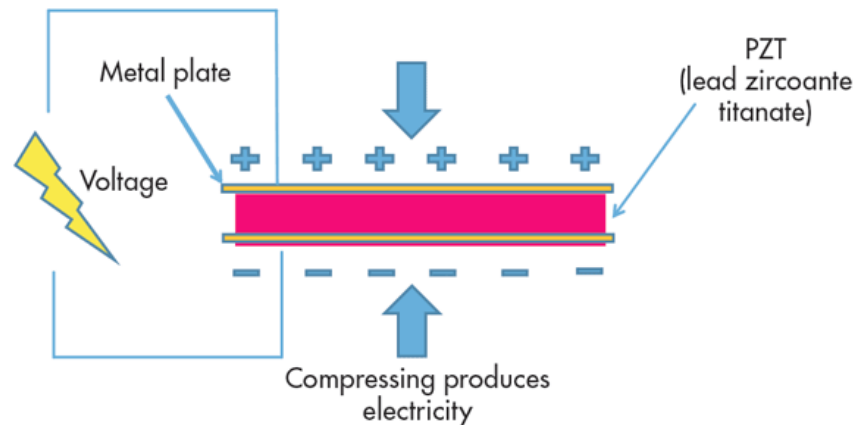


Figure 42- Piezoelectric effect sketch considering PZT as piezoelectric material. Source: <https://www.liberaldictionary.com/piezoelectric/>

Figure 25 shows a piezoelectric crystal (PZT), which is placed between two metal plates; however, in the sensors employed, the piezoelectric material is PVDF, polyvinylidene fluoride.

At this point, the material is in perfect balance and does not conduct an electric current.

Mechanical pressure is then applied to the material by the metal plates, which forces the electric charges within the crystal out of balance. Excess negative and positive charges appear on opposite sides of the crystal face.

The metal plate collects the charges, which can be used to produce a voltage signal, that will be treated and analysed throughout different pieces of equipment.

5.3.2 Calibration Equation

An attempt of calibration curve was performed. First of all, some small scale tests were carried out in order to understand the behavioural response of the PVDFs. Therefore, two PVDFs were placed in between of two pieces of Plexiglas (1.1cm of thickness) which were glued to each other to ensure continuity. Then, a little Hopkison Split Bar was built, Figure 43.

A projectile of steel was shot against that sandwich-gauge through an air gun (in blue in Figure 43) from a distance of 15 cm with a pressure in the gun of 9.3 bar. The sandwich was kept standing by means of a vice and in every shot the time of arrival of the shock wave between the two signals (produced by the projectile against the two sensors) was always $4.4\mu\text{s}$; this means that the gauges work with good accuracy and that the measurements are repetitive.

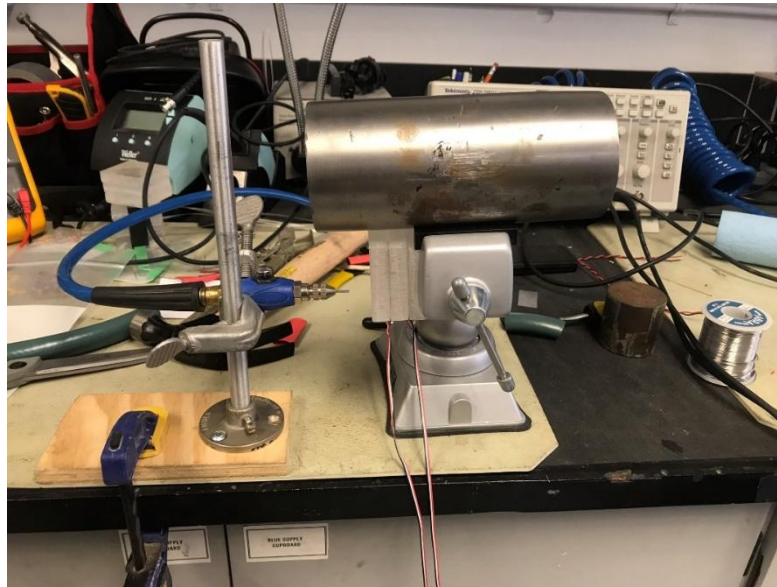


Figure 43- Hopkinson Split Bar in Little Scale

After small scale tests, some experiments were carried out throughout the Hopkinson Split Bar, which is a good substitute of shock waves by detonating explosive. These kinds of experiments were not destructive and a PVDF gauge was placed in between of two steel disks, Figure 44, 45. The goal of these tests was to observe the response, in term of voltage, of the PVDF due to a strong shock stimulus. However, problems occurred during these tests and it was impossible to obtain a clear development of the trials.



Figure 44- Hopkinson Split Bar



Figure 45- Hopkinson Split Bar

6 FIELD EXPERIMENTS

6.1 INTRODUCTION

"The experiment serves two purposes, often independent one from the other: it allows the observation of new facts, hitherto either unsuspected, or not yet well defined; and it determines whether a working hypothesis fits the world of observable facts." Rene J. Dubos (1953).

In this chapter, the methodology employed, as well as pieces of equipment and besides are analysed, including different methodologies of acquiring data. Experiments were carried out according to different methodologies as well as equipment; however, measurements were improved, in almost each experiment, through the change of the sensor design and recording data; this is the reason why different paragraphs discuss the same kind of sensors, though conceived with a different construction method and different instrumentation.

Besides, all the borehole tests were carried out in granodiorite bedrock, with the following properties:

Mohr-Coulomb Linear Regression Parameters $\sigma_c=174.4$ MPa, $c=30.4$ MPa, $\Phi=51.6^\circ$

6.2 CCR GAUGES

As reported in paragraph 5.2, carbon composition resistor are just resistors that change their resistance according to the stress they are exposed to. The design of these sensors was about the same for all the versions: the resistor was connected to a coaxial cable, which is shown in Figure 46. However, as written in 6.1, different methodologies were employed, therefore in Figure 47 the other cable used in the third typology of sensors is shown. Thus, there are two main cables, the centre conductor and the braid; they will be connected to a Signal Conditioner on one side and, on the other side, they will be linked to the resistor as positive and negative pin.

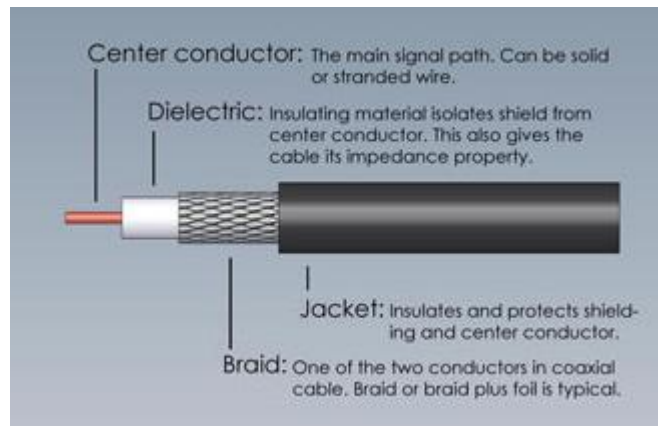


Figure 46- Generic coaxial cable cutaway view

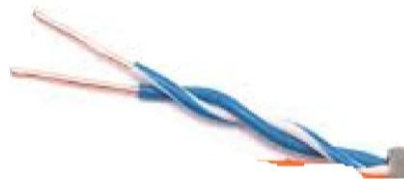


Figure 47- Twisted cables

The resistor is well known and its function is well explained in 5.2.1, three different sensors were designed, where, the first two are pretty similar, whereas the last one is completely different and responded better to the tests.

6.2.1 CCR, first typology

The first experiments were done throughout this typology of CCR: the resistor is connected to the centre conductor by means of a “copper tube” which has been squeezed and well coupled using simply a plier, then, in order to insulate the first pit, a rubber tube was shrunk (Figure 48)



Figure 48- First step, CCR, first typology

Then, it was connected the other pin to the braid cable, which was twisted shown in Figure 47. In this first case, the two were soldered with some tin and then another

piece of rubber tube was placed and shrank as well. At the end of these two steps, the “raw sensors” was obtained, as shown in Figure 49.



Figure 49- Second step, CCR, first typology

Before sealing the whole sensor into a pipette full of mineral oil, the resistance has to be checked, since heated up (to shrink the rubber tubes). In this way the resistor itself was influenced and a change of a bunch of Ohms, about 1-15 Ω was obtained, both because of heating them up and soldering them. These were the main reasons why it was decided to change a bit the design in the other experiments.

As anticipated, the sensors were then placed inside a dropper (pipette) full of mineral oil. This provides different advantages, such as the possibility to have a sterile environment for the resistor as well as physical protection, and least but not last, a shield against Electro Magnetic Fields. The latter was a big problem in the past experiments, since the analysis of the data has been made impossible due to EMF (mainly due to the recording equipment though), which produced too much noise and thus, it was not possible to extrapolate suitable data.



Figure 50- Finished sensors, first typology

In Figure 50 the finished sensors before their use on site are shown. As noticeable, the pipettes are tied up with some plastic ties and besides, the sensor has been placed inside them trying to avoid, as much as possible, formation of air bubbles, which could affect considerably the pressure measurement. Furthermore, the avoiding of air bubble was one of the main challenge in this design; first because some air remained inside the rubber shrink, since it was not too adherent to the resistance whereas it was necessary to keep the temperature (by means of a heat-gun) as low as possible in order not to affect the resistance itself. Second, because the pipette could not be shrunk since the mineral oil could have caught fire.

6.2.2 CCR, second typology

Basically the construction process was almost the same; however, as specified in paragraph 6.3.1, the change of resistance value could have been avoided without using both the solder and the last shrink (the one that completely covers the sensor, which decreases the probability of making air bubbles). Therefore, after the first step shown in Figure 48, the sensor's pin were twisted together with the coaxial cable by using a simple pliers, and finally, the resistance was placed and sealed inside the pipette full of mineral oil.



Figure 51- Finished sensors, second typology, not sealed yet (always through using plastic ties)

As it can be seen in Figure 51, the resistance is in contact with the mineral oil. The main differences between these two kinds of sensors can be observed in Figures 50-51.

The first and second type have been used for different experiments, but unfortunately they were not so suitable for boreholes (the signal was plenty of noisy) and, for this reason, they were used to analyse the shock wave behaviour in water, by: buckets, garbage bins and pipes.

6.2.3 CCR, third type

The third typology of CCR was used for most of the experiments, due to their good response to the pressure pulse. They were used in both buckets and boreholes, as well as in both the environments, and clear pressure curves were obtained.

About the construction method, it was quite different since in this kind of sensors there is not any pipette and mineral oil.



Figure 52- CCR, third typology, before being insulated

The main difference, as is possible to notice in the first place, is the cable to which the sensors is connected (the yellow one), that is much thinner compared to the

coaxial one visible in Figures 50-51. This feature will allow to get a clearer signal with less noise and furthermore, less interferences and loses of the shock wave pulse travelling through it. Then the resistor is connected to the cables through two pieces of copper tube well pushed together, and finally, one of the pin was shrank by means of a heat-gun, taking care of the resistor that has not to be warmed too much. Finally, the resistor (showed in Figure 53) was dipped into a naphtha rubber solvent for making it insulated. This rubber solvent has a good tensile strength, as well as great dielectric strength proprieties, so that it avoided the problem of air bubbles attached to the sensor.

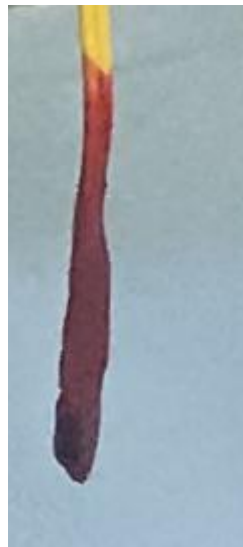


Figure 53- Finished sensor, third typology, insulated with a special coating.

6.3 CCR EXPERIMENTAL SETUP AND PROCEDURES

The tests took place at the site described in paragraph 5.2. Different kind of experiments were done in order to understand, as much as possible, the limits as well as the main features of this technology. What it was observed was remarkable, even though it took a bit more than expected, since some problems were encountered with the instrumentations, which will be explained later on.

First of all the first tests are introduced, dated 20/09/2019, up to the last one, which was performed on 11/10/2019.

6.3.1 First tests, setup 13/09/2019

As shown in Figure 54, the pieces of equipment used were mainly two: the signal conditioner, which in the first place allowing to supply the sensors with a current of

4 mA (in this case) and providing the output signal. The other tool in the picture is the “MicroTrap”.



Figure 54- First test's setup, starting from the left side, rightwards: Signal conditioner, Microtrap, Multimeter, Chargers.

Basically, this instrument allows to bring just one little box to the site instead of different oscilloscopes, since usually they have 2 channels each (nevertheless, it is possible to purchase oscilloscopes with 4 channels and more, even though being more expensive) and furthermore, the MicroTrap has been designed for acquiring data either in extreme situations. In Figure 56 is shown the voltage drop signal acquired through the MicroTrap. However, after investigation of this equipment, it has been decided that all the data obtained by the MicroTrap will be not considered in this analysis, since mismatches were found during the analysis. Due to this mismatch, it was decided to gather data only by means of oscilloscopes.

Anyways, in Figure 56 is shown a signal captured throughout the DataTrap, on Channel 1, due to an explosion of a booster of Pentolite 50/50, and in Figure 55 the respective values of pressures.

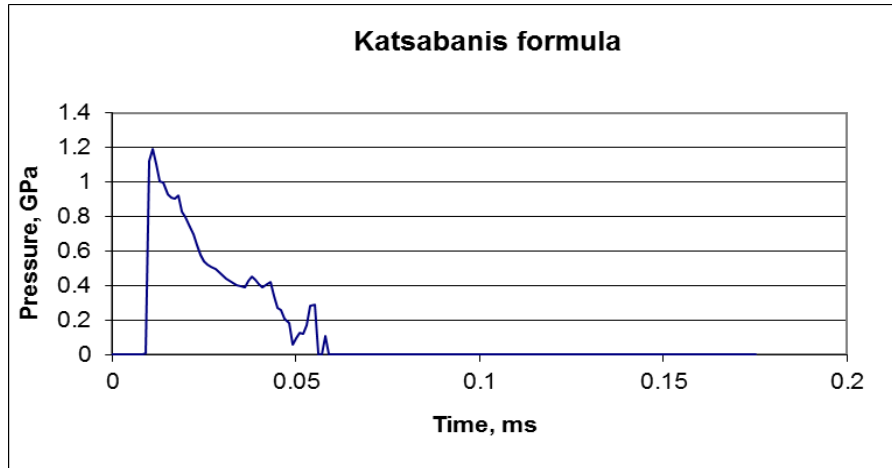


Figure 55- Pressure curve. TEST 1, 30mm faraway from the booster

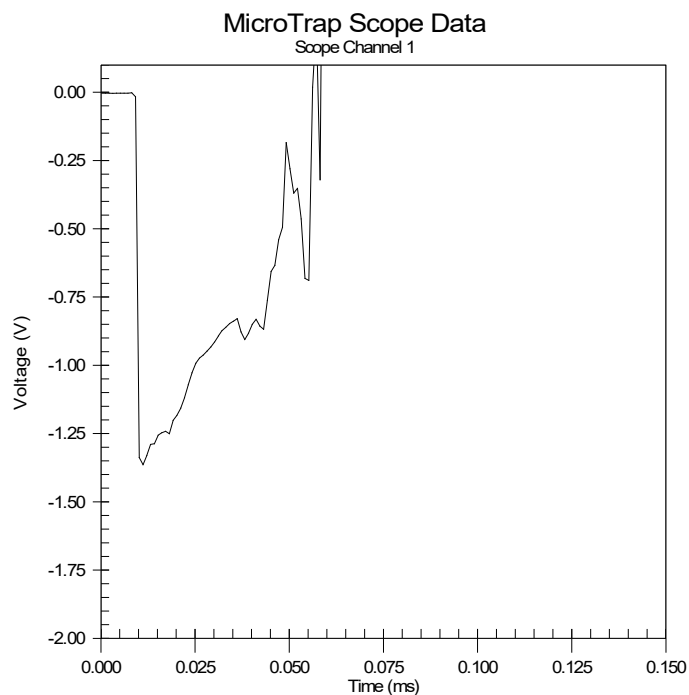


Figure 56- Voltage drop, TEST 1, 30mm faraway from the booster, Volts-micro seconds

6.3.1.1 Experiment descriptions

First of all the different part of the experiment will be described, as noticeable in Figure 57-58. Two wires passing through the primer charge are visible: the yellow one is the NONEL shock tube, whereas the twisted one is the trigger line which is useful to trigger the DataTrap, to have synchronized measurements among all the sensors.

A booster of Pentolite 50/50 TNT/PETN (Table 4, by Orica) was used.

Table 4-Pentolite Technical Data, by Orica

Nominal Diameter	60 mm
Nominal Length	120 mm
Nominal Mass	454 g (1 lb)
Shell Material	Open Top Cardboard Canister
Shell Colour	Fluorescent Orange
Nominal Density	1.6 g/cm ³
Nominal Detonation Pressure	25 GPa

The ignition system was a sort of mix between electric and Nonel. Attention was paid in placing the electric detonator, since it could produce EMF and thus, noise during the experiment; for this reason, the electric detonator was placed as far as possible from the sensors and buried, in order to confine as much as possible its explosion.

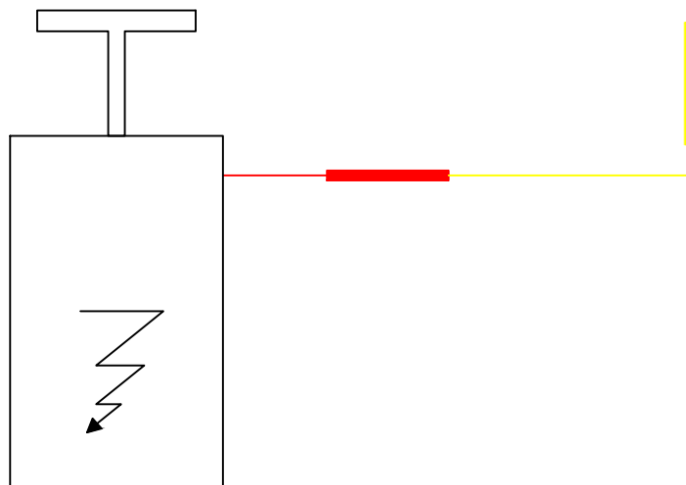


Figure 57- Ignition System, Blasting Machine plus Electric and NONEL detonator.

Figure 57 provides a sketch of the ignition system; the Blasting Machine (on the left), is a capacitor equipped with a battery that releases a current to initiate the electric detonator (red). The electric detonator initiates the NONEL detonator (yellow) that initiates the charge.

Figure 58 shows two cables twisted to each other and placed inside the charge. Those cables work as “Trigger line” for the Microtrap/DataTrap (which is essentially a faster Microtrap). Therefore, when the detonation start, those cables will melt together and thus, the DataTrap will start recording data.

Finally, the sensors (first type) are “hanged” (fixed) by means of plastic ties and besides, they are bonded to a piece of wood.

The bucket has dimensions: 44.3 cm height, 30cm top diameter, 26cm bottom diameter, and it was filled up to about 34cm, as shown in Figure 59.

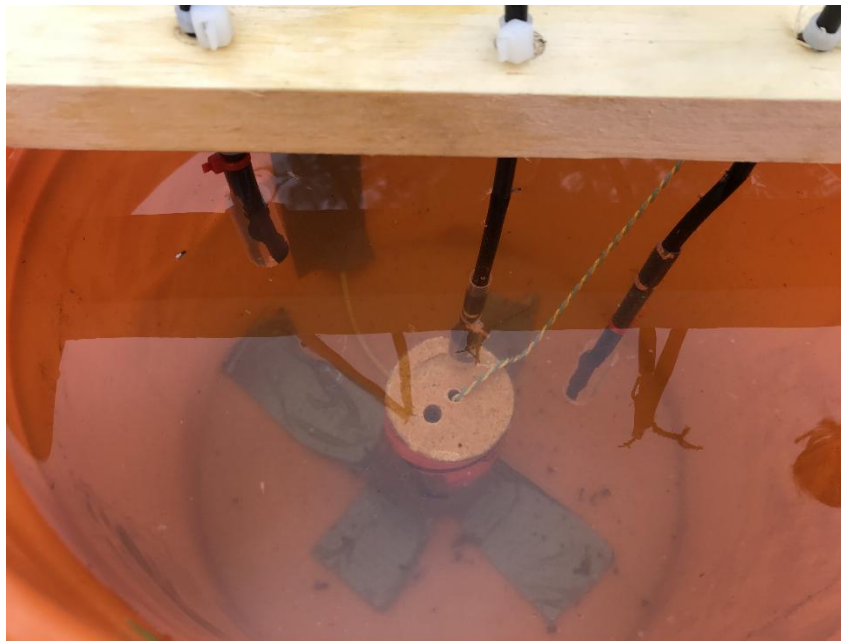


Figure 58- Experiment 1, Primer on the bottom of the bucket, sensors hanged at difference heights

In Figure 59 is shown the CAD lateral view of a bucket experiment.

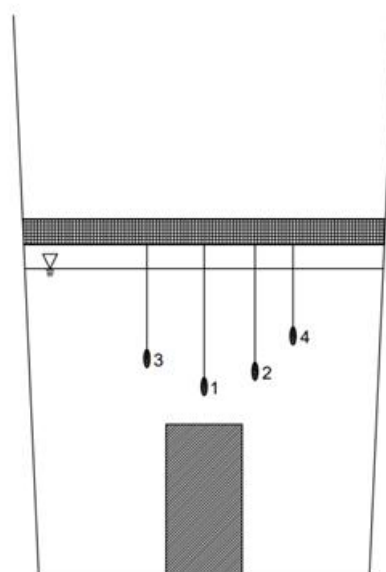


Figure 59- Lateral view, Orthogonal Projection, First set up

6.3.2 Second tests, setup 27/10/2019

Different tests were conducted using the same buckets described in 6.4.1.1, as well as a big garbage bin. The explosive employed was the same used in the previous tests, Table 4. This time though, different pieces of recording equipment were used, as indeed anticipated in the last paragraph; two Tektronix TDS1001B oscilloscopes (two channels each) and one Yokogawa DL750 scope (four channels) were used. Tables 5 and 6 summarize the main features of the equipment shown in Figure 60.

Table 5- Tektronix TDS1001B Main Features

Frequency	40, 60, 100 MHz
Sample Rates	Up to 1 GS/s real time
Channels	2

Table 6-Yokogawa DL750 oscilloscope, main features

Sample Rates	Recording Time	Channels
10 MS/s	100 s	4
1 1 MS/s	600 s	
100 KS/s	9000 s	
10 KS/s	72000 s	
1 KS/s	864000 s	
200 S/s	2592000 s	



Figure 60- Tektronix TDS1001B (left), Yokogawa DL750 (right)

Thus, eight channels were completely available, which means eight sensors. Then another S.C was added, in order to provide power to the other four sensors. The S.C. current was increased to 10 mA of current, in order to obtain a clearer signal.

6.3.2.1 Experiment Description, Buckets

Basically, all the experiments in date 27/09/19 were carried out throughout the second type of CCR. However, the last bucket test was performed using the third type of CCR, where indeed, a better trend in the curves Voltage-Time, Pressure-time was noticed, and besides, the fabrication process was much faster compared to the previous one, since not mineral oil and neither pipettes were employed, and just those kind of sensors were used.

Three different experiments were performed in buckets, including the one with the third typology.

The first experiment was basically the same shown in Figure 58, 59: same charge, same detonation system, though the sensors had different distances from the primer; the results are discussed in Chapter 7.

Furthermore, the major breakthrough in CCR was achieved in the following experiment, since a new design of piezo-resistive sensors was developed, by improving the construction process, installation comfortability and besides, a cleaner output signal was obtained.



Figure 61- CCR third type during field experiments

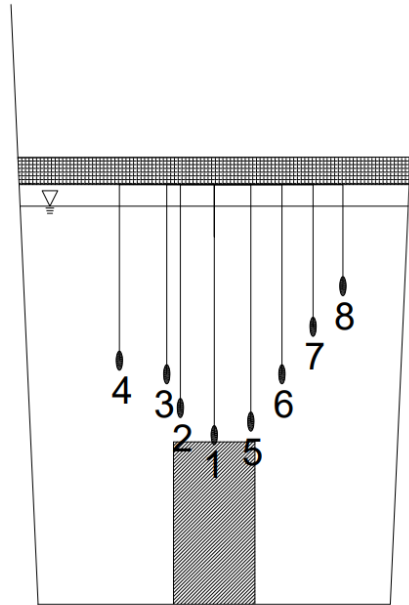


Figure 62- Lateral view, Orthogonal Projection, Third type of CCR, first try

6.3.2.2 Experiment Description, Big Bucket

The third experiment was completely different, since the “environment” was changed by using a different control volume. A big bucket was employed, with a volume of 166 litres, 81x61 cm (HxD). The goal was to examine how the shock wave travelled and behaved in a bigger environment, with greater distances and in further positions, as shown in Figure 64, especially looking at sensors 5, 6. The pressure curves are attached in Appendix II, while the results are presented in Chapter 7.



Figure 63- Picture taken on field, putting in place the sensors

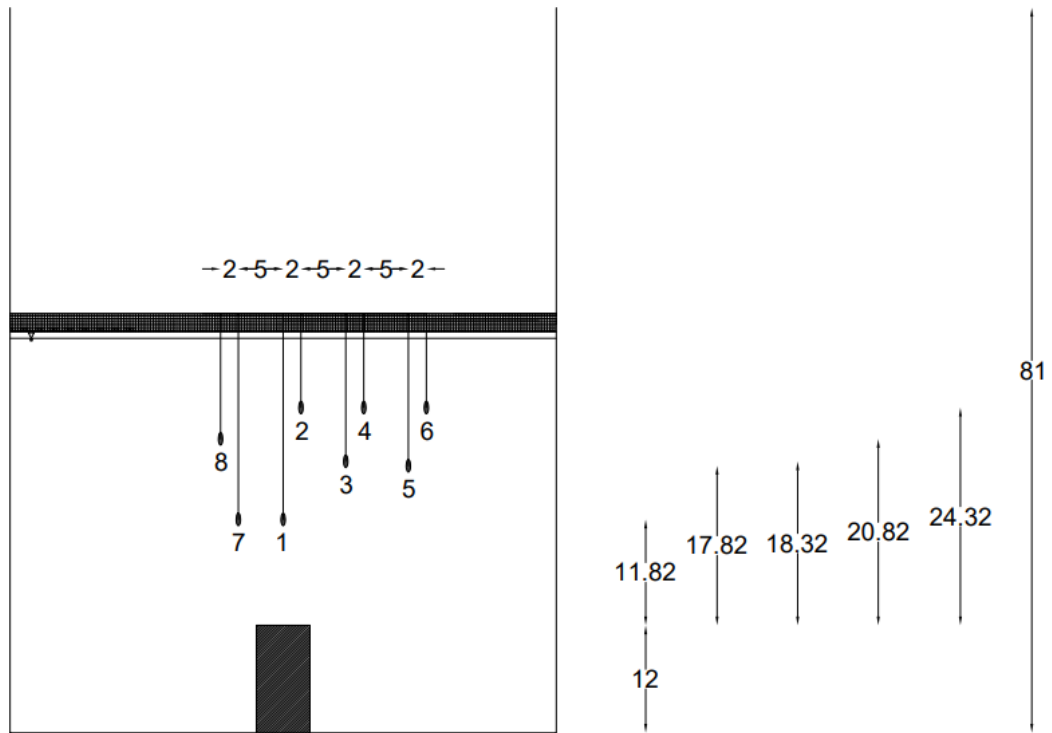


Figure 64- Lateral view, Orthogonal Projection, Big Bin, [cm]

6.3.3 Pipe experiments, setup

The last experiments carried out with this piece of technology, namely CCR second type, were realized in two different pipes full of water, with the same diameter, as well as thickness, but different lengths.

The purpose of this experience was to simulate, as much as possible, the borehole environment. Therefore, throughout the pipe confinement would have been useful to see the pressures detected from the sensors seen in Paragraph 6.3.2, second typology. The initiation system is always the same, it was used the same 11b booster of Pentolite (Table 4) as explosive, it was placed at the bottom of the pipe and then sealed through a plastic cup visible in Figure 67.

The pipes had a diameter of 100 mm, thickness of 7mm and lengths of 1.22 m and 1.69 m and in particular they were made of “coextruded ABS cellular core”. In the first experiment the sensors were placed starting from 5 cm far away to the top of the booster, instead for the longest pipe, the first sensor was placed 8 cm from the top of the explosive; further information about these experiments are attached in Table 7, 8.

Table 7- First Pipe Setup, Length: 122 cm

CHANNEL	DISTANCE [cm]
1	5
2	11
3	23
4	38
5	53
6	68
7	83
8	98

Table 8- Second Pipe Setup, Length: 169 cm

CHANNEL	DISTANCE [cm]
1	8
2	18
3	28
4	58
5	88
6	108
7	128
8	148

Unfortunately, those experiments were not successful since the shock waves, generated by the explosion, was not fast enough to reach the gauges and thus, to detect any significant pressure. This was due to the fact that the breakage at the base of the pipe happened before it could propagates.

Some pictures of the experiments are shown in Figure 65, 66, 67.



Figure 65- Pipe experiments, setup



Figure 66- Inside view's Pipe



Figure 67- NONEL Detonator Glued at the Bottom Plastic Cup

6.3.4 First Borehole tests, setup

Finally, after different attempts at a “small” scale, after seeing the behaviour respond of these sensors, that technology was ready to be applied inside a borehole. Obviously, that environment was completely different: first of all because of its heterogeneous composition, presence of cracks and so on; it was impossible to check the borehole wall accurately and thus, it was assumed that the rock was in good state except for the experiment on the parallel holes, as discussed later on. The borehole diameter was 10 cm and a length of about 700.

The experiment setup is shown in Figure 68. Starting from the left, the first element is the blasting machine, which always was inside the bunker; the red line represents the electric fireline, which ends with the electric detonator that in its turn, initiates the NONEL line, up to reaching the NONEL detonator placed inside the cartridge of emulsion explosive (50x400 mm) at the bottom; finally, the sensors, that have been placed at different distances from the top of the second cartridge, in this case without stemming. However, different experiments were carried out by using different mass of explosive, respectively: one, two and three cartridges, in Table 9 plus another experiment were carried out using the Pentolite 50/50 booster, which was used in the previous experiments. Besides, the sensors were sank in water, therefore the shock wave detonation travels through the water medium. There was no need to fill up the whole borehole with water since the measurement will be got from the sensors themselves, hence it will be necessary to sink the sensors into the water and make it sure that there was a consistent “gap” (franchise) of water between the last sensor and the water table.

Table 9- Amount of Explosive Material

Size [cm]	V [cm³]	ρ [g/cm³]	m [kg]
5x40	785	1.14	0.8949
5x80	1570	1.14	1.7898
5x120	2355	1.14	2.6847

If the franchise was not enough, the measurements would be affected by reflection waves, which would produce too much noise, in particular to the closest sensor to the water table. This phenomenon is noticeable in the pipe experiments, where the measurements were affected by reflected waves, which made the experiments sort of useless.

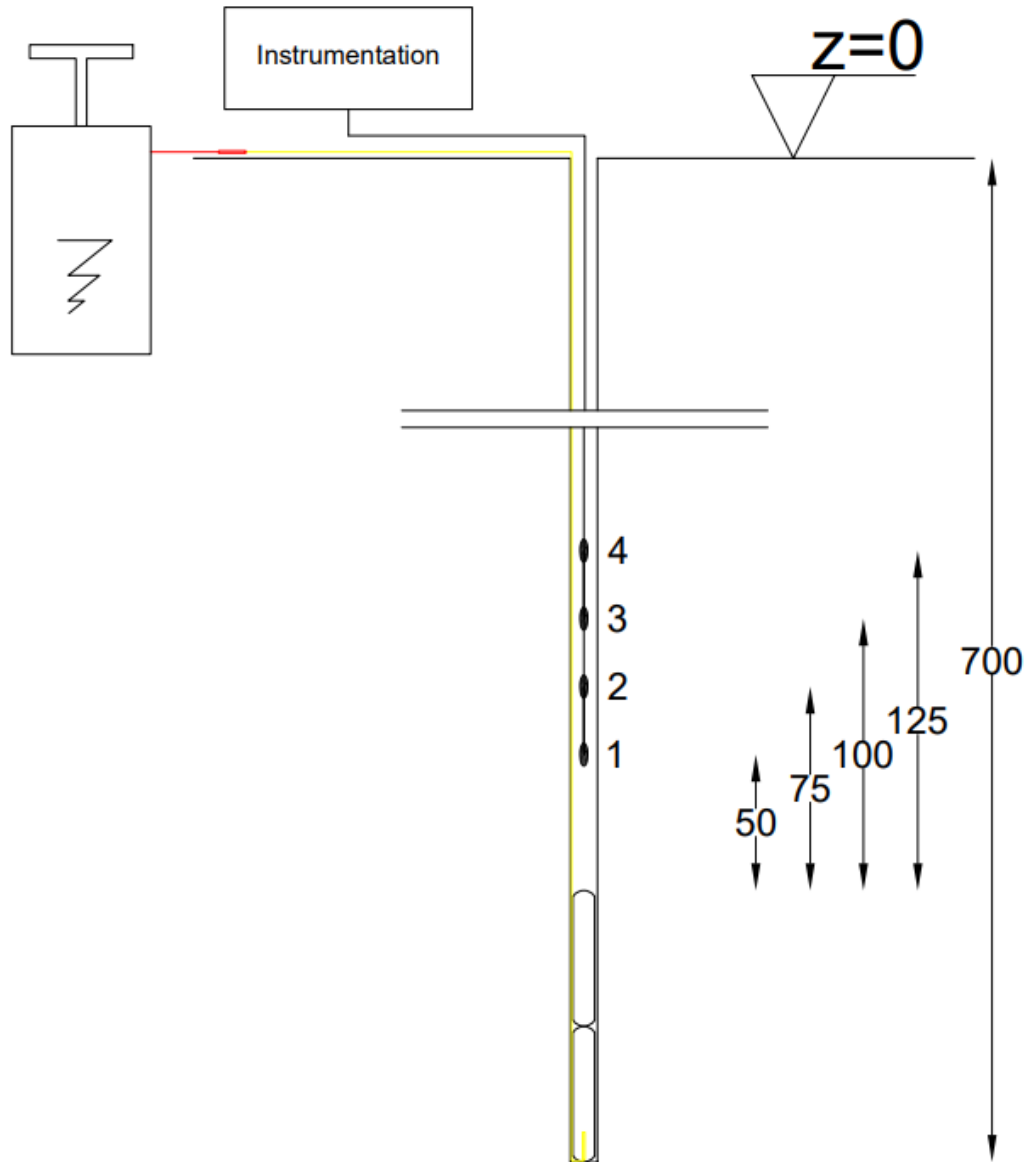


Figure 68-Sketch of the First Borehole Tests, [cm]

The explosive employed in these experiments was an emulsion with the composition and properties showed in Table 10 and Table 11 (for further information, see Appendix I).

As it can be seen in Figure 68, two cartridges of emulsion were placed; since this kind of emulsion is sensitized, it does not need a booster, and the NONEL detonator was placed at the bottom hole. However, in order to ensure the detonation continuity between the two charges, they were tied up together using a tape, as shown in Figure 69.

Table 10-Senatel Magnafrac, Emulsion by Orica

Mixture Name	Percentage %
Ammonium nitrate	70-80
Sodium nitrate	7-13
Water	7-13
Petroleum	3-7
Glass, Oxide, Chemicals	0.97-5
Polysobutylene	0.5-2
Sorbitan, (Z)-9-Octadecenoate (2:3)	0.5-2
Paraffin Waxes and Hydrocarbon waxes	0.5-2
Silica, Amorphous, Precipitated and gel	<0.15

Table 11-Emulsion, Magnafrac Technical Properties

Magnafrac		
Cartridge Density		1.14 g/cc
VOD		5000 m/s
Water resistance		Excellent
Relative Effective Energy	Relative Weight Strength	91
	Relative Bulk Strength	120



Figure 69- Connection of Two Cartridges of Emulsion.

6.3.5 Second Borehole tests, setup

The second tests were carried out using a constant amount of explosive (Magnafrac in Table 11), i.e. two cartridges, namely 1.7898 kg in each experiment. The procedure adopted was the same that has been examined in Paragraph 6.4.3, with the same initiation system; the only difference compared to the previous tests was the length of stemming inside the borehole, which was changed. Table 12 summarizes the main information about those tests.

Table 12- Second Borehole tests

TEST	STEMMING [cm]	EXP. MASS [kg]
1	45	1.7898
2	100	1.7898
3	122	1.7898

The AutoCAD sketch in Figure 70 is the example of the second experiment summarized in Table 12, which was realized using 1 m of stemming.

The stemming is basically made by crushed material, gravel, with a size of about 8-16 mm of diameter (unfortunately, the grain size distribution curve was not provided).

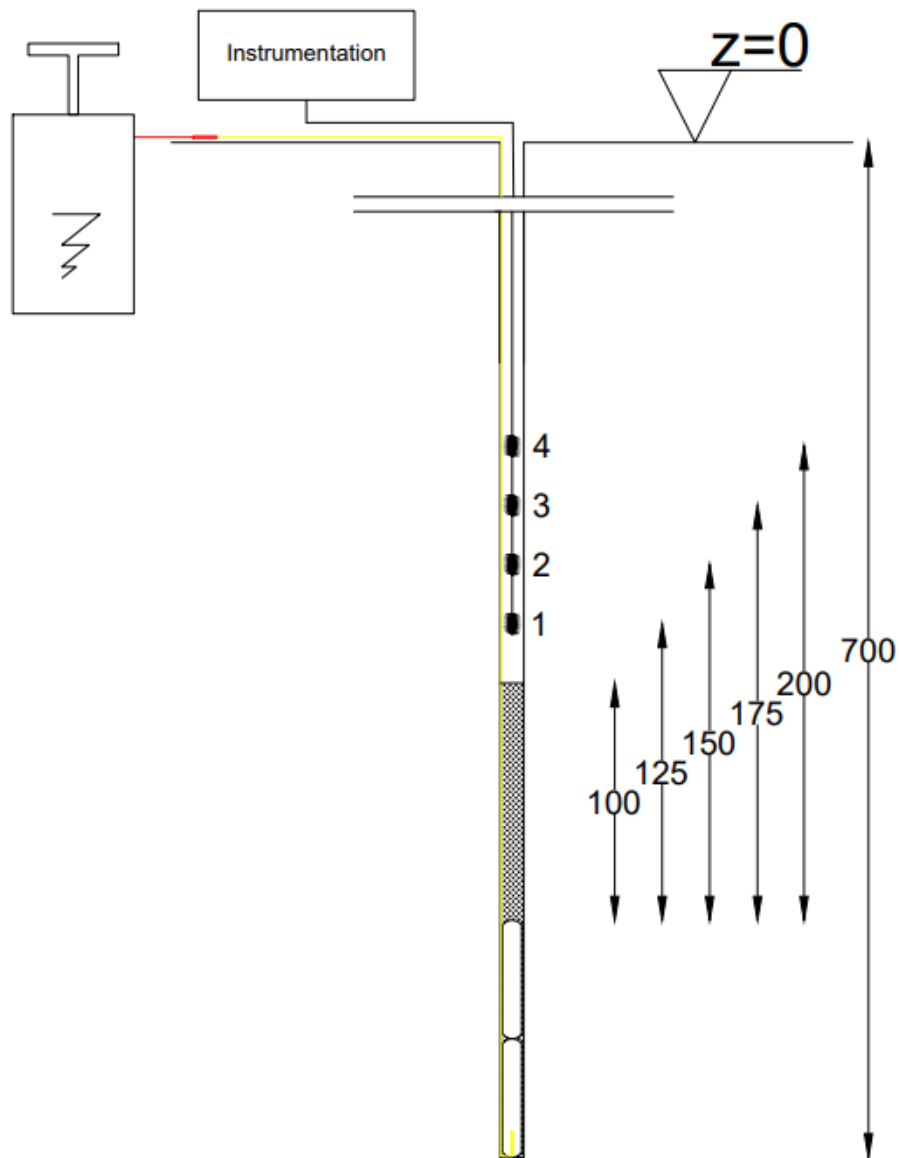


Figure 70- Sketch of Second Borehole Tests, [cm].

7 RESULTS

The tests described in Chapter 6 are in the following analysed, according to the different theories previously examined.

First of all, a comparison between the Autodyn simulation code and the measurements obtained through the pressure gauges is provided.

7.1 VERIFICATION OF THE PRESSURE SENSOR FUNCTIONALITY

The calibration and the functionality of these sensors were verified by running different simulations throughout the Autodyn Code. In particular, only two experiments were performed, since making simulations for all of them would have taken too much time. Furthermore, simulations were developed only for the experiment in homogeneous media, thereby water, and by means of the Pentolite booster, due to the difficulty of developing the theoretical Jones-Wilkins-Lee EOS for the emulsion in the boreholes; besides, the result in this situation might have been very far from what detected by the gauges, since the borehole wall's conditions were not checked (it is an impossible operation). It was chosen to take the experiment in the big garbage bin, discussed in Paragraph 6.4.2.2, Figure 63, plus the other experiment seen in Paragraph 6.4.2.1, Figures 60, 61, ran with the third typology of gauges. All the boundary conditions were fixed and the sensors were put in place according to the field experiments. Figure 71 shows the measurements and Autodyn simulation for the big garbage bin experiment.

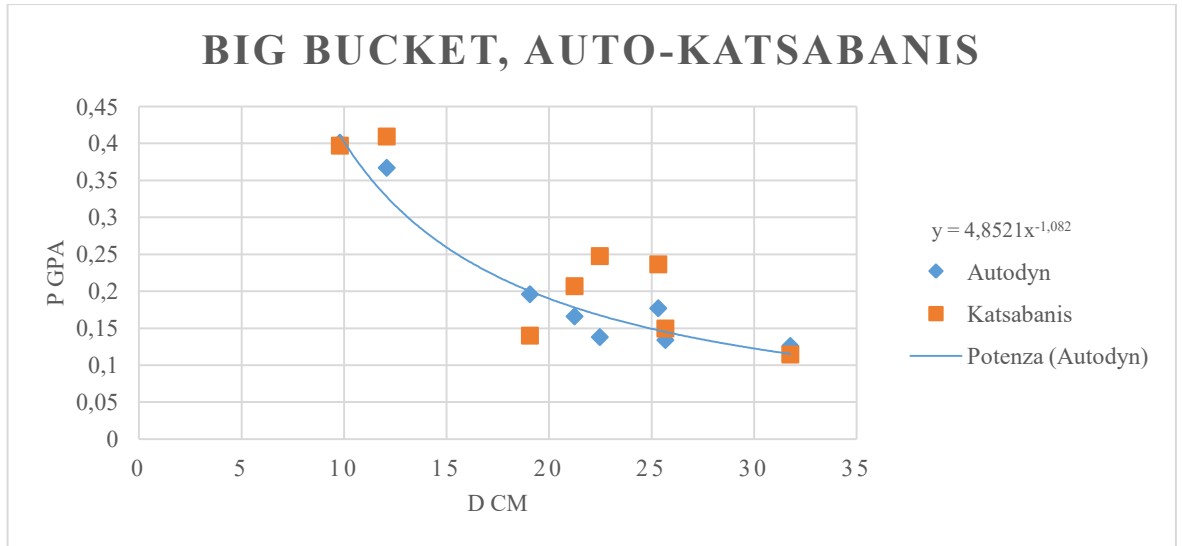


Figure 71-Comparison between Autodyn and Pressure Gauges, Big Garbage Bin

The attenuation equation of the Autodyn data is presented in the graph and has form: $P=K (x)^{-m}$. The distance, represented in the x-axis, is obtained as the root sum squared of the x-position (horizontal distance, on respect of the centre of the bucket) plus the y-position (distance from the top of the Pentolite booster). All the peak pressures and distances are shown in Table 13, 14.

Table 133- Garbage Bin Measurements

Big bucket	CH	P [GPa]	d [cm]
	1	0,39705	9,8
	2	0,2476	22,38951
	3	0,14	17,7395
	4	0,1496	24,04766
	5	0,2364	21,11019
	6	0,1144	27,44613
	7	0,4094	11,00182
	8	0,2069	20,06091

Table 14- Garbage Bin Autodyn Simulation

Big bucket	CH	P [GPa]	d [cm]
	1	0,401	9,8
	2	0,138	22,47866
	3	0,196	19,07066
	4	0,134	25,67664
	5	0,177	25,33061
	6	0,126	31,76932
	7	0,367	12,0847
	8	0,166	21,24712

As it can be seen, the measurements are pretty close to the simulation ran with Autodyn code. The little mismatch could be due to different problems, first of all to the fact that the water media inside the library of Autodyn had different values of bulk sound velocity, C_0 and s , regarding the Hugoniot planes, indeed it was modified according to real values. Furthermore, the explosive, (Pentolite) always inside the library, had different composition of PENT/TNT and, besides, the explosive volume had to be created since the booster geometry was not present in that library.

As previously said, another comparison was done: in this case, it was considered the experiment regarding the third typology of CCR inside a normal bucket. The comparison is shown in Figure 72; in this case though, the measurements and simulation are farer in comparison with Figure 71: this is due to the distance from the explosive, which is less in the experiment represented in Figure 71. As previously said, indeed, a huge change of pressure correspondes to a small change of resistance, Paragraph 5.2.2, Figure 38. Therefore, it can be noticed that after a certain distance, 8 cm, the measurements and the pressure simulations are very close each other.

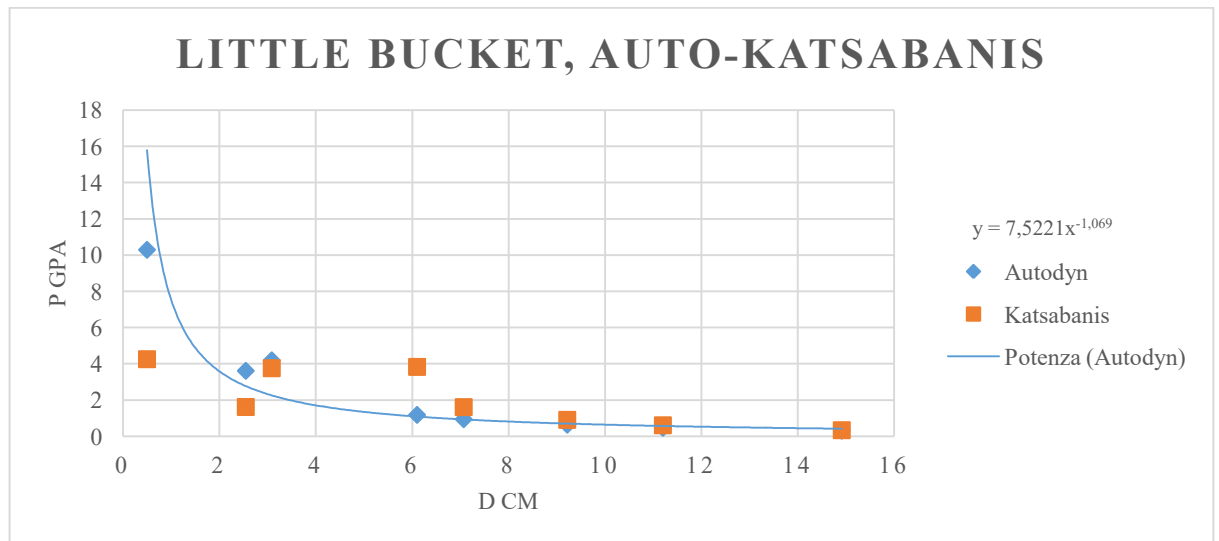


Figure 72-Comparison between Autodyn and Pressure Gauges, Bucket with Third Typology Gauges

In Table 15, 16 show the data obtained from the experiment and the Autodyn code respectively.

Table 15- Little bucket measurements

Little bucket		
CH	P [GPa]	d [cm]
1	4,2578	0,5
2	1,6219	2,54951
3	3,832	6,103278
4	0,910576	9,219544
5	3,7606	3,088689
6	1,6142	7,071068
7	0,6117	11,20446
8	0,34052	14,91643

Table 16- Little bucket Autodyn simulation

Little bucket		
CH	P	d
1	10,294	0,5
2	3,616	2,54951
3	1,184	6,103278
4	0,643	9,219544
5	4,198	3,088689
6	0,946	7,071068
7	0,472	11,20446
8	0,31	14,91643

It was useful to calculate and plot the absolute error (between the simulations and the measurements): in this way it is evident, as said before, that the higher the pressure detected, the higher the gap between the simulations. Figures 73 and 74 show the pressures versus the absolute errors. This behaviour is well visible in Figure 74, since the distances from the charge are way low compared to the big bucket experiment, and the pressures detected are higher.

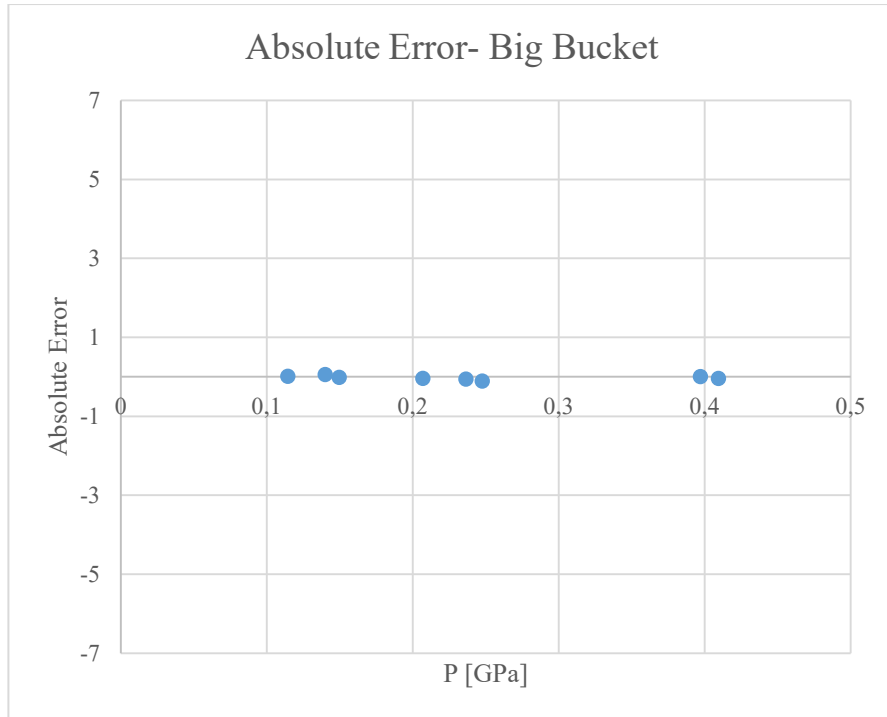


Figure 73- Absolute Error, Big Garbage Bin

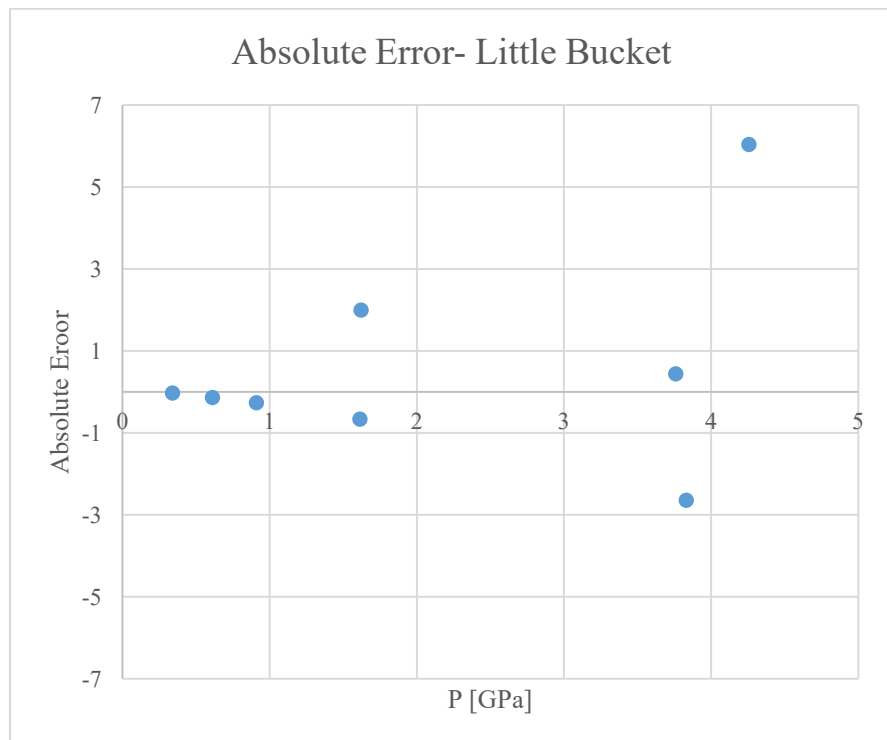


Figure 74- Absolute Error, Bucket with Third Typology CCR

7.2 COMPARISON BETWEEN EMULSION CHARGE AND PENTOLITE CHARGE

As anticipated in Paragraph 2.9, a comparison attempt employing Equation 23 was done (Cole’s law) in the following part. However, this analysis did not bring up to the attention any significant features. Figure 75 shows the graph containing part information about the experiments discussed in Paragraph 6.4.4. In fact, in Figure 75, two curves are drawn, the blue one representing some gauges in different experiments, namely using one, two, three cartridges of emulsion; on the other side, the orange curve represents the only experiment of Pentolite 50/50 into a borehole. These different experiences were compared according to the scaled distance law (x-axis) and the pressure detected by the gauges (y-axis).

Not all the values were taken into consideration, since, as said in Paragraph 2.9, the distance between “donor-acceptor”, in this case represented by “explosive charge-gauge”, had to be significant. Thereby for this purpose, the distances taken in consideration had to be greater than the ratio $D/D_{cg} > 2.5$, where D is the distance of the gauges from the top of the charge, and D_{cg} is position of the centre of gravity with respect to the whole column charge.

Regarding the calculations of the scaled distances, the relative weight strength was used. By knowing the energy available per weight of TNT, PENT and emulsion, the relative strength was calculated for both the explosives. Table 17 sums up the results.

Table 17- Relative Weight Strengths, PENT, Emulsion

WSPENT [kcal/kg]	WSTNT [kcal/kg]	WSem [kcal/kg]	RWS pent/TNT	RWS Em/TNT
1408	1210	801	1,081818182	0,661983471

In Tables 18-24, the red cells show the values taken for the comparison, which means the ones considered far enough from the explosive charge (Emulsion data). Instead, for the Pentolite booster, the data considered are in Table 24 and the curve in Figure 75 is represented by the orange curve.

Table 148- One Cartridge, First Experiment

CH	P [GPa]	Dc/W ^{1/3}
1	1,3922	0,357202
2	0,3219	0,833472
3	0,211	1,428809

Table 19- One Cartridge, Second Experiment

CH	P [GPa]	D/W1/3
1	0,195082	0,833472
2	0,114517	1,13114
3	0,00379	1,726477
4	0,005615	2,024145

Table 2015- Two Cartridge, First Experiment

CH	P [GPa]	D/W1/3
1	0,2212	0,850535
2	0,09643	1,086794
3	0,02686	1,559313
4	0,02588	1,795573

Table 2116- Two Cartridge, Second Experiment

CH	P [GPa]	D/W1/3
1	0,6286	0,614275
2	0,3516	0,850535
3	0,1735	1,559313
4	0,05845	2,268092

Table 22- Three Cartridge, First Experiment

CH	P [GPa]	D/W1/3
1	0,8575	0,701732
2	0,3831	0,908124
3	0,2256	1,733691
4	0,1777	2,146474

Table 23- Three Cartridge, Second Experiment

CH	P [GPa]	D/W1/3
1	0,27278	0,908124
2	0,143512	1,320907
3	0,127656	1,733691
4	0,06786	2,146474

Table 24- One Booster of Pentolite, First Experiment

CH	P [GPa]	D/W1/3
1	0,4357	1,660356
2	0,249	1,977218
3	0,1123	2,29408
4	0,1199	2,610942

Figure 75 shows the equation of the curves and their coefficients of correlation, which give an indication on how much the curves fit.

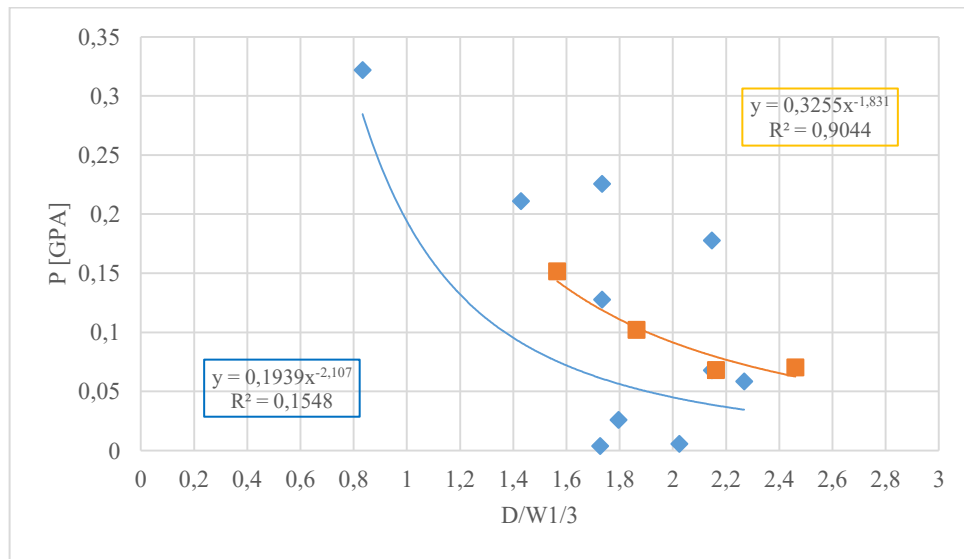


Figure 75- Blue: Column Charges Experiments, Orange: Pentolite Booster Experiment

It is evident that the Emulsion curve does not fit the points detected and, unfortunately, from these experiments it is impossible to obtain reasonable conclusion since the data collected were not enough. However, the points obtained through the Pentolite booster are perfectly fitting the curve, thus a comparison will be provided with these data.

According to Equation 23, the pressure values were obtained for the same scaled distances. Table 25 and Figure 76 show the results obtained.

Table 25- Gauge's Pressures, Cole's Pressures

CH	P _{gauge} [GPa]	D/W1/3	P _{Cooler} [GPa]
1	0,4357	1,66035614	0,02947305
2	0,249	1,977217999	0,024194177
3	0,1123	2,294079858	0,020453369
4	0,1199	2,610941717	0,01767143

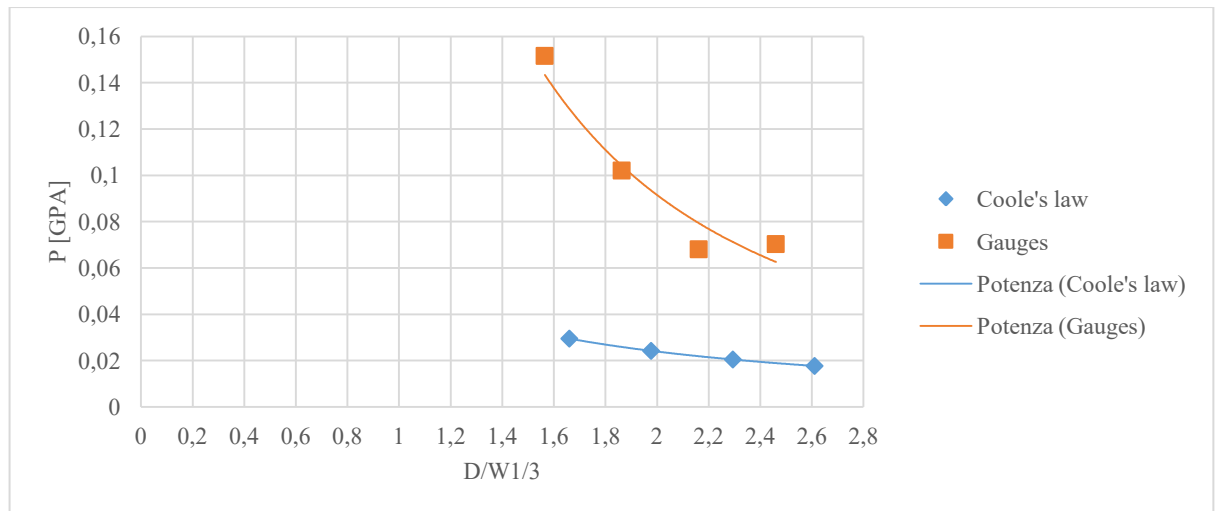


Figure 76- Pentolite 50/50 in Borehole, Pressure vs Scaled Distance

From Figure 76 it is evident that the magnitude of pressure detected by the gauges inside the borehole, is one order greater than the values calculated from the Cole's. This is mainly due to what is called “reverberation”, namely the persistence of shock waves in enclosed space as result of continued multiple reflections, with or without continued emission by source. The multiple reflection of the shock waves in this case is because of the constrain environment of the bore-walls. Furthermore, another effect has to be taken into consideration. Equation 23 was obtained by using spherical charge of TNT and the scaled distance considers a decay for this type of charge, besides the gauges were placed very far from the charge (several feet). Thus, first of all the charges used in the experiments in Paragraph 6.4.4 were not spherical at all moreover, the distances were not as relevant as the Cole's experience. By assuming the same environment of Coole (deep water) and considering a spherical charge, it can be claimed that the whole mass of the charge contributes to the explosion and thus, the pressure of a spherical charge is supposed to be greater than the column one, since the detonation reactions progress during time and, indeed, the total mass of the column charge cannot suddenly contribute to the explosion reactions. A different method for comparing cylindrical and spherical charges is described in the next Paragraph.

7.2.1 Holmberg-Persson adapted integration

Taking advantage from the similarity of the Holmberg and Persson's equation for particle velocity (1978) and the Coole's equation (Equation 23), a different approach for the above problem can be examined.

The Holmberg and Persson equation is shown in Equation 27:

$$PPV = K \frac{W^\alpha}{R^\beta} \quad (27)$$

where K , α and β are constants for the particular site, PPV is the peak particle velocity, W is the charge weight and R is the distance. Equation 27 structured in a similar way as Equation 23;

Thereby, the coefficients of Equation 23 can be converted into the coefficient in Equation 27 $\alpha=m/3$, $\beta=m$ and $K=K$.

Finally, the formula for the pressure transmitted from a cylindrical charge was obtained by Iverson et al. (2008) by integrating the incremental contribution of each length of explosive along the length of the explosive leading away from the point of observation.

$$P = K \left(q \int_{-x}^x \frac{dx}{(r^2 + x^2)^{\frac{\alpha}{2\beta}}} \right)^\alpha$$

The above formula will be referred to as Holmberg-Persson Adapted Integration equation (HPAI). However, the coefficients K , α and β were not developed since the number of experiments were too low and besides, the effect of reverberation was too high to obtain comparable pressures, thereby this approach was not further kept.

7.3 STEMMING ATTENUATIONS

An analysis regarding the experiments shown in Paragraph 6.4.5 was done. Therefore, the stemming experiments were used to build Figure 77, which contains different curves according to the length of stemming employed (gravel, crushed material present on site). The grain size distribution curve was not provided, though being roughly in the range 8-16 mm.

In all the experiments, the mass of explosive was constant, about 1.8 kg of emulsion, which means two cartridges in borehole. The lengths of stemming are summed up in Table 12.

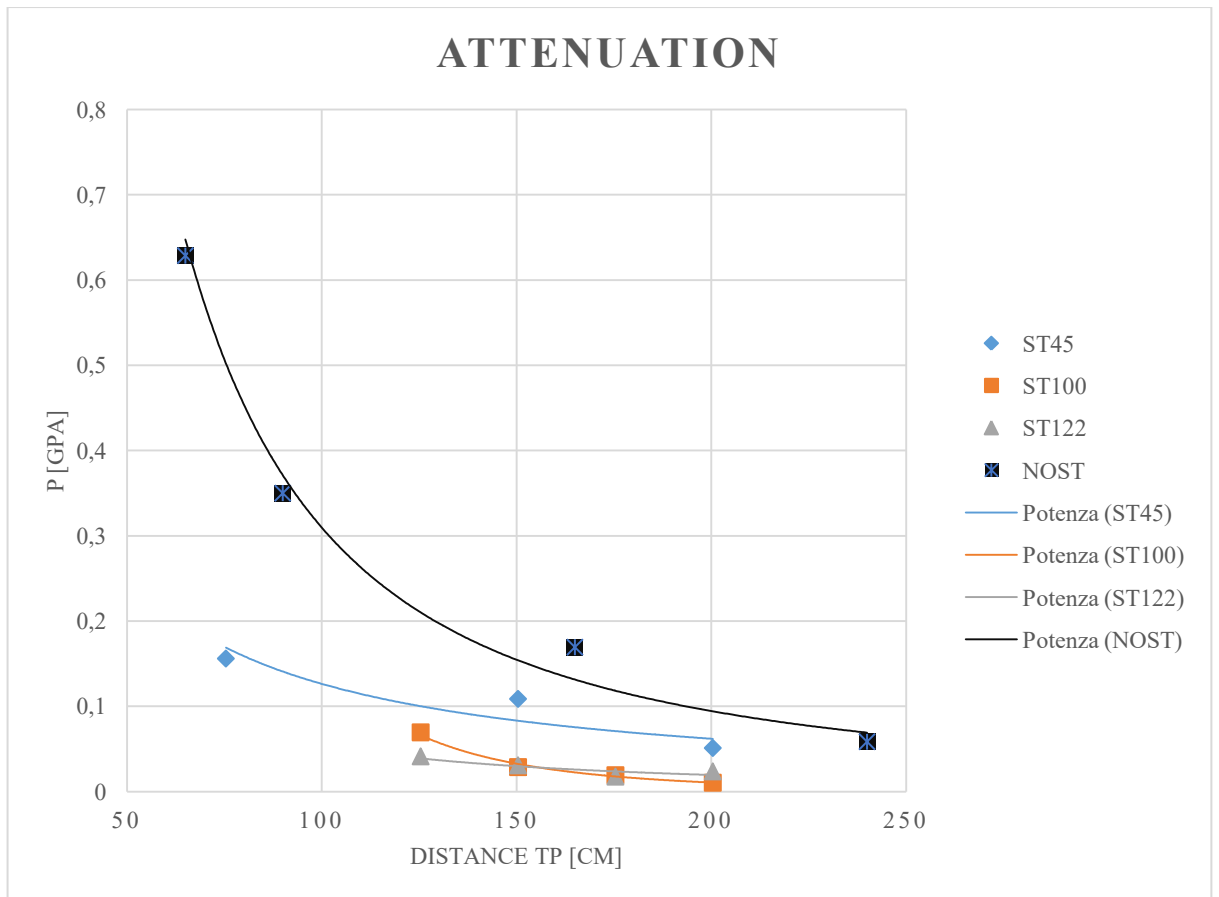


Figure 77- Attenuation Curves, ST45: 45cm of Stemming, ST100: 100cm of Stemming, ST122: 122cm of Stemming, NOST: No Stemming Used

All the curves showed in Figure 77 behave according to a power decay, as said in Paragraph 7.1, $P=K (x)^{-m}$. The curves below the black one, are those written in Table 12, namely, the experiments ran with different length of stemming; instead, the black curve represents the experiment showed in Paragraph 6.4.4, where the borehole was without stemming. Figure 77 also shows that the stemming strongly attenuates the pressure in function of the distance between the top of the cylindrical charge (two cartridges have 80 cm of length) and the gauges. This phenomenon is noticeable especially at a short distance from the charge (very high pressure indeed) since the rarefaction wave took over afterwards. For this reason, after about 150 cm from the top charge, the pressure assumes values very close to the borehole filled of stemming (same magnitude of pressure). This means that the attenuation effect due to stemming is very important at short distance from the charge and this is going to be very useful for further studies about decked technique, Figure 1, 23.

7.4 ATTENUATION IN PARALLEL HOLES

According to what said at Paragraph 3.9, it has been possible to replicate the experiment of Liu and Tidman (1995) regarding the pressure of an explosive charge detected in an adjacent borehole, as donor-acceptor in Figure 28 but in this case, the acceptor was made only by placing sensors in the parallel borehole without any extra “acceptor charge”. Only one experiment with four gauges was run, thus the measurements, as well as the graph in Figure 78, are not very reliable.

Therefore, throughout Eq. 22, 23, 24 (Liu and Katsabanis’s,1993), a comparison was performed.

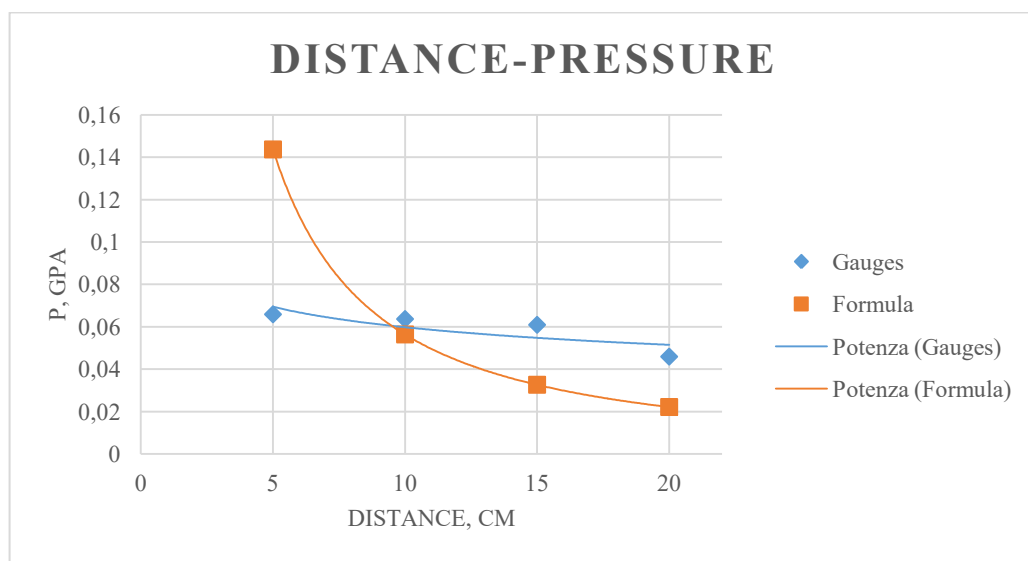


Figure 78- Parallel Holes Experiment, Blue: Pressures Detected, Orange: Pressures Calculated

Figure 78 shows the comparison between the gauges, which detected the pressure due to the explosion of two cartridges of emulsion (about 1.8 kg), and the pressures calculated through Equation 22. It is well visible that the pressures are so different each other. The reason why there is this huge mismatch in Figure 75 is that the pressure calculated through Equation 22 is the pressure in the rock and not the pressure in water of the adjacent borehole, (this phenomenon has been explained at the end of Paragraph 3.9). The two pressures might have been comparable if the borehole had a very little diameter and the sensors were straight in contact with the surrounding rock; in this case, probably, comparable pressures could have been obtained.

Furthermore, another difference of pressures was due to the conditions of the two boreholes, that were not checked, and thus likely, they presented different cracks in their own walls, therefore communication channels were present between them. Since technical rock parameters were not provided, the following parameters were attributed for calculating Equation 22, 23, 24; Table 26 summarizes the information:

Table 26- Rock-Explosive Parameters

C km/s	ρ_r g/cm ³	ρ_0 g/cm ³	D km/s
5	2,6	1,13	5

where C is the velocity of P-waves through a gneiss, ρ_r is the density of the rock, ρ_0 is density of the explosive and finally, D is the VOD of the explosive. Table 27 shows the results of the pressures with respect of the distance from the top of the column charge (80 cm from the bottom of the hole).

Table 27- Pressures detected in the parallel hole through third type CCR, Pressures Calculated by Eq.22

d [cm]	P_{gauges} [GPa]	$P_{\text{calculated}}$ [GPa]
5	0,065851	0,143680452
10	0,063631	0,056364699
15	0,060886	0,032604984
20	0,045883	0,022111423

8 CONCLUSIONS

After the experiments carried out and the analysis performed in this work, it can be said that:

- regarding the CCR gauges, it was found a new design, with lower construction time compared to the past gauges, and besides, that gives a clearer and better signal trend (CCR third typology, Paragraph 6.2.3).
- regarding the PVDF gauges, they have a faster response and the measurement is repetitive, which means that for the same stimulus the sensor produces the same voltage, besides, every time they behave in the same way.

Then, it can be claimed that the measurements through CCR gauges are very reliable and that, according to the calibration curve used, different ranges of pressure can be detected, even though it is known that there is a uncertainty in case of high pressure (i.e. Ginsberg et al. 1991).

Furthermore, in this work, the experiments presented were not sufficient for providing good answers to what explained at the Introduction Chapter, namely, the search for a pressure relief function through the media (stemming material, surrounding rock), with respect to the distance and time, for what regarding malfunctions, sympathetic detonation and desensitization.

From the results presented in Chapter 7, it can be seen that a lot of scatter is present in the analysis; however, if more tests were available, some important relationships could have been taken, for instance for what described in Paragraph 7.3.

Nowadays, the research should focus on the PVDF gauges; thus, new tests have to be performed, first of all by means of the Hopkinson Split Bar and then by going further on a test site, where the shock wave will be produced by detonating explosive. So, a calibration curve can be developed, and thus, the PVDFs might be used as pressure gauges, which will be more performing and cheaper compared to the CCR gauges.

REFERENCES

Allen-Bradley. *Hot-Molded Carbon Composition Fixed Resistors*. A-B Datasheet.

Ansys. (2011). *Ansys Autodyn - Explicit Dynamics*

Cole R. H.. (1948). *Underwater Explosions*. Princeton, New Jersey. Princeton University Press.

Cooper P. W.. (1997). *Explosives Engineering*. ISBN 0-471, Library of Congress Cataloging-in-Publication Data.

Forbes J. W.. (2012). *Shock Wave Compression of Condensed Matter*. Springer Heidelberg New York Dordrecht London.

Ghorbani A. (1997). *The study of Explosive Malfunction in Parallel Charges*. Kingston, ON: Queen's University Thesis.

Ginsberg M., Asay B.. (1991). *Commercial Carbon Composition Resistors as Dynamic Stress Gauges in Difficult Environments*. Rev. Sci. Instrumentation, Volume 62. No 9. September edition.

Guillermo S. . (2007). *Development, Characterization and Application of a Reactive Bulking Agent for Wall Control*. Kingston, ON: Queen's University Thesis.

Hoerth et a.. (2014). *In situ measurements of impact-induced pressure waves in sandstone targets*. Journal of Geophysical Research: Planets. AGU Publications.

Holmberg R., Persson P-A. (1978). *The Swedish approach to contour blasting*. Proceedings of the 4th Conference on Explosives and Blasting Technique, p.113-127.

Iverson S., Kerkerling C., Hustrulid W. . (2008). *Application of the NIOSH-modified Holmberg-Persson Approach to Perimeter Blast Design*. NIOSH/SRL.

Ledoux L. (2015). *The Role of Stress Waves and Gases in the Development of Fragmentation*. Kingston, ON: Queen's University Thesis.

Licht H. H.. (2000). *Performance and Sensitivity of Explosives*. Institut Franco Allemand de Recherches de Saint Louis, Deutsch-Französisches Forschungsinstitut Saint Louis, (ISL), Postfach 1260, D-79574 Weil am Rhein (Germany)

Katsabanis P. D., Yeung C., Fitz G., Heater R., (1994). *Explosives Malfunction From Sympathetic Detonation to Shock Desensitization*. Proc.. 10th Annual Symposium on Explosives and Blasting Research, ISEE, Austin. Texas.

Katsabanis P. D.. (2013). *Shock initiation and malfunction of commercial explosives and accessories: An approach using the critical energy fluence*. Rock Fragmentation by Blasting: Fragblast 10.

Katsabanis P. D., Omid O., Rielo O., Ross P.(2014). *A review of timing requirements for Optimization of Fragmentation*.

Katsabanis P. D.,. (1997). *Performance and Analysis of Aquarium Experiments to Provide Shock Wave Amplitudes for the Evaluation of Detonators under Shock Impact*. Final Report to The Ensign-Bickford Company.

Malfunction, Sympathetic Detonation and Desensitization of Explosives:
http://www.iring.ca/_Tutorials/

Mancini R., Cardu M.. (2001). *Scavi in Rocca, gli Esplosivi*. Hevelius Edizioni. Torino, Italy.

Mohanty B.. (2013). *Energetics and Performance of Modern Commercial Explosives*. Performance of Explosives and New Developments.

Person P.A., Holmberg R., Lee J. (1994). *Rock Blasting and Explosives Engineering*. CRC.

Dubos R. J. (1953). *The Art of Scientific Investigation*.

Rock Fragmentation by Blasting: Fragblast 9. (2009) Proceedings of the ninth international symposium on rock fragmentation by blasting. Fragblast 9, Granada.

TE Connectivity Technology. (2019). *FDM series' Datasheet*.

Watson W. R. (1967). *Gauge for Determining Shock Pressures*. Review of Scientific Instruments 38, 978.

Wieland M. (1987). *Cross Borehole Wave Measurements in Underground Coal*. 13th Conference of Explosives and Blasting Techniques (ISEE).

Wieland M. (1987). *The Desensitization and Malfunction of Coal-Mine Explosives*. Proc.. 13th Annual Conference on Explosives and Blasting Techniques. Cleveland, OH.

Yeung C. (1992). *The Study of Sympathetic Detonations in Boreholes*. MSc. Thesis. Department of Mining Engineering, Queen's University. Kingston.

Zhang Zong-Xian. (2015). *Rock fracture and Blasting. Theory and Applications*. Department of Arctic Technology, University Centre in Svalbard, Norway.

Zhou T. Qu, M. (2017). *Implosion of composite cylinders due to underwater impulsive loads in Dynamic Response and Failure of Composite Materials and Structures*.

Zou D. (2017). *Theory and Technology of Rock Excavation for Civil Engineering*. Springer, Metallurgical Industry Press. Hong Kong.

APPENDIX I

Additional Materials and Information

The following Appendix contains miscellaneous specifications, additional experimental data and any supplemental information not provided in the main body of the document.

SPECIFICATIONS						
Model	482C05	482C15	482C16	482C24	482C27	482C54 482C64
Performance						
Input Sensor Type	ICP*	ICP*, Voltage		ICP*, Voltage, Bridge/ Differential		ICP*, Charge, Voltage
Gain	—	x1, x10, x100 [1]	x0.1 to x200		x0.1 to x200 (ICP*, Volt) x0.1 to x2000 (Brdg/Diff)	x0.1 to x200
Charge Conversion (selectable)	—					0.1, 1, 10 mV/pC
Frequency Range (+/-5%) (gain <100)	0.1 Hz to 1000 kHz	0.05 Hz to 17 kHz	0.05 Hz to 100 kHz	0.05 Hz to 100 kHz [8]		0.05 Hz to 100 kHz [2]
Frequency Range (+/-5%) (gain ≥100)	—	0.05 Hz to 17 kHz	0.05 Hz to 50 kHz	0.05 Hz to 50 kHz [8]		0.05 Hz to 75 kHz [2]
Coupling (AC or DC)	AC			AC/DC		AC
Input Filter [3]	—	Optional		Optional Bridge & ICP* [9]		Optional
Output Filter [3]	—		Optional			10 kHz LPF (4th order)
TEDS Sensor Support	—		Yes			
Electrical						
AC Power (From power adapter) [4]	100 to 240 VAC					
AC Power (From power adapter) [4]	≤0.7 amps		≤1.6 amps			≤0.35 amps
Excitation Voltage (To Bridge/Diff. Sensors)	—				-12 V to +12 V [6][7]	—
Excitation Voltage (To ICP* Sensors)	+26 VDC		+24 VDC			
Constant Current Excitation (To ICP* Sensors) [5]	2 to 20 mA		0 to 20 mA			
DC Offset	≤20 mV		≤50 mV			
Broadband Electrical Noise (1 to 10000 Hz) (x1 gain)	3.5 μV rms	5.6 μV rms	50 μV rms			
Physical						
Front Panel Display/Keypad	—		Yes			
Digital Control Interface	—		RS-232	RS-232, Ethernet	RS-232	RS-232, Ethernet
Electrical Connector (Inputs)	BNC jack			BNC jack, 8-socket mini DIN		BNC jack
Electrical Connector (Outputs)	BNC jack					
Electrical Connector (DC Power Input)	5-socket DIN		6-socket mini DIN			
Size (Height x Width x Depth) (Nominal)	3.2 x 8.0 x 5.9 in 8.1 x 20 x 15 cm					
Weight	1.25 lb 567 gm	2.00 lb 907 gm		2.50 lb 1134 gm	2.40 lb 1089 gm	2.00 lb 1134 gm
Supplied Accessories						
Power Cord	017AXX					
Universal Power Adapter	488B04/NC		488B14/NC			
Communication Cable	—		100-7103-50			
MCSC Control Software	—		EE75			
Additional Versions						
Power Button Disabled; On Whenever Powered	482M167	—	482M166	—		
Notes						

Figure 79- Signal Conditioner's Datasheet by PCR

Senatel™ Magnafrac

USA, Canada & Mexico



Description

Senatel™ Magnafrac™ packaged emulsion explosive is a robust, detonator sensitive explosive. The explosive is orange in color with a firm putty-like consistency. This product is also available in High Wax (HW) formulations.

Application

Senatel™ Magnafrac™ is a water-resistant packaged explosive designed for priming applications, and as a medium density column explosive, in mining, quarry and construction, and general blasting work. The high detonation velocity and the robust nature of Senatel™ Magnafrac™ make it an ideal primer for the initiation of ANFO columns.

Senatel™ Magnafrac™ PMP film cartridges readily split during tamping to maximize coupling and bulk strength within a blasthole.

Key Benefits

- Senatel™ Magnafrac™ is a cost-effective emulsion formulation suitable for a range of blasting applications.
- Senatel™ Magnafrac™ reduces post-blast fumes and improves turnaround time.
- Senatel™ Magnafrac™ can be loaded into 115 mm (4½ in.) diameter upholes when used with cartridge loading equipment.
- The tight diameter control specifications and wax formulation of Senatel™ Magnafrac™ maximizes cartridge loader performance.
- Senatel™ Magnafrac™ is highly water resistant that minimizes leaching and reduces environmental impact.
- OH&S issues around the handling and storage of nitroglycerine are eliminated.
- Provides excellent fragmentation with minimum throw.

Technical Properties

Senatel™ Magnafrac™ 32 x 400 mm (1.14 x 16 in.)		
Cartridge Density		1.14 g/cc
Velocity of Detonation ¹		5,000 m/s 16,400 ft/s
Water Resistance		Excellent
Fume Class		1
Relative Effective Energy (REE) ²	Relative Weight Strength (RWS)	91
	Relative Bulk Strength (RBS)	120

- Packaged in PMP, easy to tamp plastic film or high strength, tear resistant Valeron film cartridges ideal for ragged, medium size boreholes.
- The packaging and emulsion color of Senatel™ Magnafrac™ provides high visibility in a range of environments.

Recommendations for Use

Blasthole Depth

Senatel™ Magnafrac™ is suitable for use in holes of any practical depth providing contained water does not exceed 20 m (65.6 ft.) depth.

Priming and Initiation

An Orica high strength electric, electronic, or non-electronic detonator can reliably initiate Senatel™ Magnafrac™ at temperatures higher than -15°C (5°F). At temperatures below -15°C (5°F), an appropriately sized Pentax™ Booster is recommended. Use of detonating cord with Senatel™ Magnafrac™ is not recommended. Detonating cord may adversely affect the performance of Senatel™ Magnafrac™.



V9 12/28/16

1 of 3



Figure 80-Emulsion Technical Datasheet, By Orica.

TECHNICAL DATA SHEET

Pentex™ AP Cast Boosters

USA & Canada



Description

Pentex™ AP Cast Boosters provide high energy initiating power for a wide range of explosive applications. The recessed groove in the base of Pentex™ AP Cast Boosters ensures reliable initiation with all types of detonator assemblies. They can be used to provide safe and reliable priming of booster sensitive explosives on most surface and underground blasting operations.

Pentex™ AP Cast Boosters are ideal for use in blasting applications which require multiple decking and multiple boosters down the hole.

Key Benefits

- High velocity
- High density
- High detonation pressure
- Long shelf life
- Excellent water resistance
- High safety and reliability
- Concentrated detonation energy

Technical Properties

Pentex™ AP "All Purpose" Booster			
Nominal Weight	340 g (12 oz)	454 g (16 oz)	908 g (32 oz)
Nominal Diameter	51 mm (2.01 in)	58 mm (2.28 in)	80 mm (3.15 in)
Nominal Length	126 mm (4.97 in)	126 mm (4.97 in)	126 mm (4.97 in)
Shell Material	Open top cardboard canister		
Shell Color	Fluorescent Orange		
Nominal Density	1.60 g/cc		
VOD	7,600 m/s (24,934 ft/s)		
Detonation Pressure	250 kb		
Water Resistance	Excellent		
Tunnel Arrangement	One blind detonator well & two through tunnels.		

Recommendations for Use

Priming and Initiation

Pentex™ AP Cast Boosters can be initiated by standard high strength electric, electronic and non-electric detonators or by 3.6 gram/m (18 grain/ft) detonating cord threaded into the center through tunnel.

When used with booster-sensitive explosives, ensure that the primer is in intimate contact with, and surrounded by, the explosive.

Figure 81- Pentolite 50/50 Booster, Technical Datasheet, by Orica.